The Microbial and Geochemical Architecture of Scotian Slope Cold Seep Site 2A-1, Scotian Slope, Canada

By
Elish Redshaw

A Thesis Submitted to
Saint Mary's University, Halifax, Nova Scotia,
in Partial Fulfillment of the Requirements for
the Degree of Master of Applied Science.

December 2024, Halifax, Nova Scotia

Copyright: Elish Redshaw, 2024

Approved: Dr. Todd Ventura
Supervisor

Approved: Dr. Erin Adlakha
Internal Committee Member

Approved: Dr. Christa Brosseau
Internal Committee Member

Approved: Dr. Greg Slater
Internal Committee Member

Approved: Dr. Christopher Algar
External Examiner

Date: Dec. 16th, 2024

List of Abbreviations

1G	Monoglycosidic headgroup
2G	Diglycosidic head group
ANME	Anaerobic methane oxidizing archaea
AOM	Anaerobic oxidation of methane
AR	Archaeol
Bpdiol	Biphytanediol
brGDGT	Branched glycerol dialkyl glycerol tetraether
brSRI	Branched Sulfate Reduction Index
BSR	bacterial sulfate reducers
Ca^{2+}	Calcium
CH_4	Methane
Chl *a*	Chlorophyll a
CL	Core lipids
Cl^-	Chloride
CL-DP	Core lipid decay products
cmbsf	Centimeters below sea floor
CO_2	Carbon dioxide
CO_3^{2-}	Carbonate
DCM	Dichloromethane
DIC	Dissolved inorganic carbon
DRNA	Dissimilatory nitration to ammonium
EA	Elemental analyser
ESI	Electrospray Ionization
F^-	Fluoride
FA	Formic acid
Fe^{2+}	Iron
GDD	Glycerol dibiphytanol diether
GDGT	Glycerol dialkyl glycerol tetraether
H_2S	Hydrogen sulfide
HCl	Hydrochloric acid
HCO_3^-	Bicarbonate
HPLC	High performance liquid chromatography
HS^-	Bisulfide
IC	Ion chromatogram
IPA	Isopropanol
IPL	Intact polar lipids
KMO	Kaiser-Meyeer-Olkin
M	Molecular ion
m/z	Mass to charge ratio
MBD	Modified Bligh and Dyer
MeOH	Methanol
Mg^{2+}	Magnesium

MI	Methane Index
Mn^{2+}	Manganese
MSR	Microbial sulfate reduction
N_2	Fixed nitrogen
Na^{2+}	Sodium
NaOH	Sodium hydroxide
NH_4^+	Ammonium
NH_4OH	Ammonium hydroxide
NO_2^-	Nitrite
NO_3^-	Nitrate
O_2	Oxygen
P	Photometer
PA	Phosphatidic acid head group
PAF	1-alkyl-2-acetoyl-sn-glycero-3-phosphocholine
PCA	Principal component analysis
PG	Phosphatidylglycerol head group
Phy *a*	Pheophytin a
PIC	Particulate inorganic carbon
PO_4^{3-}	Phosphate
PS	phosphatidylserine head group
qToF-MS	Quadrupole Time of Flight Mass Spectrometry
ROV	Remote operated vehicle
RP	Reverse phase
SMTZ	Sulfate-methane transition zone
SO_4^{2-}	Sulfate
TLE	Total lipid extracts
TOC	Total organic carbon
TPH	Total petroleum hydrocarbons

The Microbial and Geochemical Architecture of Scotian Slope Cold Seep Site 2A-1, Scotian Slope, Canada

By Elish Redshaw

December 16th, 2024

Abstract

Cold seeps occur globally along the seabed of continental margins, expelling reduced fluids, which help to form oasis-like ecosystems in highly redox stratified sediments. In this study, a 600 m long, six push core, transect was collected from cold seep site 2A-1, located on the Scotian Slope of Eastern Canada. Downcore porewater ions and lipidomic profiles were generated. These data were compiled as spatially resolved, two-dimensional heatmaps to examine both vertical and lateral changes in the subsurface geochemical and microbiological architecture. Twenty-three lipid classes, predominantly of archaeal origin, were tentatively identified and quantified. Microbially mediated metabolic zones of targeted processes, were mapped based on ion porewater concentrations, diffusion fluxes, carbon isotope values, lipidomic diversity patters, and biomarker proxy data. The resolved lipidome indicates a zoned archaeal community with diversity increasing as a function of seepage rate that provides insights into the seep's formation and microbial dynamics.

Acknowledgments

I would like to thank all members of my committee, especially my supervisor, Dr. Todd Ventura. The feedback and support from Dr. Erin Adlakha, Dr. Christa Brosseau, and Dr. Greg Slater, has been invaluable for the completion of this project. Dr. Ventura has taught me to stand up for my theories and have conviction in my results. I'll look back fondly on our spirted debates. Try not to miss me in the lab too much.

I would also like to extend my gratitude to Natasha McAdam and Adam MacDonald at the Nova Scotia Department of Natural Resources and Renewables. A special thank you for Natasha for creating the bathymetric and seismic images used throughout this thesis, and for always being free for a chat at the gym. A warm thank you to all members of the OGL for their guidance, especially to former lab manager Jeremy Bently, for his training on the MBD extraction technique and Nikita for her contributions of porewater anion data.

This thesis would not be complete without the unyielding support from my family, partner, and friends. Cameron has been my rock (pun intended) throughout this entire journey. He was always a shoulder to cry on and an (un)willing participant in my one-way ramblings. I like to especially thank my parents for teaching me resilience and perseverance. Their love and support have carried me through every challenge I have faced thus far.

Finally, I'd like to acknowledge myself – cheers. I've earned it.

"The harder I work, the luckier I get." – *Samuel Goldwyn*

Table of Contents

Table of Figures

Table of Tables

Chapter 1: Introduction and Background Information

1.1 Preamble

Cold seeps on the ocean floor expel low temperature fluids often rich in reduced carbon (including gas to liquid range hydrocarbons) and sulfur gases. Fluids are expelled at ambient seafloor temperatures, which is where they derive their name. Globally, these features release an estimated 600,000 metric tons of oil and 20–50 Tg of methane gas per year into the marine environment, making them the single most important source of oil and gas to the oceans (Hovland et al., 1993; Kvenvolden & Cooper, 2003; Kvenvolden & Rogers, 2005). Fluid migration is driven by a variety of geophysical processes including (i) plate tectonism that leads to the formation of fractures, faults, and folds in the basin bedrock (Barnes et al., 2010; Cartwright, 2011), (ii) sediment overburden and compression (Suess, 2020), and (iii) salt tectonism (Talukder, 2012; Suess, 2020). Cold seeps are found along both passive and active continental margins. Primarily identified by active gas seepage, other direct geological features associated with cold seeps include pockmarks (King & MacLean, 1970; Hovland et al., 2002), microbial mats and bioherms (Hovland et al., 2002; Vanreusel et al., 2009), authigenic carbonates (Kulm et al., 1986; Ritger et al., 1987), and gas hydrates (MacDonald et al., 1994). In seismic surveys, indirect seepage indicators include amplitude bright spots, gas washouts, and other acoustic turbidity anomalies (Wei et al., 2020) that commonly co-occur with faults (Cartwright, 2011). Satellite slick surveys provide further indirect seepage indicators (Ziervogel et al., 2014). As cold seeps are frequently associated with sub-surface petroleum reservoirs, their detection is of interest for oil and gas exploration for determining the locations and untapped reservoir potential of hydrocarbon prospects in the marine environment.

1.1.1 Biogeochemical cycling

Microbes extract metabolic energy by the oxidation of carbon bound to sedimentary organic matter (OM) mediated by a series of terminal electron acceptors that create distinct biogeochemical zones within sediments (Fig. 1.1). The upward migration of methane (CH_4) from deeper within the cold seep sediments changes the depth over which the biogeochemical zones form (Borowski et al., 1996; Jørgensen & Kasten, 2006). Each reaction can be viewed as a specific metabolism from different microbial communities. These reactions facilitate the cycling of key elements in ocean biogeochemical cycles. These cycles are interconnected through reactants, intermediates, and products. The focus of this study is primarily on reactions connecting the carbon, sulfur, and nitrogen cycles.

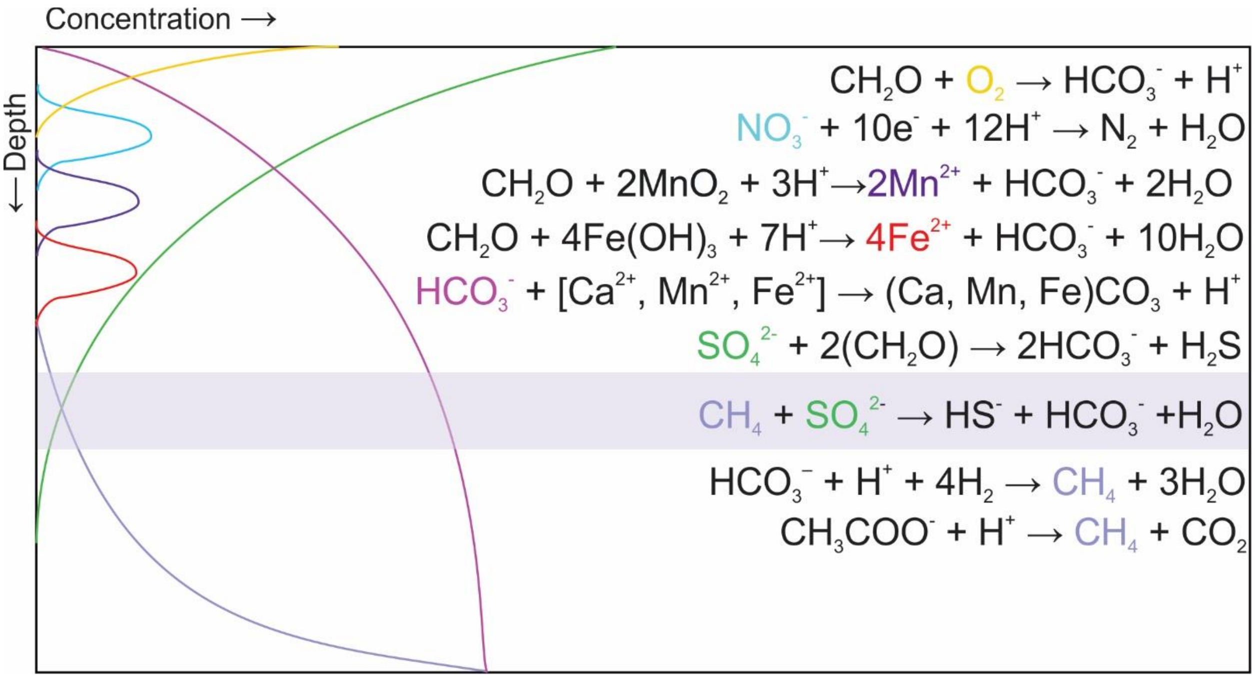

Figure 1.1: Idealized porewater redox tower. Ions have been coloured to match their corresponding reaction. Carbonate production, coloured pink, is not itself a microbial metabolism, but occurs are a result of biological activity in the sediment. The highlighted zone indicates the sulfate-methane transition zone, the focus point of anaerobic methane oxidation (modified from Jørgensen & Kasten, 2006 and Regnier et al., 2011).

Nitrogen is the limiting reactant in the marine environment, exerting a large influence on other biogeochemical cycles due to its role in primary productivity. This cycle is primarily driven by nitrification and denitrification reactions, as well as nitrogen fixation, which transforms unusable N_2 into fixed, useable nitrogen (organic N, NO_2^-, NO_3^-) and back to N_2 via microbial pathways (Gruber, 2008; Canfield et al., 2010). Nitrogen availability influences both the rate of organic matter degradation and the activity of microbial sulfate reducers within microbial mats (Canfield et al., 2010). The anaerobic oxidation of ammonia, referred to as anammox, is a secondary nitrogen sink occurring in low-oxygen sediments (Engström et al., 2005).

Oceans represent one of the largest pools of sulfur on Earth (Vairavamurthy et al., 1995). The marine sulfur cycle is driven by microbial sulfate reduction (MSR), where sulfate reducing bacteria (SRB) reduce sulfate (SO_4^{2-}) to hydrogen sulfide (H_2S) to fuel the heterotrophic consumption of sedimentary organic matter. In doing so, expelled reduced sulfur species can bind to available cations, such as metals or organic matter forming metal sulfides and organo-sulfur compounds. The resulting authigenic pyrite locks sulfur in a stable mineral form, preserving it in the geological record. The isotopic compositions of sulfur within pyrite and other sulfur compounds are therefore used to reconstruct paleoclimate and ocean salinity changes over Earth's long history (Vairavamurthy et al., 1995; Jørgensen et al., 2019). The sulfurization of organic matter marks an independent pathway for kerogen formation. These processes collectively mark relatively non-reactive sulfur sinks.

The carbon cycle is vital to life on Earth, but despite being studied extensively, significant gaps remain in understanding geological contributions. Judd et al., (2002) recognised that most published drawings of the global carbon cycle largely overlook geological sources of carbon outside of carbon dioxide (CO_2) emissions from volcanoes or fossil fuels. A 2022 review of the ocean carbon cycle from DeVries (2022) noted that CH_4 emissions from gas hydrates fell outside the scope of the review and neglected to mention cold seeps and hydrothermal vents. Biological processes within sediments have also been biased to downward reductive processes, ignoring the microbial oxidative attenuation of upward migrating reduced carbon pools from deeper within sedimentary basins.

The rate of methanogenesis is an estimated 85–300 Tg $CH_4 \cdot \text{year}^{-1}$ (Reeburgh, 2007), yet the natural contribution of the oceans to the global atmospheric methane budget is only 2-4% of total emissions (Judd et al., 2002). Much of this methane is lost by the microbial process through the anaerobic oxidation of methane (AOM; Eq. 1), which produces the largest energy yield along the redox tower by consuming > 90% of the methane within the shallow sulfate-containing sediments (Reeburgh, 2007; Knittel & Boetius, 2009).

$$CH_4 + SO_4{}^{2-} \rightarrow \; HCO_3{}^{-} + HS^{-} + H_2O \tag{1}$$

The AOM activity is concentrated in the sulfate-methane transition zone (SMTZ), where non-zero sulfate and methane concentrations overlap (R. Barnes & Goldberg, 1976). The anaerobic oxidation of methane is also a key process operating at cold seeps to regulate the flux of CH_4 to the atmosphere. Additionally, gas hydrates act as large reservoirs of methane, locking the gas in a cage-like framework of hydrogen bonded water molecules. Climate change, causing increased ocean bottom temperatures and pressures, poses an increased risk to the stability of these reservoirs, which can release the gas back into the oceans, further increasing methane fluxes to the atmosphere (Dickens, 2003). In situ micro-profiling of targeted porewater ions can reveal geochemical signatures of AOM and the SMTZ.

1.1.2 Microbial mediators of AOM

Microbial activity in shallow marine sediments has long been identified as a leading mechanism for the diagenetic alteration of organic matter and a fundamental driver of Earth's carbon cycle. Following the original works of Hinrichs et al. (1999) and Boetius et al. (2000) with the identification of AOM, recent studies have aimed to further refine the location and extent to which this process impacts carbon cycling and to resolve the unique microbiome that make enables its function. The anaerobic oxidation of methane is mediated by a syntrophic consortium of anaerobic methane oxidizing archaea (ANME) and SRB (Boetius et al., 2000; Hinrichs et al., 2000). Three ANME groups are involved in AOM special clades of methanogenic *Euryarchaeota*. These groups appear to gain energy exclusively from AOM (Knittel & Boetius, 2009). Anaerobic methane oxidizing archaea clades 1 and 2 occur in consortia with SRB from the *Desulfosarcina*/*Desulfococcus* group (Boetius et al., 2000; Orphan et al., 2001a) and ANME-3 occurs with SRB related to *Desulfobulbus* spp. (Niemann et al., 2006). Distinct lipid biomarker signatures can be assigned to each of these communities based on various lipid ratios and stable carbon isotope ratios (Blumenberg et al., 2004; Niemann & Elvert, 2008; Rossel et al., 2008).

The distribution of ANME and SRB in cold seeps have been studied worldwide (Orphan et al., 2001a; Teske et al., 2002; Knittel et al., 2005; Orcutt et al., 2010; Kleindienst et al., 2012; Niu et al., 2017). A pitfall in this research is that these studies have focused on the vertical distribution of the AOM consortia, ignoring potential horizontal spatial influences on the range and rates of activity. Most studies utilize a control, or ambient sample to highlight the unique ecosystem present within a seep, but neglect to relate these sites. This "point-sampling" approach has led to a large gap in the literature in understanding how the community dynamic changes from within the centre of the seep out to ambient sea floor conditions. Cao et al., (2015) acknowledged the lack of research in understanding microbial changes along an environmental gradient examining the changes in ammonia oxidizing archaea along a transect of the Thuwal Seep in the Red Sea. A 2020 study from Zhang et al. (2020) collected sub-samples along the transect of an East China Sea cold seep carbonate pipe for lipid analysis. Other studies have looked at fauna distribution along cold seep transects (Vanreusel et al., 2009; Sen et al., 2018). Microbial transect surveys are much more common for hydrothermal vent complexes (Sievert et al., 1999; Giovannelli et al., 2013; Rubelmann et al., 2017; Bentley et al., 2022). Expanding transect surveying to the cold seep environment will provide crucial insights into the complexity of these dynamic ecosystems.

1.2 Lipidomics

Lipidomics is the whole-scale study of lipids within a defined system. Lipids are major sources of metabolic energy and essential materials for the formation of tissues and cellular membranes. This encompasses many compound classes from simple hydrocarbons to sterols, fatty acids, waxes, phospholipids, and oils (Bergé & Barnathan, 2005; Summons et al., 2022). As the structural components of cellular membranes, lipids contribute a significant portion of preservable organic matter to Earth’s soils and sediments (ie., Langworthy et al., 1983; Kohl & Rice, 1999; Killops & Killops, 2004). Their abundance in the natural environment, coupled with their ability to persist over geological time, lends to their usage as biomarkers in the marine environment.

Membrane lipids from all three domains of life (Archaea, Bacteria, and Eukaryotes) have been identified in marine sediments. Lipp et al., (2008) suggest that Archaea contribute significantly to marine sedimentary biomass (87%). Archaea typically possess monolayer lipid membranes, whereas bacterial and eukaryotic lipids form bilayer membranes. Intact polar lipids (IPLs) of

Archaea are lipids found in their biological form with a polar headgroup, usually phosphate and/or a glycosidic base, attached to the glycerol of an ether-bound isoprenoidal core lipid (CL) (Fig. 1.2). Bacteria and Eukaryotes attach their headgroups to the glycerol of a fatty acid through ester bond linkages. The structural differences of archaeal lipids increase their stability, which allows them to persist not only deeper in marine sediments, but also in more extreme conditions than bacterial and eukaryotic lipids (Koga & Morii, 2005; Valentine, 2007).

Intact polar lipids are treated as the product of living cells, where upon senescence, the polar headgroups rapidly hydrolyze to more stable CLs (White et al., 1979; Harvey et al., 1986; Sturt et al., 2004). The quantitative detection of IPLs can be used to reconstruct the microbial population (Schippers & Neretin, 2006; Lipp et al., 2008; Lipp & Hinrichs, 2009), community dynamics (Cao et al., 2015; Lv et al., 2022), and metabolite availability and preference (Kellermann et al., 2012; Wegener et al., 2016). Compound specific isotope analysis of lipid biomarkers can be used to trace carbon cycling throughout the marine environment (Hinrichs et al., 2000; Orphan et al., 2001b; Thiel et al., 2001; Peckmann & Thiel, 2004). Intact polar lipids, and to a lesser degree CLs, are chemotaxonomically unique and are specific to their environment, which lends to their use as biomarkers to study material cycling in the marine environment (Rossel et al., 2008; Schubotz et al., 2009; Elling et al., 2017). This study aims to resolve the lipidome of a deep marine cold seep on the Scotian Slope and evaluate changes in diversity between the modern and paleoseep environment.

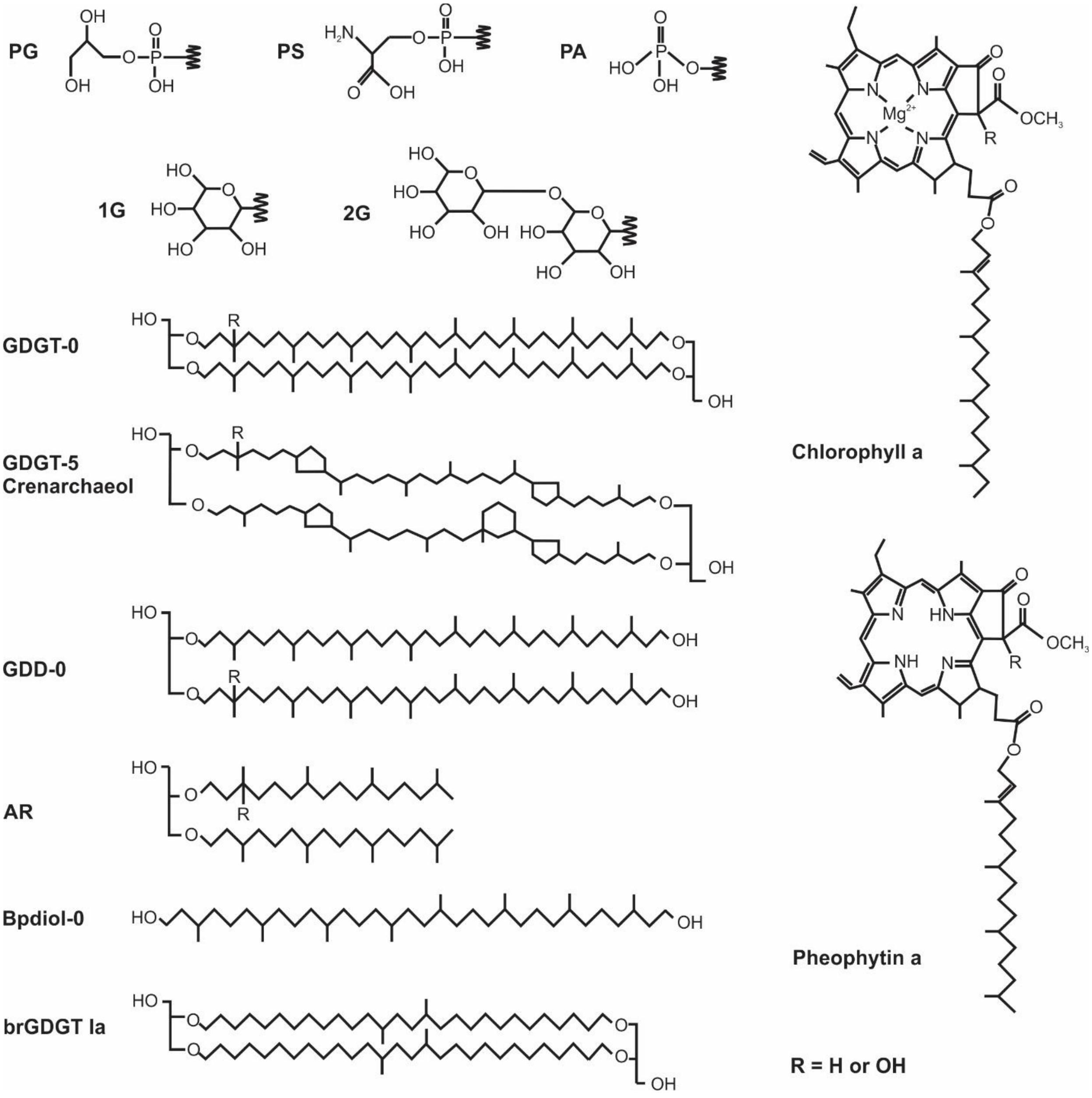

Figure 1.2: Example of core lipid structures and polar head groups identified in this study.

1.3 Study Area

The Scotian Margin is a 1200 km long passive margin stretching approximately 400 km off the coast of Nova Scotia. A horst of Paleozoic granite and troughs of Early Triassic sediment deposits make up the margin's basement. Rifting began in the Middle Triassic to the Early Jurassic, within the Appalachian Orogen, as North America separated from Africa during the Mesozoic break up of Pangea (Mosher & Wach, 2009). Late Triassic – Early Jurassic shallow marine sediments and extensive salt deposits were overlain by thick sequences of Jurassic and Cretaceous strata (Mosher et al., 2004; Weston et al., 2012). By the Late Jurassic, the margin entered fully marine conditions. Marine regression during the Cretaceous lead to the progradation of a thick sand-rich alluvial plane deposit. Chalk, marls, and shales cap off the Late Cretaceous (Beicip-Franlab & NS DNRR, 2023). Low sea level during the Tertiary resulted in an accumulation of prodeltaic shales, but also deep carvings of canyons. Rapid deposition of prodeltaic shales continued through the Pliocene terrestrial glaciation. The Scotian Margin has been dominated by proglacial sediment deposition since the first shelf crossing glaciation ~500,000 years ago to the present (Mosher et al., 2004).

Although not currently active, the Scotian Margin was once a site of oil and gas production. Commercial exploration of the Scotian Margin began in the 1960's, with most exploration and successful development occurring on the shelf in areas related to salt canopies (Kendell, 2012). The first offshore energy project, the Cohasset-Panuke project produced 44.5 million barrels of light oil. The Sable Offshore Energy Project produced over 2.09 trillion cubic feet of natural gas (Wach & Brown, 2021). Recent seismic surveys, as well as recovery of gas hydrates and light oils during sampling, have provided strong evidence of thermogenic hydrocarbon seepage, although none of these sites have been deemed economically viable (Campbell, 2019; Dong et al., 2020; Wach & Brown, 2021).

Since 2015, Natural Resources Canada, the Nova Scotia Department of Natural Resources and Renewables, Nova Scotia Offshore Energy Association, University of Calgary, and Saint Mary's University have been investigating hydrocarbon seeps on the Scotian Slope (Dong et al., 2020; Gittins et al., 2022; Beicip-Franlab & NSDNRR, 2023; Li et al., 2023; Adebayo et al., 2024; Chowdhury et al., 2024). Seismic, autonomous underwater vehicle, and remotely operated vehicle (ROV) surveys identified direct hydrocarbon indicators at site 2A-1 on the Scotian Slope. Direct hydrocarbon indicators include active gas seepage, cold seep carbonates, and a prospering ecosystem of macrofauna and microfauna (Fig. 1.3). The seep structure is elongated and orientated NW-SE, sitting approximately 1 km above a salt diapir with fault pathways extending to the surface. Authigenic carbonates are inhabited by bivalves, tubeworms, and other sessile organisms. Large microbial mats in colours of bright purples, blues, and greys are located at the edge of the seep, with smaller mats found at the seep centre. A steady stream of gas is expelled from a central depression, with some bubbles trapped as gas hydrates under a block of authigenic carbonate.

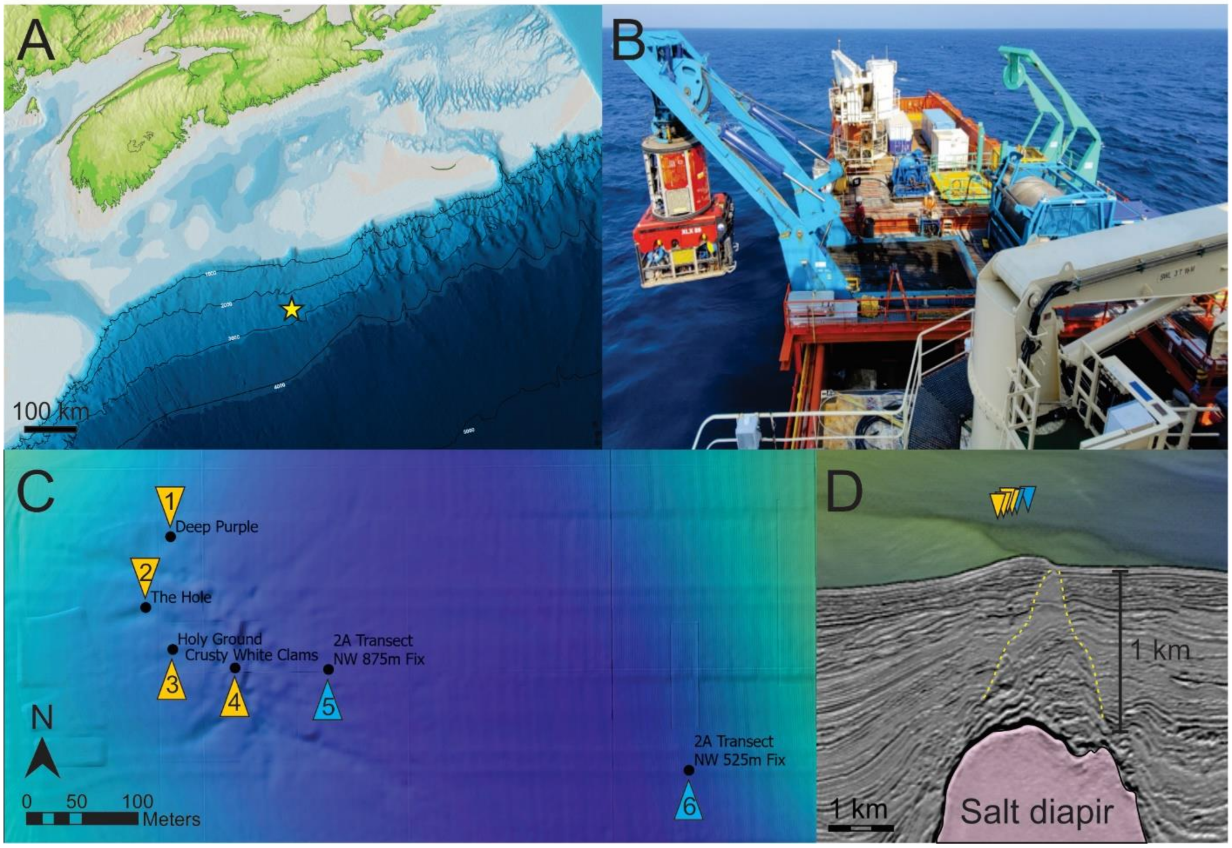

Figure 1.3: A) Site 2A-1 location on the Scotian Slope. B) Aft deck and mezzanine decks on the 2021 Atlantic Condor Expedition. The ROV is located on the left of the vessel. C) Bathymetric image at 2500 m water depth showing sampling location of push cores used in this project. D) Seismic transect near site 2A-1 showing the underlying salt diapir. Fault pathways are shown in yellow. Images modified from (Bennett & Desiage, 2022) and Natasha MacAdam (NSDNRR).

1.4 Thesis Objectives and Hypothesis Statements

The main objectives of this thesis are to 1) resolve the biogeochemical cycles and microbial dynamics within seep site 2A-1 using porewater and bulk organic geochemical as well as lipidomics-based proxies; 2) explore the spatial arrangement of sampled core sediments and determine whether large-scale patterns exist beyond the down core trends expected from individual core profiles, and 3) resolve these spatial changes to interpret the microbial metabolic seep architecture.

I hypothesize that seepage rate directly effects the microbial community inhabiting seep impacted sediments. Furthermore, I hypothesize that the hydrocarbon flow rate is not solely a vertical flux, and the seep microbial structure extends horizontally beyond the surficial boundary of the seep, largely controlled by the migration of reduced fluids. Microbial diversity is impacted by the level of chemical energy available, resulting in heterotrophic seep communities in individual cores.

1.5 Structure of Thesis

This MSc thesis is composed of four chapters: an introduction, two research chapters, and a conclusion and future work chapter. Chapter 1 introduces the reader to the study area while providing a background on deep marine cold seeps and their unique geochemical environment. The thesis objectives and hypothesis questions are outlined in this chapter. Chapter 2 summarizes the methodology used in each study. Chapter 3 describes the porewater geochemistry at Site 2A-1 and explores variations in ion diffusion fluxes and spatially resolves metabolically driven ion gradients and relationships. Chapter 4 includes a comprehensive lipidomic survey, in which 23 lipid classes were identified across six push cores. A series of lipid density heatmaps, lipid-based biomarker proxies, and porewater data from the previous chapter are combined to create a two-dimensional reconstruction of the subsurface geochemical seep architecture. Ultimately, the goal is to combine the results of Chapter 2 and 3 into a robust research paper to be submitted for publication upon the completion of this thesis. Chapter 5 summarizes the key findings of each study and provides suggestions for future work.

References

Adebayo, O., Bhatnagar, S., Webb, J., Campbell, C., Fowler, M., MacAdam, N. M., Macdonald, A., Li, C., & Hubert, C. R. J. (2024). Hydrocarbon-degrading microbial populations in permanently cold deep-sea sediments in the NW Atlantic. *Marine Pollution Bulletin*, *208*, 117052. https://doi.org/10.1016/j.marpolbul.2024.117052

Barnes, P. M., Lamarche, G., Bialas, J., Henrys, S., Pecher, I., Netzeband, G. L., Greinert, J., Mountjoy, J. J., Pedley, K., & Crutchley, G. (2010). Tectonic and geological framework for gas hydrates and cold seeps on the Hikurangi subduction margin, New Zealand. *Marine Geology*, *272*(1–4), 26–48. https://doi.org/10.1016/j.margeo.2009.03.012

Barnes, R. O., & Goldberg, E. D. (1976). Methane production and consumption in anoxic marine sediments. *Geology*, *4*(5), 297. https://doi.org/10.1130/0091-7613(1976)4<297:MPACIA>2.0.CO;2

Beicip-Franlab, & Nova Scotia Department of Natural Resources and Renewables. (2023). Scotian Basin Integration Atlas 2023, A collaborative study of stratigraphy, architecture, evolution, and geologic prospectivity. A technical collaboration with direct and indirect input provided by Canada-Nova Scotia Offshore Petroleum Board (CNSOPB), Leptis E&P, Stratum Reservoir, Weston Stratigraphic, APT (Canada) Ltd, Andrew MacRae, Bill Richards, and others. *Offshore Energy Research Association (OERA).* https://oera.ca/research/scotian-basin-integration-atlas-2023

Bennett, R., & Desiage, P.-A. (2022). Expedition report 21CONDOR: Scotian Slope, August 14-29, 2021 (8889; p. 8889). https://doi.org/10.4095/329977

Bentley, J. N., Ventura, G. T., Dalzell, C. J., Walters, C. C., Peters, C. A., Mennito, A. S., Nelson, R. K., Reddy, C. M., Seewald, J. S., & Sievert, S. M. (2022). Archaeal lipid diversity, alteration, and preservation at the Cathedral Hill deep sea hydrothermal vent, Guaymas Basin, Gulf of California, and its implications regarding the deep time preservation paradox. *Organic Geochemistry*, *163*, 104302. https://doi.org/10.1016/j.orggeochem.2021.104302

Bergé, J.-P., & Barnathan, G. (2005). Fatty Acids from Lipids of Marine Organisms: Molecular Biodiversity, Roles as Biomarkers, Biologically Active Compounds, and Economical Aspects. In R. Ulber & Y. Le Gal (Eds.), *Marine Biotechnology I* (Vol. 96, pp. 49–125). Springer Berlin Heidelberg. https://doi.org/10.1007/b135782

Blumenberg, M., Seifert, R., Reitner, J., Pape, T., & Michaelis, W. (2004). Membrane lipid patterns typify distinct anaerobic methanotrophic consortia. *Proceedings of the National Academy of Sciences*, *101*(30), 11111–11116. https://doi.org/10.1073/pnas.0401188101

Boetius, A., Ravenschlag, K., Schubert, C. J., Rickert, D., Widdel, F., Gieseke, A., Amann, R., Jørgensen, B. B., Witte, U., & Pfannkuche, O. (2000). A marine microbial consortium apparently mediating anaerobic oxidation of methane. *Nature*, *407*(6804), 623–626. https://doi.org/10.1038/35036572

Borowski, W. S., Paull, C. K., & Ussler, W. (1996). Marine pore-water sulfate profiles indicate in situ methane flux from underlying gas hydrate. *Geology*, *24*(7), 655. https://doi.org/10.1130/0091-7613(1996)024<0655:MPWSPI>2.3.CO;2

Campbell, D. C. (2019). CCGS Hudson Expedition 2016-011, phase 2. Cold seep investigations on the Scotian Slope, offshore Nova Scotia, June 15-July 6, 2016 (8525; p. 8525). https://doi.org/10.4095/313603

Canfield, D. E., Glazer, A. N., & Falkowski, P. G. (2010). The Evolution and Future of Earth's Nitrogen Cycle. *Science*, *330*(6001), 192–196. https://doi.org/10.1126/science.1186120

Cao, H., Zhang, W., Wang, Y., & Qian, P.-Y. (2015). Microbial community changes along the active seepage site of one cold seep in the Red Sea. *Frontiers in Microbiology*, *6*. https://doi.org/10.3389/fmicb.2015.00739

Cartwright, J. (2011). Diagenetically induced shear failure of fine-grained sediments and the development of polygonal fault systems. *Marine and Petroleum Geology*, *28*(9), 1593–1610. https://doi.org/10.1016/j.marpetgeo.2011.06.004

Chowdhury, A., Ventura, G. T., Owino, Y., Lalk, E. J., MacAdam, N., Dooma, J. M., Ono, S., Fowler, M., MacDonald, A., Bennett, R., MacRae, R. A., Hubert, C. R. J., Bentley, J. N., & Kerr, M. J. (2024). Cold seep formation from salt diapir–controlled deep biosphere oases. *Proceedings of the National Academy of Sciences*, *121*(12), e2316878121. https://doi.org/10.1073/pnas.2316878121

DeVries, T. (2022). The Ocean Carbon Cycle. *Annual Review of Environment and Resources*, *47*(1), 317–341. https://doi.org/10.1146/annurev-environ-120920-111307

Dickens, G. R. (2003). Rethinking the global carbon cycle with a large, dynamic and microbially mediated gas hydrate capacitor. *Earth and Planetary Science Letters*, *213*(3–4), 169–183. https://doi.org/10.1016/S0012-821X(03)00325-X

Dong, X., Rattray, J. E., Campbell, D. C., Webb, J., Chakraborty, A., Adebayo, O., Matthews, S., Li, C., Fowler, M., Morrison, N. M., MacDonald, A., Groves, R. A., Lewis, I. A., Wang, S. H., Mayumi, D., Greening, C., & Hubert, C. R. J. (2020). Thermogenic hydrocarbon biodegradation by diverse depth-stratified microbial populations at a Scotian Basin cold seep. *Nature Communications*, *11*(1), 5825. https://doi.org/10.1038/s41467-020-19648-2

Elling, F. J., Könneke, M., Nicol, G. W., Stieglmeier, M., Bayer, B., Spieck, E., de la Torre, J. R., Becker, K. W., Thomm, M., Prosser, J. I., Herndl, G. J., Schleper, C., & Hinrichs, K.-U. (2017). Chemotaxonomic characterisation of the thaumarchaeal lipidome. *Environmental Microbiology*, *19*(7), 2681–2700. https://doi.org/10.1111/1462-2920.13759

Engström, P., Dalsgaard, T., Hulth, S., & Aller, R. C. (2005). Anaerobic ammonium oxidation by nitrite (anammox): Implications for N2 production in coastal marine sediments. *Geochimica et Cosmochimica Acta*, *69*(8), 2057–2065. https://doi.org/10.1016/j.gca.2004.09.032

Giovannelli, D., d'Errico, G., Manini, E., Yakimov, M., & Vetriani, C. (2013). Diversity and phylogenetic analyses of bacteria from a shallow-water hydrothermal vent in Milos island (Greece). *Frontiers in Microbiology*, *4*. https://doi.org/10.3389/fmicb.2013.00184

Gittins, D. A., Desiage, P.-A., Morrison, N., Rattray, J. E., Bhatnagar, S., Chakraborty, A., Zorz, J., Li, C., Horanszky, O., Cramm, M. A., Bisiach, F., Bennett, R., Webb, J., MacDonald, A., Fowler, M., Campbell, D. C., & Hubert, C. R. J. (2022). Geological processes mediate a microbial dispersal loop in the deep biosphere. *Science Advances*, *8*(34), eabn3485. https://doi.org/10.1126/sciadv.abn3485

Gruber, N. (2008). The Marine Nitrogen Cycle. In *Nitrogen in the Marine Environment* (pp. 1–50). Elsevier. https://doi.org/10.1016/B978-0-12-372522-6.00001-3

Harvey, H. R., Fallon, R. D., & Patton, J. S. (1986). The effect of organic matter and oxygen on the degradation of bacterial membrane lipids in marine sediments. *Geochimica et Cosmochimica Acta*, *50*(5), 795–804. https://doi.org/10.1016/0016-7037(86)90355-8

Hinrichs, K.-U., Hayes, J. M., Sylva, S. P., Brewer, P. G., & DeLong, E. F. (1999). Methane-consuming archaebacteria in marine sediments. *Nature*, *398*(6730), 802–805. https://doi.org/10.1038/19751

Hinrichs, K.-U., Summons, R. E., Orphan, V., Sylva, S. P., & Hayes, J. M. (2000). Molecular and isotopic analysis of anaerobic methane-oxidizing communities in marine sediments. *Organic Geochemistry*, *31*(12), 1685–1701. https://doi.org/10.1016/S0146-6380(00)00106-6

Hovland, M., Gardner, J. V., & Judd, A. G. (2002). The significance of pockmarks to understanding fluid flow processes and geohazards. *Geofluids*, *2*(2), 127–136. https://doi.org/10.1046/j.1468-8123.2002.00028.x

Hovland, M., Judd, A. G., & Burke, R. A. (1993). The global flux of methane from shallow submarine sediments. *Chemosphere*, *26*(1–4), 559–578. https://doi.org/10.1016/0045-6535(93)90442-8

Jørgensen, B. B., Findlay, A. J., & Pellerin, A. (2019). The Biogeochemical Sulfur Cycle of Marine Sediments. *Frontiers in Microbiology*, *10*, 849. https://doi.org/10.3389/fmicb.2019.00849

Jørgensen, B. B., & Kasten, S. (2006). Sulfur Cycling and Methane Oxidation. In H. D. Schulz & M. Zabel (Eds.), *Marine Geochemistry* (pp. 271–309). Springer-Verlag. https://doi.org/10.1007/3-540-32144-6_8

Judd, A. G., Hovland, M., Dimitrov, L. I., García Gil, S., & Jukes, V. (2002). The geological methane budget at Continental Margins and its influence on climate change. *Geofluids*, *2*(2), 109–126. https://doi.org/10.1046/j.1468-8123.2002.00027.x

Kellermann, M. Y., Wegener, G., Elvert, M., Yoshinaga, M. Y., Lin, Y.-S., Holler, T., Mollar, X. P., Knittel, K., & Hinrichs, K.-U. (2012). Autotrophy as a predominant mode of carbon fixation in anaerobic methane-oxidizing microbial communities. *Proceedings of the National Academy of Sciences*, *109*(47), 19321–19326. https://doi.org/10.1073/pnas.1208795109

Kendell, K. L. (2012). Variations in salt expulsion style within the Sable Canopy Complex, central Scotian margin ^{1} This article is one of a series of papers published in this CJES Special Issue on the theme of *Mesozoic–Cenozoic geology of the Scotian Basin*. *Canadian Journal of Earth Sciences*, *49*(12), 1504–1522. https://doi.org/10.1139/e2012-069

Killops, S., & Killops, V. (2004). *Introduction to Organic Geochemistry* (1st ed.). Wiley. https://doi.org/10.1002/9781118697214

King, L. H., & MacLean, B. (1970). Pockmarks on the Scotian Shelf. *Geological Society of America Bulletin*, *81*(10), 3141. https://doi.org/10.1130/0016-7606(1970)81[3141:POTSS]2.0.CO;2

Kleindienst, S., Ramette, A., Amann, R., & Knittel, K. (2012). Distribution and *in situ* abundance of sulfate-reducing bacteria in diverse marine hydrocarbon seep sediments. *Environmental Microbiology*, *14*(10), 2689–2710. https://doi.org/10.1111/j.1462-2920.2012.02832.x

Knittel, K., & Boetius, A. (2009). Anaerobic Oxidation of Methane: Progress with an Unknown Process. *Annual Review of Microbiology*, *63*(1), 311–334. https://doi.org/10.1146/annurev.micro.61.080706.093130

Knittel, K., Lösekann, T., Boetius, A., Kort, R., & Amann, R. (2005). Diversity and Distribution of Methanotrophic Archaea at Cold Seeps. *Applied and Environmental Microbiology*, *71*(1), 467–479. https://doi.org/10.1128/AEM.71.1.467-479.2005

Koga, Y., & Morii, H. (2005). Recent Advances in Structural Research on Ether Lipids from Archaea Including Comparative and Physiological Aspects. *Bioscience, Biotechnology, and Biochemistry*, *69*(11), 2019–2034. https://doi.org/10.1271/bbb.69.2019

Kohl, S. D., & Rice, J. A. (1999). Contribution of lipids to the nonlinear sorption of polycyclic aromatic hydrocarbons to soil organic matter. *Organic Geochemistry*, *30*(8), 929–936. https://doi.org/10.1016/S0146-6380(99)00076-5

Kulm, L. D., Suess, E., Moore, J. C., Carson, B., Lewis, B. T., Ritger, S. D., Kadko, D. C., Thornburg, T. M., Embley, R. W., Rugh, W. D., Massoth, G. J., Langseth, M. G., Cochrane, G. R., & Scamman, R. L. (1986). Oregon Subduction Zone: Venting, Fauna, and Carbonates. *Science*, *231*(4738), 561–566. https://doi.org/10.1126/science.231.4738.561

Kvenvolden, K. A., & Cooper, C. K. (2003). Natural seepage of crude oil into the marine environment. *Geo-Marine Letters*, *23*(3–4), 140–146. https://doi.org/10.1007/s00367-003-0135-0

Kvenvolden, K. A., & Rogers, B. W. (2005). Gaia's breath—Global methane exhalations. *Marine and Petroleum Geology*, *22*(4), 579–590. https://doi.org/10.1016/j.marpetgeo.2004.08.004

Langworthy, T. A., Holzer, G., Zeikus, J. G., & Tornabene, T. G. (1983). Iso- and Anteiso-Branched Glycerol Diethers of the Thermophilic Anaerobe Thermodesulfotobacterium commune. *Systematic and Applied Microbiology*, *4*(1), 1–17. https://doi.org/10.1016/S0723-2020(83)80029-0

Li, C., Adebayo, O., Ferguson, D. K., Wang, S., Rattray, J. E., Fowler, M., Webb, J., Campbell, C., Morrison, N., MacDonald, A., & Hubert, C. R. J. (2023). Bacterial anomalies associated with deep sea hydrocarbon seepage along the Scotian Slope. *Deep Sea Research Part I: Oceanographic Research Papers*, *193*, 103955. https://doi.org/10.1016/j.dsr.2022.103955

Lipp, J. S., & Hinrichs, K.-U. (2009). Structural diversity and fate of intact polar lipids in marine sediments. *Geochimica et Cosmochimica Acta*, *73*(22), 6816–6833. https://doi.org/10.1016/j.gca.2009.08.003

Lipp, J. S., Morono, Y., Inagaki, F., & Hinrichs, K.-U. (2008). Significant contribution of Archaea to extant biomass in marine subsurface sediments. *Nature*, *454*(7207), 991–994. https://doi.org/10.1038/nature07174

Lv, Y., Yang, S., Xiao, X., & Zhang, Y. (2022). Stimulated Organic Carbon Cycling and Microbial Community Shift Driven by a Simulated Cold-Seep Eruption. *mBio*, *13*(2), e00087-22. https://doi.org/10.1128/mbio.00087-22

MacDonald, I. R., Guinasso, Jr., N. L., Sassen, R., Brooks, J. M., Lee, L., & Scott, K. T. (1994). Gas hydrate that breaches the sea floor on the continental slope of the Gulf of Mexico. *Geology*, *22*(8), 699. https://doi.org/10.1130/0091-7613(1994)022<0699:GHTBTS>2.3.CO;2

Mosher, D. C., Piper, D. J. W., Calvin Campbell, D., & Jenner, K. A. (2004). Near-surface geology and sediment-failure geohazards of the central Scotian Slope. *AAPG Bulletin*, *88*(6), 703–723. https://doi.org/10.1306/01260403084

Niemann, H., & Elvert, M. (2008). Diagnostic lipid biomarker and stable carbon isotope signatures of microbial communities mediating the anaerobic oxidation of methane with sulphate. *Organic Geochemistry*, *39*(12), 1668–1677. https://doi.org/10.1016/j.orggeochem.2007.11.003

Niemann, H., Lösekann, T., De Beer, D., Elvert, M., Nadalig, T., Knittel, K., Amann, R., Sauter, E. J., Schlüter, M., Klages, M., Foucher, J. P., & Boetius, A. (2006). Novel microbial communities of the Haakon Mosby mud volcano and their role as a methane sink. *Nature*, *443*(7113), 854–858. https://doi.org/10.1038/nature05227

Niu, M., Fan, X., Zhuang, G., Liang, Q., & Wang, F. (2017). Methane-metabolizing microbial communities in sediments of the Haima cold seep area, northwest slope of the South China Sea. *FEMS Microbiology Ecology*. https://doi.org/10.1093/femsec/fix101

Orcutt, B. N., Joye, S. B., Kleindienst, S., Knittel, K., Ramette, A., Reitz, A., Samarkin, V., Treude, T., & Boetius, A. (2010). Impact of natural oil and higher hydrocarbons on microbial diversity, distribution, and activity in Gulf of Mexico cold-seep sediments. *Deep Sea Research Part II: Topical Studies in Oceanography*, *57*(21–23), 2008–2021. https://doi.org/10.1016/j.dsr2.2010.05.014

Orphan, V. J., Hinrichs, K.-U., Ussler, W., Paull, C. K., Taylor, L. T., Sylva, S. P., Hayes, J. M., & Delong, E. F. (2001a). Comparative Analysis of Methane-Oxidizing Archaea and Sulfate-Reducing Bacteria in Anoxic Marine Sediments. *Applied and Environmental Microbiology*, *67*(4), 1922–1934. https://doi.org/10.1128/AEM.67.4.1922-1934.2001

Orphan, V. J., House, C. H., Hinrichs, K.-U., McKeegan, K. D., & DeLong, E. F. (2001b). Methane-Consuming Archaea Revealed by Directly Coupled Isotopic and Phylogenetic Analysis. *Science*, *293*(5529), 484–487. https://doi.org/10.1126/science.1061338

Peckmann, J., & Thiel, V. (2004). Carbon cycling at ancient methane–seeps. *Chemical Geology*, *205*(3–4), 443–467. https://doi.org/10.1016/j.chemgeo.2003.12.025

Reeburgh, W. S. (2007). Oceanic Methane Biogeochemistry. *Chemical Reviews*, *107*(2), 486–513. https://doi.org/10.1021/cr050362v

Regnier, P., Dale, A. W., Arndt, S., LaRowe, D. E., Mogollón, J., & Van Cappellen, P. (2011). Quantitative analysis of anaerobic oxidation of methane (AOM) in marine sediments: A modeling perspective. *Earth-Science Reviews*, *106*(1), 105–130. https://doi.org/10.1016/j.earscirev.2011.01.002

Ritger, S., Carson, B., & Suess, E. (1987). Methane-derived authigenic carbonates formed by subduction-induced pore-water expulsion along the Oregon/Washington margin. *Geological Society of America Bulletin*, *98*(2), 147. https://doi.org/10.1130/0016-7606(1987)98<147:MACFBS>2.0.CO;2

Rossel, P. E., Lipp, J. S., Fredricks, H. F., Arnds, J., Boetius, A., Elvert, M., & Hinrichs, K.-U. (2008). Intact polar lipids of anaerobic methanotrophic archaea and associated bacteria. *Organic Geochemistry*, *39*(8), 992–999. https://doi.org/10.1016/j.orggeochem.2008.02.021

Rubelmann, H., Karlen, D. J., & Garey, J. R. (2017). Changes in Eukaryotic and Bacterial Communities along a 120 m Transect Associated with a Shallow Marine Hydrothermal Vent. *Frontiers in Marine Science*, *4*, 177. https://doi.org/10.3389/fmars.2017.00177

Schippers, A., & Neretin, L. N. (2006). Quantification of microbial communities in near-surface and deeply buried marine sediments on the Peru continental margin using real-time PCR. *Environmental Microbiology*, *8*(7), 1251–1260. https://doi.org/10.1111/j.1462-2920.2006.01019.x

Schubotz, F., Wakeham, S. G., Lipp, J. S., Fredricks, H. F., & Hinrichs, K. (2009). Detection of microbial biomass by intact polar membrane lipid analysis in the water column and surface sediments of the Black Sea. *Environmental Microbiology*, *11*(10), 2720–2734. https://doi.org/10.1111/j.1462-2920.2009.01999.x

Sen, A., Åström, E. K. L., Hong, W.-L., Portnov, A., Waage, M., Serov, P., Carroll, M. L., & Carroll, J. (2018). Geophysical and geochemical controls on the megafaunal community of a high Arctic cold seep. *Biogeosciences*, *15*(14), 4533–4559. https://doi.org/10.5194/bg-15-4533-2018

Sievert, S. M., Brinkhoff, T., Muyzer, G., Ziebis, W., & Kuever, J. (1999). Spatial Heterogeneity of Bacterial Populations along an Environmental Gradient at a Shallow Submarine Hydrothermal Vent near Milos Island (Greece). *Applied and Environmental Microbiology*, *65*(9), 3834–3842. https://doi.org/10.1128/AEM.65.9.3834-3842.1999

Sturt, H. F., Summons, R. E., Smith, K., Elvert, M., & Hinrichs, K. (2004). Intact polar membrane lipids in prokaryotes and sediments deciphered by high-performance liquid chromatography/electrospray ionization multistage mass spectrometry—New biomarkers for biogeochemistry and microbial ecology. *Rapid Communications in Mass Spectrometry*, *18*(6), 617–628. https://doi.org/10.1002/rcm.1378

Suess, E. (2020). Marine Cold Seeps: Background and Recent Advances. In H. Wilkes (Ed.), *Hydrocarbons, Oils and Lipids: Diversity, Origin, Chemistry and Fate* (pp. 747–767). Springer International Publishing. https://doi.org/10.1007/978-3-319-90569-3_27

Summons, R. E., Welander, P. V., & Gold, D. A. (2022). Lipid biomarkers: Molecular tools for illuminating the history of microbial life. *Nature Reviews Microbiology*, *20*(3), 174–185. https://doi.org/10.1038/s41579-021-00636-2

Talukder, A. R. (2012). Review of submarine cold seep plumbing systems: Leakage to seepage and venting. *Terra Nova*, *24*(4), 255–272. https://doi.org/10.1111/j.1365-3121.2012.01066.x

Teske, A., Hinrichs, K.-U., Edgcomb, V., De Vera Gomez, A., Kysela, D., Sylva, S. P., Sogin, M. L., & Jannasch, H. W. (2002). Microbial Diversity of Hydrothermal Sediments in the Guaymas Basin: Evidence for Anaerobic Methanotrophic Communities. *Applied and Environmental Microbiology*, *68*(4), 1994–2007. https://doi.org/10.1128/AEM.68.4.1994-2007.2002

Thiel, V., Peckmann, J., Richnow, H. H., Luth, U., Reitner, J., & Michaelis, W. (2001). Molecular signals for anaerobic methane oxidation in Black Sea seep carbonates and a microbial mat. *Marine Chemistry*, *73*(2), 97–112. https://doi.org/10.1016/S0304-4203(00)00099-2

Vairavamurthy, M. A., Orr, W. L., & Manowitz, B. (1995). Geochemical Transformations of Sedimentary Sulfur: An Introduction. In *Geochemical Transformations of Sedimentary Sulfur* (Vol. 612, pp. 1–14). American Chemical Society. https://doi.org/10.1021/bk-1995-0612.ch001

Valentine, D. L. (2007). Adaptations to energy stress dictate the ecology and evolution of the Archaea. *Nature Reviews Microbiology*, *5*(4), 316–323. https://doi.org/10.1038/nrmicro1619

Vanreusel, A., Andersen, A., Boetius, A., Connelly, D., Cunha, M., Decker, C., Heeschen, K., Hilario, A., Kormas, K., Maignien, L., Olu, K., Pachiadaki, M., Ritt, B., Rodrigues, C., Sarrazin, J., Tyler, P., Van Gaever, S., & Vanneste, H. (2009). Biodiversity of Cold Seep Ecosystems Along the European Margins. *Oceanography*, *22*(1), 110–127. https://doi.org/10.5670/oceanog.2009.12

Wegener, G., Kellermann, M. Y., & Elvert, M. (2016). Tracking activity and function of microorganisms by stable isotope probing of membrane lipids. *Current Opinion in Biotechnology*, *41*, 43–52. https://doi.org/10.1016/j.copbio.2016.04.022

Wei, J., Li, J., Wu, T., Zhang, W., Li, J., Wang, J., Tao, J., Chen, Z., Wu, Z., & Chen, W. (2020). Geologically controlled intermittent gas eruption and its impact on bottom water temperature and chemosynthetic communities—A case study in the “HaiMa” cold seeps, South China Sea. *Geological Journal*, *55*(9), 6066–6078. https://doi.org/10.1002/gj.3780

Weston, J. F., MacRae, R. A., Ascoli, P., Cooper, M. K. E., Fensome, R. A., Shaw, D., & Williams, G. L. (2012). A revised biostratigraphic and well-log sequence-stratigraphic framework for the Scotian Margin, offshore eastern Canada ^{1} This article is one of a series of papers published in this CJES Special Issue on the theme of *Mesozoic–Cenozoic* *geology of the Scotian Basin*. ^{2} Earth Sciences Sector Contribution 20120137. *Canadian Journal of Earth Sciences*, *49*(12), 1417–1462. https://doi.org/10.1139/e2012-070

White, D. C., Davis, W. M., Nickels, J. S., King, J. D., & Bobbie, R. J. (1979). Determination of the sedimentary microbial biomass by extractible lipid phosphate. *Oecologia*, *40*(1), 51–62. https://doi.org/10.1007/BF00388810

Zhang, Z.-X., Li, J., Chen, Z., Sun, Z., Yang, H., Fu, M., & Peng, X. (2020). The effect of methane seeps on the bacterial tetraether lipid distributions at the Okinawa Trough. *Marine Chemistry*, *225*, 103845. https://doi.org/10.1016/j.marchem.2020.103845

Ziervogel, K., D'Souza, N., Sweet, J., Yan, B., & Passow, U. (2014). Natural oil slicks fuel surface water microbial activities in the northern Gulf of Mexico. *Frontiers in Microbiology*, *5*. https://doi.org/10.3389/fmicb.2014.00188

Chapter 2: Methodology

Cold seeps are unique environmental systems with fluctuating geochemical conditions and complex microbial communities. Correct sampling techniques, careful storage, and appropriate analyses are crucial in ensuring that no alteration or degradation of the sediment, porewater, or lipidome occurs. The methodology outlined in the following chapter aligns with research objectives to produce accurate and representative data of the geochemical architecture of a Scotian Slope cold seep.

2.1 Sample Collection

Previous expeditions on the Scotian Slope collected samples using piston, box, and gravity cores at prospective seepage sites (Campbell, 2019; Campbell & Normandeau, 2019). These cores provided sediments up to ~ 900 *cm below the seafloor* (cmbsf) but presented unique challenges in sampling accuracy. Gravity and piston cores are susceptible to lateral drift post-deployment and can penetrate the sediment at an angle, compromising the spatial accuracy of the cores. Upon impact with the seabed, piston and gravity cores disturb the shallow sediment. This causes frequent loss of surface sediment stratigraphy when using these techniques. Push coring, while explicitly targeted and capable of preserving the shallow sediment stratigraphy, is limited to very shallow sediment depths (typically <50 cm) and can require a submersible to enable sample collection.

The 2021 Atlantic Condor Expedition used a remotely operated vehicle (ROV) to conduct a video mapping and push coring survey. Prospective seep site localities were selected based on prior autonomous underwater vehicle (AUV) surveys completed during 2018 and 2020 aboard the CCSG Hudson and promising geochemical results from 2016 and 2018 expeditions (Campbell, 2019; Campbell & Normandeau, 2019).

A transect of 6 push cores was collected at seep site 2A-1 at ~2500 m water depth along the Scotian Slope, offshore Nova Scotia using a Triton XLX ROV (Helix Robotics Solutions Ltd.), during the 2021 Atlantic Condor Expedition (Fig. 2.1; Table 2.1). The transect was composed of four cores at geologically interesting sites (termed hotspots) within the seep that hosted diverse communities of microbial mats and bivalves, and two cores located further southeast at ~125 m and ~500 m outside the seep into ambient sediment (Chapter 1, Fig. 1.3). The push cores were labeled based on a distinct feature from the sample location. Upon collection, the push cores were subsampled into 2 cm intervals, wrapped in baked aluminium foil, and stored in a -80 °C freezer until analysis.

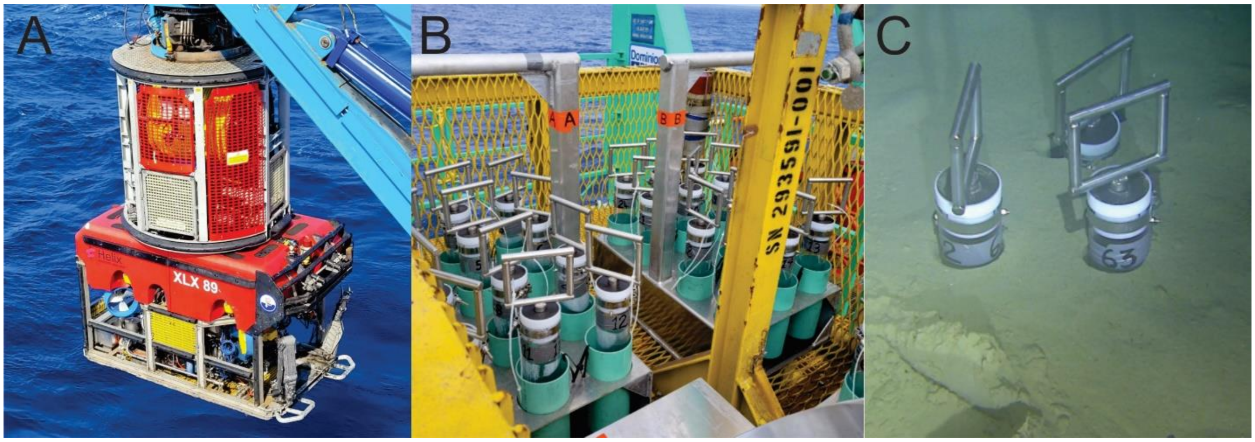

Figure 2.1: A) Triton XLX ROV pre-deployment. B) Push core quivers loaded for deployment. C) Push core sampling in progress. Images modified from (Bennett & Desiage, 2022).

Table 2.1: Summary of sample set of the 2A-1 seep transect study.

Core Name	Core Number	Location (Lat., Long.)	Water Depth (m)
Deep Purple	1	42.163275, -62.372022	2685.890
The Hole	2	42.162698, -62.372356	2687.468
Holey Ground	3	42.162353, -62.302762	2688.398
Crusty White Clams	4	42.162198, -62.371378	2684.392
NW875m	5	42.162180, -62.370351	2685.503
Midpoint	6	42.161334, -62.366394	2693.491

2.2 Geochemical Surveys

2.2.1 Sedimentary carbon analysis

2.2.1.1 Bulk total organic and inorganic carbon

The total organic carbon (TOC) content of marine sediments can be used to trace organic matter sources (Redfield, 1934; Körtzinger et al., 2001), diagenesis (Berner, 1980; McArthur et al., 1992), and preservation (Hedges & Keil, 1995) in the marine environment. Elevated TOC and depleted $\delta^{13}C_{TOC}$ in marine sediments can indicate the presence of hydrocarbon seepage and provide insights into organic matter cycling (Joye et al., 2004; Zonneveld et al., 2010; Joye, 2020).

Total organic carbon and particulate inorganic carbon (PIC) were measured across the seep transect. The procedure roughly followed the protocol outlined by Kahn, (1988), with a modification of the acid used during the decarbonization stage. Frozen sediment was dried at 35 °C and decarbonated using 6N HCl for 24h. Decarbonated sediment was neutralized using deionized water. Once neutral, the sediment was dried again at 35 °C and stored at 4 °C until analysis. Particulate inorganic carbon was calculated as the difference in weight during the decarbonization stage of the procedure. Total organic carbon was measured using a Perkin-Elmer 2400 Series II CHNS/O Elemental Analyzer programed for CHN analysis located in the Centre for Environmental Analysis and Remediation (Halifax, Nova Scotia).

2.2.1.2 Carbon isotope analyses

Bulk organic stable carbon isotope measurements were obtained for 13 samples across 4 cores. Measurements were obtained by Continuous Flow-Elemental Analysis-Isotope Ratio Mass Spectrometry at the Isotope Science Laboratory at the University of Calgary. Stable isotope ratios are expressed using delta (δ) and measured as the part per mill (‰) difference between the sample and the ‘Vienna Peedee Belemnite’ formation for carbon (Craig, 1957). Four samples were used for radiocarbon analysis to obtain the age and down-core sedimentation rates for ambient sediments outside the seep structure. Radiocarbon measurements were provided by the André E. Lalonde AMS Laboratory at the University of Ottawa. Samples were prepared following the methods outlined in Crann et al., (2017) and Murseli et al. (2019). Measurements were obtained using an Ionplus AG MICADAS (Mini Carbon Dating System) and reported in ^{14}C yr BP (BP = AD 1950).

2.2.2 Porewater Analysis

2.2.2.1 Porewater extraction

Porewater can be extracted from marine sediments through a variety of methods including vacuum filtration, rhizon sampling, dialysis passive sampling or peepers, and centrifugation. Among these, centrifugation is among the fastest and can extract large volumes depending on sediment porosity. Vacuum filtration requires specialized equipment unavailable for this project. Both rhizon sampling and peepers require long extraction times and yield small quantities of porewater (Seeberg-Elverfeldt et al., 2005; Risacher et al., 2023). Porewater was therefore extracted from defrosted sediment via centrifugation at 2500 rpm for 10 min. The porewater was decanted into a pre-combusted glass beaker, then filtered through a 0.45-µm filter to remove sediment particles. The exact volume of extracted porewater was recorded as a measure of sediment porosity.

2.2.2.2 Ion chromatography

Ion chromatography is a liquid chromatographic technique that separates ions in solution based on their interaction with an ion-exchange resin within a column. A Thermo Scientific Dionex Aquion Chromatography Conductivity System set up is available at Saint Mary's University Organic Geochemistry Laboratory (OGL). The IC used in this study was equipped with an anion exchange column, where the resin hosted positively charged groups to bind the anions. Elution along the column occurs in order of attraction, based on the anions charge and size, with anions with weaker attraction eluting first followed by those with a stronger attraction. As the anions exit the column, a conductivity detector generates a signal proportional to the anion's concentration. The signals are recorded as chromatographic peaks which are integrated to measure each anion's concentration. Standard addition and external calibration are two common methods for measuring integrated ion concentrations. Standard addition requires multiple aliquots of the same sample to be run with increasing amounts of standard solution to create a calibration curve. This process is time inefficient in comparison to external calibration, which only requires a single run for each sample. A seven-anion standard mixture was diluted to 0.5, 1, 2, 5, 10, 20, and 50 ppm to generate an external calibration curve to measure concentrations of F^-, NO_2^-, NO_3^-, $CO_3^{2-} + HCO^-$, and SO_4^{2-}. The IC system used cannot discriminate independent signals of CO_3^{2-} and HCO_3^- which are recorded as a signal peak, henceforth referred to a dissolved inorganic carbon (DIC). The integrated peak area of each ion on the chromatogram is plugged into the regression equation generated by the calibration curve.

The high salinity of marine porewater requires that the system be equipped with two in-line guard cartridges to remove chloride (Cl^-) and sodium (Na^+) ions from the sample before reaching the anion-exchange column. While detection is suppressed, a large Cl^- signal is still recorded on the chromatogram. In addition to adjustments to the IC, porewater samples are diluted 5× prior to injection to prevent Cl^- and Na^+ from overwhelming the system.

2.2.2.3 Photometry

Photometry is a simple and cost-effective supplementary method for measuring low concentration ions in marine porewater. Photometry measures ion concentrations in solution based on the absorption of light by the sample. The addition of reagents to the porewater sample forms coloured complexes that absorb light at specific wavelengths, which is proportional to the concentration of the ion. Cation quantification via IC would require the system to be equipped with a cation exchange column, but photometry can be completed concurrently within a singular IC sample run. Prior to analysis, a calibration curve is constructed through a series of absorbance measurements from calibration standards (420, 466, 525, 575, and 610 nm ± 0.02 abs). A Hanna Instruments HI-83300 Multiparameter Photometer and Hanna Instruments Indication Solutions were used to measure concentrations of NH_4^+, Fe^{2+}, Mn^{2+}, and PO_4^{3-}. Limited porewater availability required 1-4 ml aliquots of porewater to be diluted in de-ionized water to a total volume of 10 ml. Concentration readings were re-calculated to account for individual dilution factors.

2.2.3 Lipidomic Analysis

2.2.3.1 Lipid extraction

Membrane lipids in environmental samples can be found as fossilized core lipids (CLs) or as intact polar lipids (IPLs), with a polar head group attached. Intact polar lipids are considered to be the products of living cells, and upon cellular death, rapidly degrade to a more stable CL (White et al., 1979; Sturt et al., 2004). Core lipids are non-polar and therefore insoluble in a polar solvent like water, while IPLs are amphipathic in nature. The labile nature of IPLs requires modifications to traditional Bligh & Dyer (1959) extraction protocols to effectively isolate IPLs and CLs from marine sediments. The modified liquid-liquid extraction process utilizes a series of three organic solvent mixtures, adjusted with buffers to maintain pH stability, aptly referred to as Mix A, B, and C, to extract the lipids during a six-step process (Fig. 1.4). Another modification from the original extraction protocol is the replacement of chloroform with dichloromethane (DCM). In comparison to other lipid extraction techniques, such as Soxhlet and accelerated solvent extraction, the MBD technique is recommended to recover an unbiased lipidome (Lengger et al., 2012).

Total lipid extracts (TLEs) were collected for 76 sediment samples through modified Bligh and Dyer (MBD) extractions as outlined in (Bentley et al., 2022). Mix A and B are a methanol (MeOH)/dichloromethane (DCM)/buffer [2:1:0.8; v/v] mix designed to extract a wide range of lipid classes. Mix C is a MeOH/DCM [5:1; v/v] mix used to remove any residual lipids from the sediment matrix. Each extraction step used 40 ml of mix, which was sonicated then centrifuged, each for 5 minutes. Once the organic fraction was isolated in the combined solvent mixtures, it was further washed with milli-Q water (≥ 18.2 MΩ cm) to remove any water-soluble impurities that may have been drawn into the organic fraction during extraction. The organic fraction is immiscible in water, which phase separates. The remaining organic fraction contains purified lipids, which enables cleaner chromatographic separation during analysis.

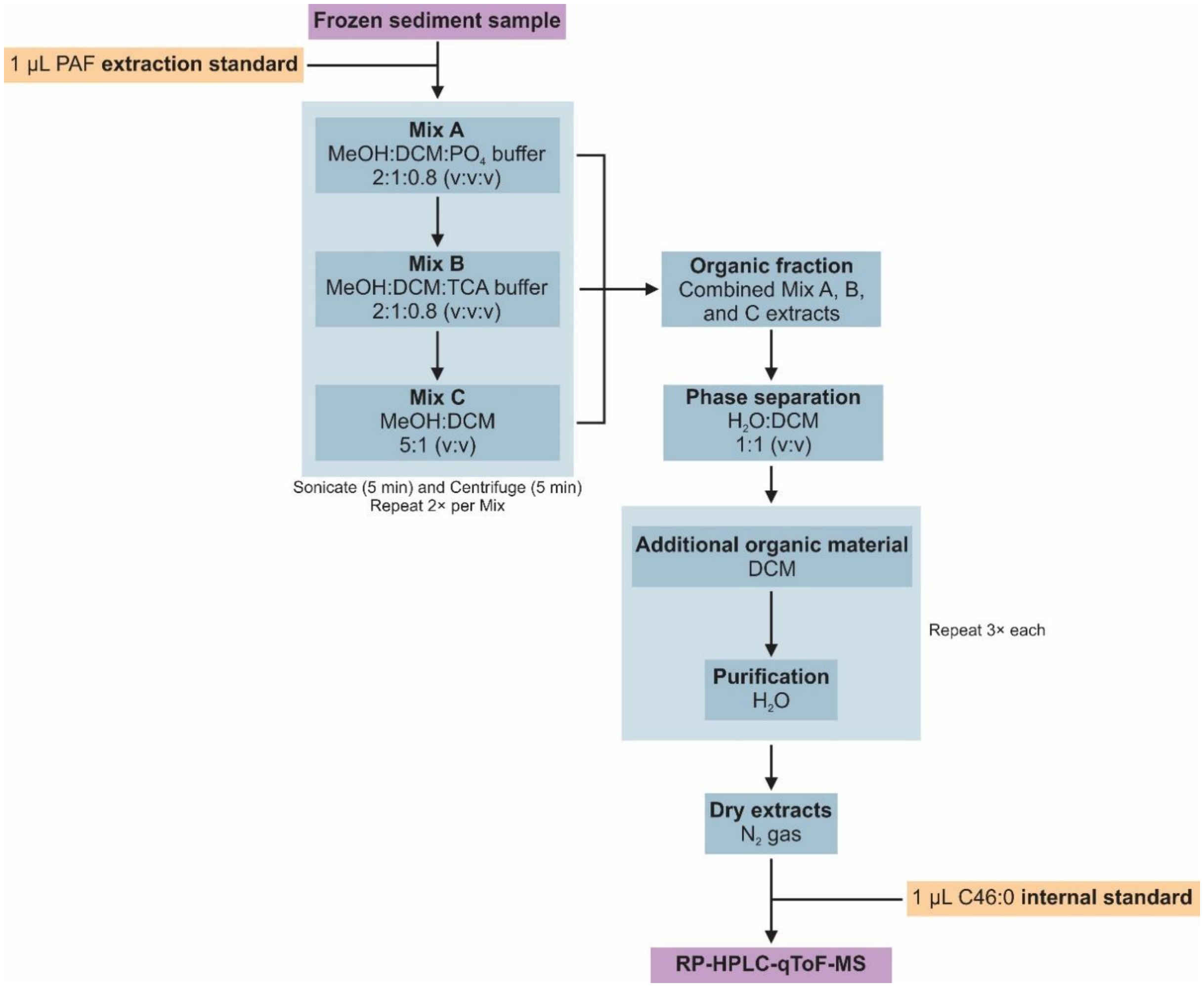

Figure 2.1: Modified Bligh and Dyer (1959) extraction protocol.

2.2.3.2 Lipid analysis

High-performance liquid chromatography coupled to mass spectrometry (HPLC-MS) has been employed to analyze the in situ microbial community in marine sediments based on membrane lipids. HPLC-MS is favourable for resolving complex lipid mixtures over more traditional genomic studies, such as metagenomics, as it enables simultaneous detection and quantification of in situ IPLs and CLs (Fang & Barcelona, 1998; Rütters et al., 2002; Sturt et al., 2004). This analytical technique separates lipid classes based on their polarity and provides structural information and quantitative measurements for targeted and untargeted surveys.

An aliquot representing 3% of the samples TLE was injected into an Agilent 1260 infinity ultrahigh performance liquid chromatograph coupled to an Agilent Technologies 6530 quadrupole time of flight mass spectrometer (UHPLC-qToF-MS). Reverse phase liquid chromatography (RPLC) uses a polar mobile phase to move the injected sample through a non-polar stationary phase. In this work, a ZORBAX RRHD Eclipse Plus C18 column was used. For this study, two mobile phases, and the use of gradient elution, was used to decrease the polarity of the mobile phase during the separation to enhance resolution. Under these conditions, elution in the column occurs in the order of decreasing polarity. The most polar lipids elude rapidly through the column, followed by less polar lipids that interact longer with the stationary phase. A chromatogram of each 85-min run displays present lipid classes in order of decreasing polarity. Lipids exit the column and are further analysed by electrospray ionization mass spectrometry (ESI-MS), which ionizes the lipids and measures their mass-to-charge (*m/z*) ratio, generating characteristic mass spectra for each class. The scan range for the ESI-MS was set to 100-3000 *m/z.* Samples were run in a randomized order with analytical blanks inserted every 7–10 sample injections. Quantitation is presented as $\mu g \cdot g^{-1}$ of sediment to normalize each lipid to the extracted sample sediment volume.

2.2.3.3 Lipid Quantification

Analyte identification was achieved by mass spectral analysis via spectra with accurate mass resolution and by direct comparison of fragmentation patterns presented in the literature using Agilent Technologies MassHunter 10.0 software. Lipids of interest were identified by their molecular ions and respective fragmentation patterns. Electrospray ionization leads to the formation of adducts, as a result of neutral molecules receiving a charge. Lipid quantification was accomplished by summing the integrated peak areas of the $[M+H]^+$, $[M+NH_4]^+$, and $[M+Na]^+$ adducts (Wörmer et al., 2015; Bentley et al., 2022). Lipid concentrations were calculated relative to the C46:0 internal standard (Eq. 2) and reported in $ug \cdot g^{-1}$ sediment weight.

$$Concentration_{Lipid} = \left(\frac{Mass_{Std} \times Area_{Lipid}}{Area_{Std} \times Mass_{Lipid}}\right) \times Dilution\ \% \qquad (2)$$

2.2.4 Statistical Analysis

The size of the data set required a multivariate statistical analysis to reduce the dimensionality of the data and reveal underlying patterns. Principal component analysis (PCA) was selected over multidimensional scaling, as PCA is more practical for high-dimensional data and retains the maximum variance possible in fewer dimensions. Principal component analysis was carried out using the "factomineR" package in RStudio (Version 4.3.2). The Kaiser-Meyer-Olkin (KMO) test of sampling adequacy and Barlett's test of sphericity were employed to ensure the datasets suitability for PCA. A KMO score above 0.6 and a p-value less than 0.05 for Barlett's test indicate that PCA is appropriate. A scree plot was generated to determine the number of principal components to retain to capture the most significant variance. Results are visualized using the "factoextra" package.

2.3 Conclusions

The extraction techniques and analytical methods outlined above are designed to accurately measure sedimentary carbon, porewater ions, and microbial lipids from cold seep sediments. Ion chromatography can measure a range of anions, which are complimented by specific cations measured by photometry. The dual-analytical approach is time-effective for the large sample set covered in this project. The MBD extraction protocols have been effectively modified to recover TLEs from marine sediments, preserving the labile IPL structures. Employing RP-HPLC-ESI-MS as the analytical technique enables identification and quantification of lipidome at Site 2A-1. Together, these methods are ideally suited to resolve the thesis objectives and address the hypotheses stated in Chapter 1.

References

Bennett, R., & Desiage, P.-A. (2022). Expedition report 21CONDOR: Scotian Slope, August 14-29, 2021 (8889; p. 8889). https://doi.org/10.4095/329977

Bentley, J. N., Ventura, G. T., Dalzell, C. J., Walters, C. C., Peters, C. A., Mennito, A. S., Nelson, R. K., Reddy, C. M., Seewald, J. S., & Sievert, S. M. (2022). Archaeal lipid diversity, alteration, and preservation at the Cathedral Hill deep sea hydrothermal vent, Guaymas Basin, Gulf of California, and its implications regarding the deep time preservation paradox. *Organic Geochemistry*, *163*, 104302. https://doi.org/10.1016/j.orggeochem.2021.104302

Berner, R. A. (1980). *Early diagenesis: A theoretical approach*. Princeton University Press.

Bligh, E. G., & Dyer, W. J. (1959). A rapid method of total lipid extraction and purification. *Canadian Journal of Biochemistry and Physiology*, *37*(8), 911–917. https://doi.org/10.1139/o59-099

Campbell, D. C. (2019). CCGS Hudson Expedition 2016-011, phase 2. Cold seep investigations on the Scotian Slope, offshore Nova Scotia, June 15-July 6, 2016 (8525; p. 8525). https://doi.org/10.4095/313603

Campbell, D. C., & Normandeau, A. (2019). CCGS Hudson Expedition 2018-041: High-resolution investigation of deep-water seabed seeps and landslides along the Scotian Slope, offshore Nova Scotia, May 26 - June 15, 2018 (8567; p. 8567). https://doi.org/10.4095/314695

Craig, H. (1957). Isotopic standards for carbon and oxygen and correction factors for mass-spectrometric analysis of carbon dioxide. *Geochimica et Cosmochimica Acta*, *12*(1–2), 133–149. https://doi.org/10.1016/0016-7037(57)90024-8

Fang, J., & Barcelona, M. J. (1998). Structural determination and quantitative analysis of bacterial phospholipids using liquid chromatography/electrospray ionization/mass spectrometry. *Journal of Microbiological Methods*, *33*(1), 23–35. https://doi.org/10.1016/S0167-7012(98)00037-2

Hedges, J. I., & Keil, R. G. (1995). Sedimentary organic matter preservation: An assessment and speculative synthesis. *Marine Chemistry*, *49*(2–3), 81–115. https://doi.org/10.1016/0304-4203(95)00008-F

Joye, S. B. (2020). The Geology and Biogeochemistry of Hydrocarbon Seeps. *Annual Review of Earth and Planetary Sciences*, *48*(1), 205–231. https://doi.org/10.1146/annurev-earth-063016-020052

Joye, S. B., Boetius, A., Orcutt, B. N., Montoya, J. P., Schulz, H. N., Erickson, M. J., & Lugo, S. K. (2004). The anaerobic oxidation of methane and sulfate reduction in sediments from Gulf of Mexico cold seeps. *Chemical Geology*, *205*(3–4), 219–238. https://doi.org/10.1016/j.chemgeo.2003.12.019

Kahn, L. (1988). *Determination of Total Organic Carbon in Sediment*. USEPA, Region II.

Körtzinger, A., Hedges, J. I., & Quay, P. D. (2001). Redfield ratios revisited: Removing the biasing effect of anthropogenic CO_2. *Limnology and Oceanography*, *46*(4), 964–970. https://doi.org/10.4319/lo.2001.46.4.0964

Lengger, S. K., Hopmans, E. C., Sinninghe Damsté, J. S., & Schouten, S. (2012). Comparison of extraction and work up techniques for analysis of core and intact polar tetraether lipids from sedimentary environments. *Organic Geochemistry*, *47*, 34–40. https://doi.org/10.1016/j.orggeochem.2012.02.009

McArthur, J. M., Tyson, R. V., Thomson, J., & Mattey, D. (1992). Early diagenesis of marine organic matter: Alteration of the carbon isotopic composition. *Marine Geology*, *105*(1–4), 51–61. https://doi.org/10.1016/0025-3227(92)90181-G

Redfield, A. C. (1934). On the Proportions of Organic Derivatives in Sea Water and Their Relation to the Composition of Plankton. *University Press of Liverpool*, 176–192.

Risacher, F. F., Schneider, H., Drygiannaki, I., Conder, J., Pautler, B. G., & Jackson, A. W. (2023). A review of peeper passive sampling approaches to measure the availability of inorganics in sediment porewater. *Environmental Pollution*, *328*, 121581. https://doi.org/10.1016/j.envpol.2023.121581

Rütters, H., Sass, H., Cypionka, H., & Rullkötter, J. (2002). Phospholipid analysis as a tool to study complex microbial communities in marine sediments. *Journal of Microbiological Methods*, *48*(2), 149–160. https://doi.org/10.1016/S0167-7012(01)00319-0

Seeberg-Elverfeldt, J., Schlüter, M., Feseker, T., & Kölling, M. (2005). Rhizon sampling of porewaters near the sediment-water interface of aquatic systems. *Limnology and Oceanography: Methods*, *3*(8), 361–371. https://doi.org/10.4319/lom.2005.3.361

Sturt, H. F., Summons, R. E., Smith, K., Elvert, M., & Hinrichs, K. (2004). Intact polar membrane lipids in prokaryotes and sediments deciphered by high-performance liquid chromatography/electrospray ionization multistage mass spectrometry—New biomarkers for biogeochemistry and microbial ecology. *Rapid Communications in Mass Spectrometry*, *18*(6), 617–628. https://doi.org/10.1002/rcm.1378

White, D. C., Davis, W. M., Nickels, J. S., King, J. D., & Bobbie, R. J. (1979). Determination of the sedimentary microbial biomass by extractible lipid phosphate. *Oecologia*, *40*(1), 51–62. https://doi.org/10.1007/BF00388810

Wörmer, L., Lipp, J. S., & Hinrichs, K.-U. (2015). Comprehensive Analysis of Microbial Lipids in Environmental Samples Through HPLC-MS Protocols. In T. J. McGenity, K. N. Timmis, & B. Nogales (Eds.), *Hydrocarbon and Lipid Microbiology Protocols* (pp. 289–317). Springer Berlin Heidelberg. https://doi.org/10.1007/8623_2015_183

Zonneveld, K. A. F., Versteegh, G. J. M., Kasten, S., Eglinton, T. I., Emeis, K.-C., Huguet, C., Koch, B. P., De Lange, G. J., De Leeuw, J. W., Middelburg, J. J., Mollenhauer, G., Prahl, F. G., Rethemeyer, J., & Wakeham, S. G. (2010). Selective preservation of organic matter in marine environments; processes and impact on the sedimentary record. *Biogeosciences*, *7*(2), 483–511. https://doi.org/10.5194/bg-7-483-2010

Chapter 3: Reconstruction of the Porewater Geochemical Architecture at Seep 2A-1, Scotian Slope of Atlantic Canada

Abstract

The Scotian Slope off the coast of Eastern Canada extends for 1200 km along a passive plate margin with a proven history of active petroleum systems. In 2021, prospective seep site 2A-1 was verified by a remotely operated vehicle. During that dive, a six-push core transect was collected. In this study, a targeted downcore porewater ion survey was conducted to better constrain subsurface biogeochemical processes occurring within the deep marine environment. Using a combination of ion chromatography and photometry, nine ionic species were detected, quantified, and compared to other geochemical data. Principal component analysis revealed systematic links between porewater ion abundance based on the redox state, sample location, and sediment depth of the 2A-1 seep site samples. Several of these ions, such as sulfate and carbonate, were statistically correlated. Following stoichiometric relationships, the inversely correlated ion pair of sulfate and carbonate was hypothesized to enable detection of archaeal-driven anaerobic methanotrophy, the anaerobic oxidation of methane, and microbial sulfate reduction in what may mark an alternative method to resolve the sulfate-methane transition zone in biochemically stratified sediments where methane concentration depth profiles are absent. High ion diffusion fluxes were calculated within the seep with substantially lower fluxes observed within the ambient sediment outside the seep. Porewater ion heatmaps were further generated to visualize geochemical spatial changes in the seep environment. Based on these data, the two-dimensional porewater seep architecture at site 2A-1 was reconstructed for the seep transect. Distinct zones of denitrification, microbial sulfate reduction, the anaerobic oxidation of methane, and methanogenesis were mapped across the seep

transect. The physical placement of these zones indicates dramatic lateral and depth dependent changes within the seep that are driven by advective fluid flow from deeper within the basin.

3.1. Introduction

Within normal marine environments, seafloor sediments microbially mediate the biogeochemical cycling of carbon, nitrogen, and sulfur following predictable, energetically derived redox and diffusion limited gradients (Reeburgh, 2007). The redox zonation is driven by the availability of terminal electron acceptors and donors that become sequentially depleted with increasing sediment depth. The process begins in shallow, oxic sediments with organic matter oxidation coupled to O_2 reduction (Eq. 1), closely followed by the reduction of nitrate (NO_3^-) and nitrite (NO_2^-) in slightly deeper sub-oxic sediments. The resulting denitrification (Eq. 2) is responsible for up to 75% of the total marine-fixed nitrogen sink (Gruber, 2004) in a process, which converts bioavailable NO_3^- into nitrogen gas (N_2) that is unusable by heterotrophic marine organisms and ultimately released into the atmosphere. Once these anions are consumed, ferric iron (Fe^{3+}) and manganese oxides (Mn^{4+}) act as the next most favorable electron acceptors, producing Fe^{2+} and Mn^{2+} via microbially mediated reductive pathways. As these metal ions deplete and the sediments reach full anoxic conditions, microbial sulfate reduction (MSR; Eq. 3) is established, marking the most microbially active layer of subsurface biogeochemical cycling (Canfield & Des Marais, 1993; Jørgensen & Kasten, 2006). Below this boundary of energetic competitive exclusion, the metabolically less efficient methanogenic and acetoclastic fermenters step in to occupy the final stages of the biogeochemical cycling of carbon.

$$C_6H_{12}O_6 + 6O_2 \rightarrow 6CO_2 + 6H_2O \tag{1}$$

$$C_6H_{12}O_6 + 4NO_3^- + 4H^+ \rightarrow 6CO_2 + N_2 + 6H_2O \tag{2}$$

$$2(CH_2O) + SO_4{}^{2-} \rightarrow 2HCO_3^- + H_2S \tag{3}$$

Although these chemically stratified sediment profiles are ubiquitous within marine environments (Berner, 1980; Jørgensen & Kasten, 2006; Regnier et al., 2011; Cochran et al., 2022); the electron tower can nonetheless be disrupted by excessive redox compression arising from the ebullition of reduced fluids within cold seeps (Borowski et al., 1996; Regnier et al., 2011). Cold seeps are sites of low-pressure seepage of reduced fluids with similar temperatures as the surrounding ocean water along active and passive continental margins (Suess, 2020). The methane (CH_4) emitted from these vents is either produced from thermogenic processes from organic matter locked within deeply buried source rocks that is transformed by exposure to high temperatures and pressures over extended periods, or it is biogenically produced by methanogenesis via carbonate and acetate reduction or fermentation (Judd et al., 2002; Reeburgh, 2007). The carbon-based gas can be sequestered into methane hydrates and carbonate minerals (Joye et al., 2004). Where the influx of reduced fluids penetrates into unconsolidated deep ocean sediments and the overlying ocean water column, chemosynthetic microbial communities flourish and further help support diverse macrofaunal communities of bivalves, clams, tubeworms, crabs, shrimp, and fish (Levin, 2005).

More recently, the anaerobic oxidation of methane (AOM; Eq. 4) has been recognized as a fundamental global process mitigating the release of CH_4, a potent greenhouse gas, into the ocean water column (Knittel & Boetius, 2009). It is estimated that marine sediments contain 500–2,500 gigatons of methane carbon, acting as one of the largest reservoirs in the global carbon cycle (Milkov, 2004). However, only trace amounts of CH_4 (less than 2%) reach the overlying water column and atmosphere (Reeburgh, 2007). It is instead microbially oxidized across a narrow, anoxic sediment zone by AOM (Hinrichs et al., 1999; Boetius et al., 2000; Orphan, Hinrichs, et al., 2001) within the sulfate-methane transition zone (SMTZ), marking a dynamic environmental niche where both sulfate and methane exist in non-zero concentrations (R. O. Barnes & Goldberg, 1976; Reeburgh, 2007). The efficiency of AOM is dictated by substrate availability and the physical properties of the sediment (Knittel & Boetius, 2009).

$$CH_4 + SO_4{}^{2-} \rightarrow HCO_3^- + HS^- + H_2O \tag{4}$$

Material cycling within cold seeps provides insights into reaction processes and pathways of biogeochemical cycles and the timescales in which they operate (Orcutt et al., 2013). The rate of fluid seepage impacts the mixing of reducing and oxidizing fluids, changing the depth to which redox zonation forms (Borowski et al., 1996; Sommer et al., 2006). Furthermore, the precipitation of cold seep carbonates and gas hydrates decreases porosity and changes ion diffusion pathways (Solomon et al., 2008; Rooze et al., 2020). Calcium carbonate and gas hydrate formation are higher along preferential flow paths (Rooze et al., 2020).

Limited studies have targeted the Scotian Slope, leaving a gap in understanding these processes within a developing exploration basin. Previous studies utilized sedimentary porewater to constrain carbon cycling and calcium carbonate precipitation just past the shelf break (Mucci et al., 2000) and to study hydrocarbon-degrading microbial communities in deep piston cores (Adebayo et al., 2024). Nikita (2022) presents a juvenile porewater baseline survey of the Scotian Slope.

The Scotian Slope of Canada has a proven petroleum system that makes it highly prospective for passive margin cold seep formation. After a long exploration effort involving the analysis of available 3D seismic surveys and acquired geochemical data from various piston and gravity coring surveys, the existence of seep 2A-1 located at a water depth of ~2500 m on the Scotian Slope, ~400 km off the south-eastern coast of Nova Scotia (Fig. 3.1a), was verified by multi-beam sonar during an autonomous underwater vehicle cruise in 2022. Geophysical surveys revealed that site 2A-1 is located directly above a salt diapir, with a crustal fault extending from depth that would act as effective conduits for fluid migration (Fig. 3.1c). The seep was later visited using a remotely operated vehicle (ROV) in 2021 where several sediment push cores were collected from the seep site.

For this study, the concentrations of nine ions from sediment porewater were measured through ion chromatography or photometry. Concentration depth profiles were created to calculate concentration gradients and diffusion fluxes of targeted ions using Fick's First Law of Diffusion. The sampling methods used during collection allow for geochemical conditions to be monitored along an environmental gradient. Porewater concentration heatmaps were then constructed as a means of visualizing vertical and lateral redox changes. In the absence of a true CH_4 profile, this study suggests an alternative method for identifying the zone of AOM, and by consequence, the SMTZ, can be obtained. Collectively the assembled data allow the reconstruction of the geochemical seep architecture.

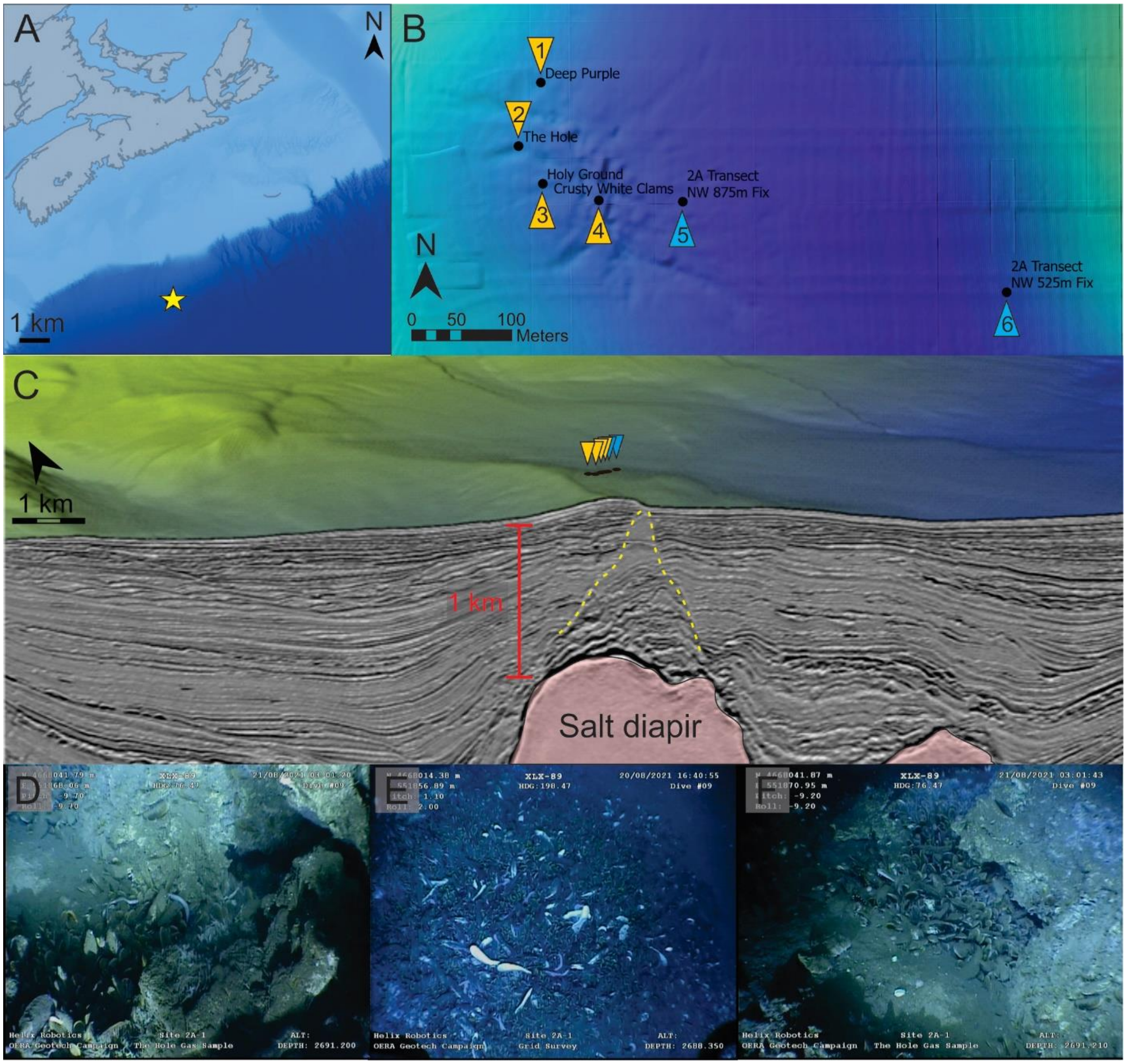

Figure 3.1: A) Location of site 2A-1 on the Scotian Slope, B) core sample locations of site 2A-1 transect, C) seafloor topography and seismic section near the push core transect (image provided courtesy of Nova Scotia Department of Natural Resources and Renewables), and D, E, F) ROV images from the 2A-1 seep showing seep supported shell beds and microbial mats. Yellow dotted line indicates crustal faulting.

3.2. Materials and Methods

3.2.1 Sample Collection

A transect of 6 push cores was collected from site 2A-1 on the Scotian Slope (Fig. 3.1b; Table 3.1) using a Triton XLX ROV operated by Helix Robotic Solutions Ltd. (Houston, Texas) on the 2021 Atlantic Condor expedition. Four cores were sourced from the seep structure at points of geochemical interest, namely in areas populated by bivalves, sessile organisms, and sites of active gas seepage (Fig. 3.1d-f). At the sampling site for Core 2, bubbles flowed from within the mussel covered sediment of the carbonate depression. Seep gas was trapped by a carbonate wall overhang producing a surface exposure gas hydrate (Bennett & Desiage, 2022). A final two cores were collected at increasing distances along a NW-SE transect to a maximum distance of 500 m.

Push cores reached a maximum depth of 40 cm below the seafloor (cmbsf). Core names were assigned based on the surficial characteristics of the coring location. Upon collection, the push cores were immediately subsampled at 2-cm thick depth intervals down to 20 cmbsf and at 4-cm thick slices until the bottom of the core was reached. The sediment slabs were immediately wrapped in pre-combusted aluminium foil and stored onboard the ship at -80 °C. All samples were kept frozen at that temperature until further processing at the Organic Geochemistry Laboratory located at Saint Mary's University (SMU).

Table 3.1. Push core sample summary.

Name	Core Number	Classification	Location (Lat., Long.)	Water Depth (m)
Deep Purple	1	Seep	42.163275, -62.372022	2686
The Hole	2	Seep	42.162698, -62.372356	2687
Holey Ground	3	Seep	42.162353, -62.302762	2688
Crusty White Clams	4	Seep	42.162198, -62.371378	2688
NW 875m	5	Transect	42.162180, -62.370351	2686
Midpoint	6	Transect	42.161334, -62.366394	2693

3.2.2 Sedimentary Carbon Analysis

Total organic carbon (TOC) and particulate inorganic carbon (PIC) were measured from the same sediment sample. Approximately ~2.5 g of frozen sediment was dried at 35 °C for a minimum of 12 hrs. The difference in weight between the frozen and dried samples was recorded as a secondary measurement of sediment porosity. Once dry, sediment samples were treated with 5 ml 6N hydrochloric acid (HCl) and left to decarbonate for 24 hrs. Acid treated samples were neutralized by repetitive washing with de-ionized water until they reached a pH of 7. Neutral samples were again dried at 35 °C for 12 hrs before being stored at 4 °C until analysis. Particulate inorganic carbon (PIC) was recorded as the difference in weight between the original dry sediment and the dried neutralized sediment.

Total organic carbon measurements were collected using a Perkin-Elmer 2400 Series II CHNS/O Elemental Analyzer (EA) programmed for CHN analysis at the Centre for Environmental Remediation (CEAR) at SMU. The EA was calibrated using Cyclohexanone 2,4-dinitrophenylhydrazone (Organic Analytical Standard (OAS)), Elemental Analysis Lot No. BN330953) and cysteine (OAS, Perkin Elmer, Lot No. 090M1244V) was used as the conditioner. A matrix-matched, silty soil standard (Organic Analytic Standard, Elemental Microanalysis Ltd. Certificate No. 133507) was used to ensure an accurate reading of the sediment samples. For the analysis, 10 mg of neutral sediment was weighed into a foil tin and injected into the EA using Ar gas as the carrier.

3.2.3 Sedimentary Porewater

Approximately 40 g of frozen sediment was placed into a plastic centrifugation tube and left for up to 2 hrs to defrost. The sediment was then centrifugated for 10 min at 2500 rpm. The supernatant porewater was pipetted out of the tube and passed through a 45-µm filter to remove residual suspended sediment particles. The volume of recovered porewater was recorded as the primary measure of sediment porosity.

3.2.3.1 Porewater Ion Analysis

Due to the limited sediment supply, alternating ~4 cm sediment intervals were assigned for anion and cation analyses. Anion measurements were obtained by ion chromatography. An additional mix of cation and anion concentrations were collected by photometry. The exception to this division was the 0-2 cm surface sediment interval, which was analysed with both methods.

3.2.3.2 Ion Chromatography

Ion chromatography was used to measure fluoride (F^-), NO_2^-, DIC, SO_4^{2-}, and NO_3^- concentrations. Filtered porewater was diluted in HPLC grade water [1:5] to a total injection volume of 600 µl into a Thermo Scientific Dionex Aquion Chromatography Conductivity System equipped with an anion-exchange column and a DS6 Heated Conductivity Cell fitted to an AERS_4mm suppressor pump and a Dionex AXP auxiliary pump operating at a flow rate of 1.00 $mlmin^{-1}$. The system is further equipped with two in-line guard cartridges: Thermo Scientific 9×24-mm Dionex InGuard Ag and Thermo Scientific Dionex InGuard Sodium (Na^+) prep cartridges. The mobile phase was 25 mM NaOH in HPLC grade water. Sedimentary porewater ion concentrations were calculated based on an external calibration curve using an anion standard (Thermo Scientific Dionex Seven Anion Standard II)/carbonate stock (2000 $mg{\cdot}L^{-1}$ Na_2CO_3)/HPLC water [2:1:1, v/v/v] with standard mixture dilutions of 0.5, 1, 2, 5, 10, 20, and 50 ppm.

3.2.3.3 Photometry

A Hanna Instruments HI-83300 Multiparameter Photometer was used to measure porewater ammonium (NH_4^+), Fe^{2+}, Mn^{2+}, and phosphate (PO_4^{3-}) concentrations. Prior to analysis, the photometer was calibrated through a series of absorbance measurements (420, 466, 525, 575, and 610 nm) to reach within an acceptable range of 0.02 abs. A 0.5–4 ml aliquot of filtered unreacted porewater was allocated to each ion. For NH_4^+, 1 ml of porewater was diluted in 9 ml of Hanna Instruments Ammonia Reagent A. Iron, Mn^{2+}, and PO_4^{3-} used varying amounts of porewater diluted in milli-Q water to reach a total volume of 10 ml. Following the baseline read of the unreacted sample, the appropriate indicator solutions associated with NH_4^+, Fe^{2+}, Mn^{2+}, and PO_4^{3-} were dissolved in the porewater sample. Concentration readings were re-calculated to account for individual dilution factors. The concentrations of Fe^{2+}, Mn^{2+}, and PO_4^{3-} were only collected where porewater volume recoveries were large enough to allow for an accurate measurement.

3.2.4 Statistical Analysis

Principal component analysis (PCA) was carried out using the "factomineR" package in RStudio (Version 4.3.2). Only ions that were consistently available across the data set were selected, thereby limiting the analysis to NO_2^-, NO_3^-, F^-, SO_4^{2-}, DIC, and NH_4^+. Prior to analysis, ion concentration measurements were standardized to ensure comparability. Using the "psych" package, the Kaiser-Meyeer-Olkin (KMO) test for sampling adequacy and Barlett's test of sphericity were initially used to confirm the data set's suitability for PCA. A KMO score higher than 0.6 and a p-value of less than 0.05 for the Barlett's test indicate the data is suitable for PCA. Results were visualized using the "factoextra" package. A scree plot of the data was used to determine the number of principal components (PCs) to retain and explain the cumulative variance.

3.2.5 Diffusion Flux

Diagenetic processes and material fluxes are recorded in porewater concentration profiles. Material fluxes are represented by changes in ion concentrations (Schulz, 2000). The sediment porewater diffusion flux was calculated using Fick's first law of diffusion under assumed steady state conditions (Eq. 5), where the diffusion flux (J_{sed}) is calculated from the sediments porosity (φ), diffusion coefficient (D_{sed}), and the concentration gradient ($\partial C/\partial x$). Concentration gradients can indicate upward and downward material fluxes. For ions with multiple gradients, the up-flux and the down-flux were averaged for the core. The diffusion coefficient for each ion was calculated from sediment tortuosity and the ions diffusion coefficient in free solutions of seawater (D_{sw}) (Table 3.2; Eq 6). Tortuosity (θ) is the mean ratio between the real length of the diffusion flux pathway and the straight-line distance and can be estimated from the sediment's porosity (Eq 7).

$$J_{sed} = -\phi \cdot D_{sed} \cdot \frac{\partial C}{\partial x} \tag{5}$$

$$D_{sed} = \frac{D^{sw}}{\theta^2} \tag{6}$$

$$\theta^2 = 1 - \ln(\phi^2) \tag{7}$$

Diagenetic processes are time dependent. The sampling methods used in this study do not allow for this variable to be accurately calculated, sediment depth is instead employed as a means of modeling processes over time, this approach is also used by Schulz (2000). Results were further compared to approximal CH_4 headspace analysis taken from adjected cores at sampling locations measured by Martin Fowler of Applied Petroleum Technologies (APT) (open-source file) and Chowdhury et al. (2024).

Table 3.2. Diffusion constants for free ions in seawater from Schulz (2000) and sources herein.

Ion	D_{SW} ($m^2 \cdot s^{-1}$ at 5 °C)
NO_2^-	1.13×10^{-9}
NO_3^-	1.08×10^{-9}
SO_4^{2-}	5.72×10^{-10}
DIC	6.09×10^{-10}
NH_4^+	1.10×10^{-9}

3.3. Results

3.3.1 Sediment Characteristics

Porewater geochemistry is dependent on sedimentological properties such as porosity and permeability of the locality. All push cores contained highly permeable unconsolidated sediments of sand to silt-sized particles. Sediment porosity changes with gravimetric compactions and exponentially decreased with depth for all the push cores in the transect. The average porosity at 0–2 cmbsf was 0.29 $w \cdot v^{-1}$ decreasing to an 0.10 $ml \cdot mg^{-1}$ within the deepest measured core intervals (Table 3.3).

Total organic carbon was measured sporadically throughout the data set (Table 3.3). A complete suite of measurements is available for cores 1–3, 4 measurements are available from cores 4 and 6, but no TOC measurements have been recorded in core 5. For the cores collected within the seep, a total of 36 TOC measurements were made. Of these, the TOC ranged from 0.35 to 1.10 wt.% (avg. 0.51 wt.%) and displayed decreasing or constant depth trends. The TOC from core 6 was high (ranging from 0.77 to 0.97 wt.%; avg. 0.88 wt.%) compared to the seep average and displayed an increasing depth trend. Concentrations of mineralized carbon do not appear to be influenced by sediment depth or their proximity to the seep centre.

3.3.2 Porewater Ion Survey

Measured ion concentrations ranged from 30.39 $mmol \cdot L^{-1}$ to 0.01 $mmol \cdot L^{-1}$ (Table 3.3; Fig. 3.2). For all observed ions, SO_4^{2-} and DIC reached the highest concentrations of 30.39 $mmol \cdot L^{-1}$ and 18.53 $mmol \cdot L^{-1}$, respectively. Based on porosity and sediment availability, not all ions measured by photometry were able to be measured consistently downcore. Priority was therefore given to NH_4^+ followed by Fe^{2+}, with Mn^{2+}, and PO_4^{3-} being the lowest priority and only measured in the most porous sediments. Core 2 was extremely non-porous and limited ion measurements to IC measured anions and NH_4^+.

Concentrations of NO_3^- were, on average, double those of NO_2^-. Concentration and downcore variability of both NO_3^- and NO_2^- decreased with proximity from the seep. Following the anticipated redox gradient, overall concentrations of NO_3^- and NO_2^- decreased with depth with some downcore variation. From the 0–2 cmbsf interval NO_3^- decreased from an average 0.19 to 0.13 $mmol \cdot L^{-1}$ to the core bottom. Nitrite exhibited a less pronounced trend, decreasing from an average 0.08 to 0.06 $mmol \cdot L^{-1}$.

Outside of distinct intervals in cores 1 and 3, the concentration of NH_4^+ was low across the sample set. Although, it initially appears that NH_4^+ increases with depth, this trend is masked by downcore variability and overall low cation concentration. Concentrations of Fe^{2+} and Mn^{2+} were also notably low across all samples. Overall, these ions do not appear to exhibit systematic downcore trends nor do they appear to be influenced by their proximity to the seep.

The most concentrated porewater ions are SO_4^{2-} and DIC^-, which also exhibit the largest downcore gradients. Dissolved inorganic carbon is composed of 3 carbon species: HCO3- and CO32-, which are both measure by the IC system, and CO2. At typical seawater pH conditions, >99 % of DIC is composed of HCO- and CO32- (Zeebe, R.E., & Wolf-Gladrow, D.A., 2001). In the 0–2 cmbsf interval of the transect, SO_4^{2-} has an average concentration of 26.10 $mmol \cdot L^{-1}$. Within the seep cores 1 to 4, SO_4^{2-} concentrations exponentially decrease to ~7.46 $mmol \cdot L^{-1}$ at the core bottom. The ambient sediment cores, cores 5 and 6, do not experience this same depletion with depth, and instead core bottom concentrations measure ~28.75 $mmol \cdot L^{-1}$, remaining steady downcore. The opposite trend is observed in measurements of DIC. The average concentration of DIC in the 0–2 cmbsf interval is 1.69 $mmol \cdot L^{-1}$. Within cores 1–4, this value increases exponentially to 10.15 mmol·L^{-1} by the core bottom, but steadily decreases further to 0.58 mmol·L^{-1} with depth in cores 5 and 6.

The downcore profiles of F$^-$ varied with sampling location along the transect. For cores 1 to 4, concentrations decreased with depth. Cores 5 and 6 exhibit a steady increase with depth. Concentrations of F$^-$ range from 0.71 to 0.07 mmol·L^{-1} (avg. = 0.16 mmol·L^{-1}). Phosphate does not have a downcore or spatially controlled trend. Concentrations range from only 0.10 to 0.00 mmol·L^{-1} (avg. = 0.02 mmol·L^{-1}). These ambiguous results may be the product of limited porewater availability and dilution with de-ionized water.

Table 3.3. Porewater ion and TOC, PIC concentration summary.

Core Number	Sediment Interval (cmbsf)	Instrument	Porosity (ml·mg^{-1})	TOC (wt.%)	$\delta^{13}C_{TOC}$ (‰)	PIC (wt.%)	Ions (mmol · L^{-1})								
							F^-	NO_2^-	DIC	SO_4^{2-}	NO_3^-	NH_4^+	Fe^{2+}	Mn^{2+}	PO_4^{3-}
1	0-2	IC + P		0.35		0.63	0.24	0.07	2.50	23.12	0.17	0.34	0.00	U	U
	2-4	P	0.29	0.49		0.63	-	-	-	-	-	0.94	0.01	0.08	0.04
	4-6	IC		0.49		0.60	0.33	0.07	11.97	6.81	0.12	-	-	-	-
	6-8	P	0.24	0.51		0.66	-	-	-	-	-	2.88	0.04	0.20	0.08
	8-10	IC		0.37		0.55	0.13	0.06	14.83	2.09	0.11	-	-	-	-
	10-12	P	0.2	0.45		0.58	-	-	-	-	-	1.13	0.02	0.06	0.05
	12-14	IC	0.19	0.39		0.58	0.11	0.05	15.58	1.59	0.12	-	-	-	-
	14-16	P	0.18	0.48		0.56	-	-	-	-	-	2.68	0.02	0.11	0.07
	16-18	IC		0.48		0.62	0.15	0.06	13.34	1.13	0.12	-	-	-	-
	18-20	P	0.17	0.44		0.57	-	-	-	-	-	2.45	0.01	0.18	0.07
	20-24	IC		0.38		0.67	0.11	0.05	15.78	1.15	0.10	-	-	-	-
	24-28	P	0.17	0.45		0.63	-	-	-	-	-	2.16	0.01	0.11	0.07
2	0-2	IC + P	0.42	1.10	-40.06	0.40	0.17	0.07	0.06	28.72	0.17	0.25	0.00	0.07	0.07
	2-4	P	0.26	0.85		0.46	-	-	-	-	-	0.29	0.02	0.07	0.02
	4-6	IC		0.73		0.39	0.18	0.09	0.82	27.56	0.18	-	-	-	-
	6-8	P	0.09	0.63	-38.80	0.43	-	-	-	-	-	0.09	0.00	U	U
	8-10	IC		0.63		0.33	0.21	0.09	4.54	15.61	0.14	-	-	-	-
	10-12	P	0.05	0.63		0.30	-	-	-	-	-	0.44	U	U	U
	12-14	IC		0.38	-28.29	0.40	0.12	0.06	10.13	4.84	0.13	-	-	-	-
	14-16	P	0.04	0.43		0.29	-	-	-	-	-	0.67	U	U	U
	16-18	IC		0.40		0.29	0.09	0.06	11.72	1.29	0.11	-	-	-	-
	18-20	P	0.04	0.42	26.22	0.29	-	-	-	-	-	0.62	U	U	U
3	0-2	IC + P	0.31	0.52	-35.20	0.29	0.71	0.08	2.56	24.59	0.19	0.68	0.00	0.02	0.01
	2-4	P	0.42	0.58		0.36	-	-	-	-	-	0.67	0.01	0.02	0.02
	4-6	IC+P		0.50		0.31	0.32	0.08	12.66	3.48	0.14	5.64	0.01	U	0.10
	6-8			0.51		0.36	-	-	-	-	-	-	-	-	-
	8-10	IC		0.47		0.36	0.25	0.09	8.30	4.56	0.17	-	-	-	-

	10-12	IC+P	0.2	0.44	-41.92	0.36	0.18	0.07	13.18	0.87	0.11	0.39	0.01	0.10	0.00
	12-14	P	0.13	0.38		0.33	-	-	-	-	-	7.14	0.01	0.01	U
	14-16	IC		0.47		0.28	0.08	0.07	13.79	1.00	0.10	-	-	-	-
	16-18	P	0.12	0.47		0.34	-	-	-	-	-	7.14	0.01	U	0.10
	18-20	IC		0.47		0.30	0.18	0.06	10.01	4.64	0.14	-	-	-	-
	20-24	P	0.15		-39.25	0.36	-	-	-	-	-	0.43	0.01	0.07	0.01
4	0-2	IC + P	0.28	0.72	-31.31	0.29	0.15	0.09	2.64	23.75	0.16	0.18	0.00	0.06	0.01
	2-4	P	0.23			0.21	-	-	-	-	-	0.55	0.03	0.13	0.01
	4-6	IC				0.23	0.13	0.07	18.53	22.47	0.15	-	-	-	-
	6-8	P	0.18			0.20	-	-	-	-	-	0.35	0.03	0.07	0.00
	8-10	IC		0.54	-30.13	0.23	0.12	0.06	8.98	11.70	0.14	-	-	-	-
	10-12	P	0.15			0.23	-	-	-	-	-	0.44	0.01	0.10	0.02
	12-14	IC				0.19	0.51	0.07	4.58	20.16	0.14	-	-	-	-
	14-16	P	0.1			0.21	-	-	-	-	-	0.18	0.01	0.07	0.01
	16-18	IC				0.20	0.09	0.06	2.56	23.77	0.15	-	-	-	-
	18-20	P	0.06	0.44	-27.19	0.22	-	-	-	-	-	0.05	0.04	U	0.00
	20-24	IC				0.23	0.11	0.07	2.07	23.71	0.14	-	-	-	-
	24-28	P	0.03			0.20	-	-	-	-	-	0.11	0.01	0.20	U
	28-32	IC				0.18	0.10	0.07	3.11	22.77	0.15	-	-	-	-
	32-38	P	0.03	0.46	-26.12	0.22	-	-	-	-	-	0.14	0.00	U	U
5	0-2	IC				0.50	0.07	0.08	0.22	28.63	0.15	-	-	-	-
	2-4	P	0.24			0.47	-	-	-	-	-	0.00	0.00	0.06	0.00
	4-6	IC				0.47	0.09	0.05	0.45	28.56	0.14	-	-	-	-
	6-8	P	0.13			0.46	-	-	-	-	-	0.09	0.00	0.07	0.01
	8-10	IC				0.45	0.10	0.05	1.00	29.89	0.14	-	-	-	-
	10-12	P	0.11			0.49	-	-	-	-	-	0.04	0.00	0.08	0.00
	12-14	IC				0.43	0.09	0.05	1.80	21.20	0.12	-	-	-	-
	14-16	P	0.1			0.42	-	-	-	-	-	0.16	0.01	0.07	0.00
	16-18	IC				0.39	0.09	0.05	0.66	30.39	0.14	-	-	-	-
	18-20	P	0.1			0.28	-	-	-	-	-	0.11	0.00	0.11	0.00
	20-24	IC				0.31	0.10	0.05	1.06	30.25	0.14	-	-	-	-

	24-28	P	0.1			0.22	-	-	-	-	-	0.04	0.01	0.05	0.00
	28-32	IC				0.28	0.09	0.05	0.66	29.63	0.14	-	-	-	-
	32-36	P	0.08			0.27	-	-	-	-	-	0.14	0.00	0.05	0.00
	36-40	IC				0.23	0.10	0.05	0.60	29.78	0.13	-	-	-	-
6	0-2	IC + P	0.26	0.85	-21.83	0.46	0.07	0.07	2.13	27.81	0.15	0.01	0.00	0.07	0.00
	2-4	P	0.24			0.46	-	-	-	-	-	0.08	0.00	0.05	0.00
	4-6	IC				0.50	0.07	0.05	0.88	29.62	0.15	-	-	-	-
	6-8	P	0.16			0.45	-	-	-	-	-	0.51	0.00	0.03	0.00
	8-10	IC		0.77	-21.63	0.46	0.08	0.05	0.55	28.18	0.13	-	-	-	-
	10-12	P	0.15			0.45	-	-	-	-	-	0.35	0.00	0.05	0.01
	12-14	IC				0.44	0.08	0.05	0.61	28.33	0.12	-	-	-	-
	14-16	P	0.13			0.41	-	-	-	-	-	0.11	0.01	0.07	0.01
	16-18	IC				0.29	0.09	0.05	1.11	28.73	0.15	-	-	-	-
	18-20	P	0.12	0.96	-21.55	0.30	-	-	-	-	-	0.16	0.00	0.04	0.01
	20-24	IC				0.31	0.08	0.05	1.11	29.19	0.13	-	-	-	-
	24-28	P	0.16			0.28	-	-	-	-	-	0.12	0.00	U	0.01
	28-32	IC				0.40	0.09	0.05	0.55	27.72	0.12	-	-	-	-
	32-36	P	0.16	0.97	-22.56	0.30	-	-	-	-	-	0.14	0.00	0.05	0.01

IC = ion chromatography

P = photometer

U = measurement unavailable from lack of porewater

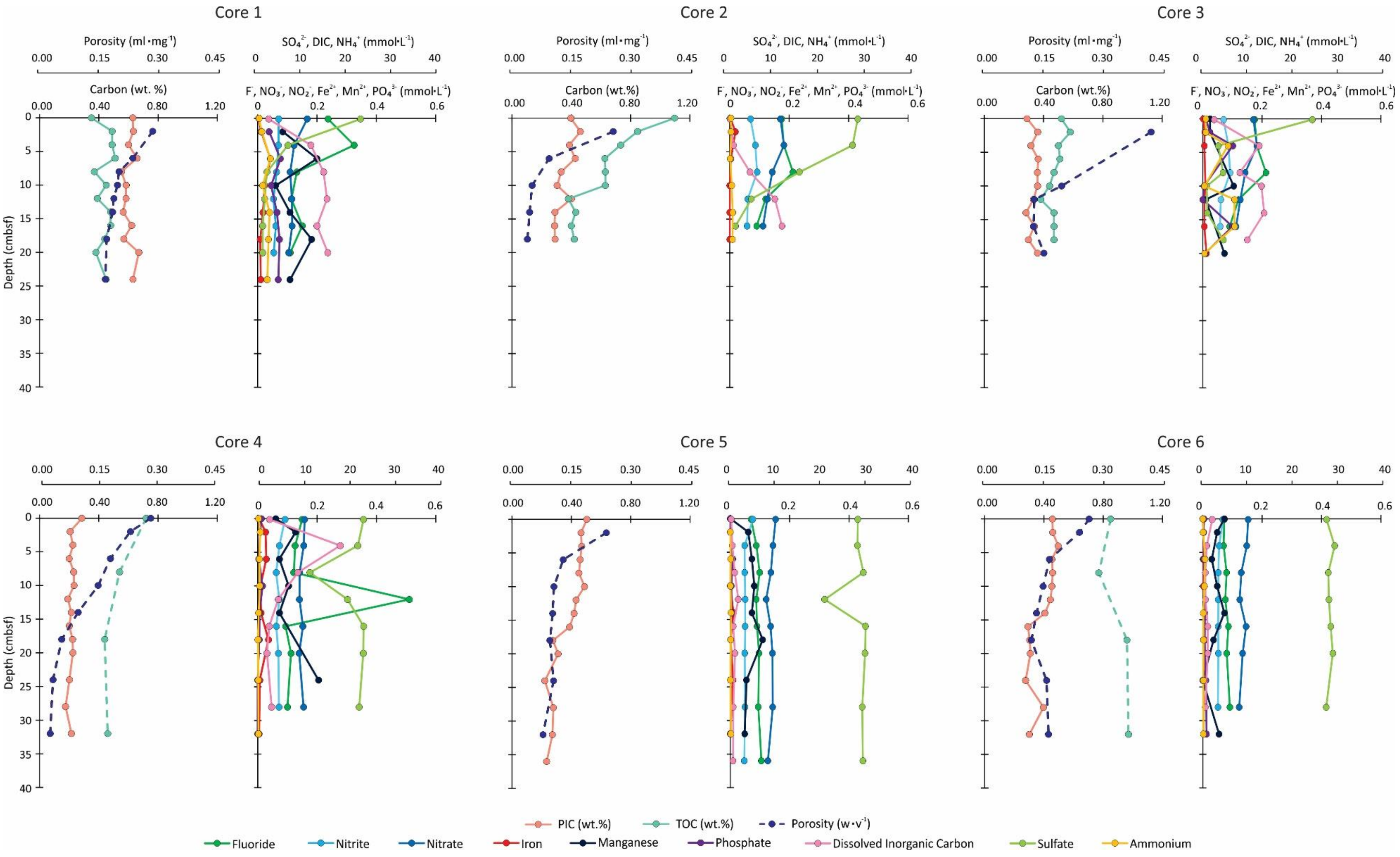

Figure 3.2: Sedimentary carbon and porewater ion survey. Core are organized by their location along the transect. Dashed lines for sedimentary carbon characteristics indicate that sampling was not continuous down core. Porewater was measured on alternating intervals but is treated as a continuous measurement from each method of instrumentation.

3.4. Discussion

3.4.1 Principal Component Analysis

Principal component analysis was employed to identify controls on ion variability by simplifying the complexity of the multivariate concentration data through dimensionality reduction. Prior to analysis, the Kaiser-Meyer-Olkin Test (KMO = 0.66) and Bartlett's Test of sphericity ($p < 0.05$), were completed to ensure the data was suitable for PCA. A scree plot revealed that the first two PCs explain 79% of the variance in the data set (Appendix A1). A secondary analysis of each ion's squared cosine value and contribution value was used to explain their involvement in the creation of each PC (Appendix A1).

The first and second principal components (PC 1 and PC 2), accounts for 46.6%, 32.4% of variation, respectively. Figure 3.3 provides the merged factor loadings and scores plots for the 2A-1 transect sample set. For PC 1, positive factor loadings were obtained for DIC and NH_4^+ and negative loadings were calculated for SO_4^{2-} and to a lesser degree, NO_3^- (Fig. 3.3). Near zero loadings were produced for NO_2^- and F^- (Fig. 3.3), indicating the variability of these three porewater ions is largely not affected by PC 1. Based on the distribution of samples in the embedded scores plot, PC 1 likely indicates first-order redox changes in the depositional environment with decreasing down core ion concentrations yielding negative factor loadings and those having positive gradients generating positive loadings.

The second principal component (PC 2) accounts for 32.4% of the variation in the data set and shows positive loadings for NO_2^-, NO_3^-, and F^- with near zero loadings for SO_4^{2-}, DIC, and NH_4^+. PC 2 is likely influenced by preferentially elevated abundances of NO_2^-, NO_3^-, and F^- in the shallowest sediment horizons. The absolute mean concentrations of these ions are significantly lower than SO_4^{2-}, DIC, and NH_4^+ and do not experience the same gradient changes or variability as observed within the more concentrated ions.

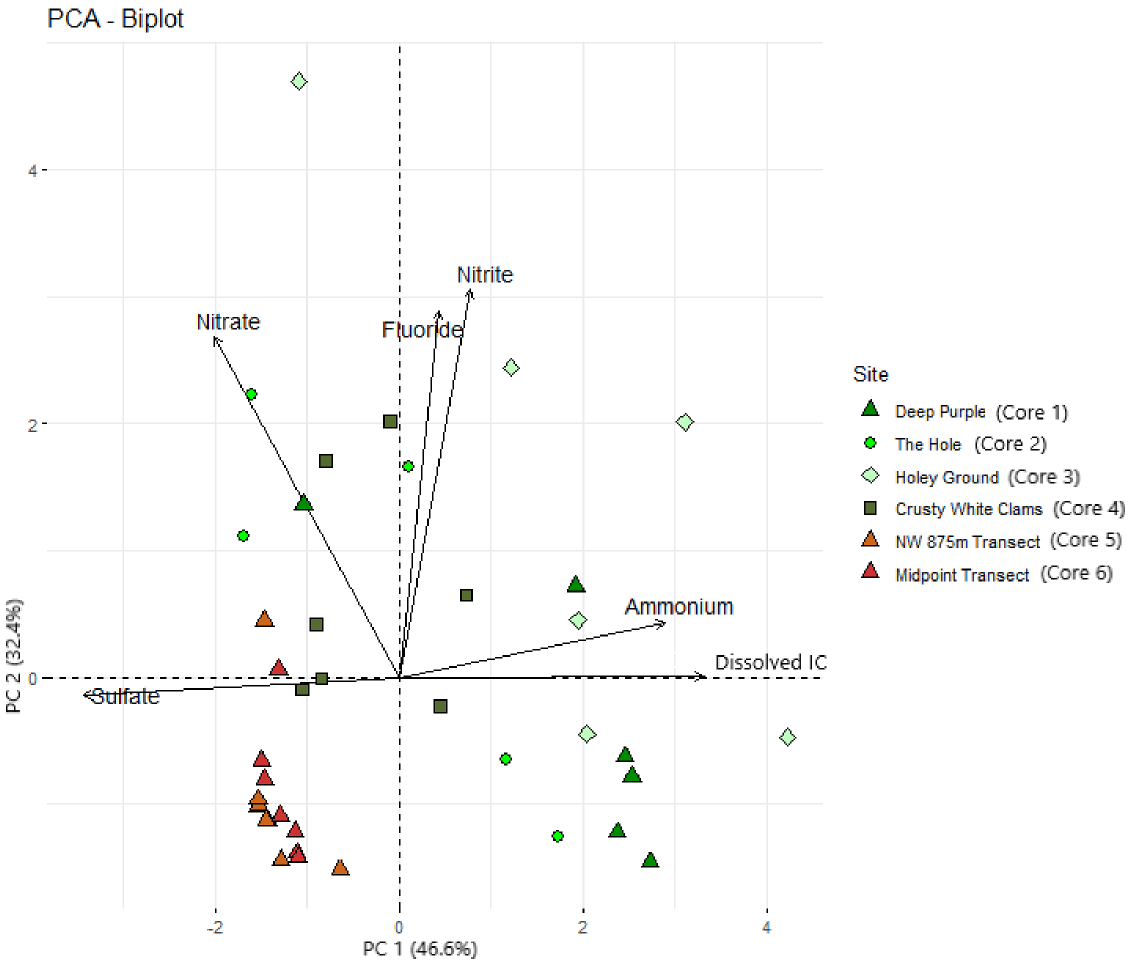

Figure 3.3: Biplot of principal components analysis factor loadings and embedded scores plot of seep site 2A-1 core sediment porewater ions.

The scores plot of Figure 3.3 shows cores collected within the seep are easily distinguished from ambient coring sites. Cores 5 and 6 have negative loadings on PC 1 and 2, plotting near SO_4^{2-}, which is the most concentrated ion within the ambient sediments. Seep-sourced push core samples are broadly distributed through PCs 1 and 2, with deeper core samples experiencing positive loadings on PC1, reflecting their higher DIC content (Appendix Figure A1.3). The lack of pronounced ion concentration gradients in the ambient cores likely distinguishes the distribution of these sediments on the biplot from cores 1–4 that have pronounced gradients. Interestingly, core 4, which does not have notable loadings on either component, has a mixed geochemical environment (Fig. 3.3).

3.4.2 Porewater Ion Coupling

Following the PCA results, partial least square regression models were applied to all prospective correlated ion pairs (Figs 3.4 and 3.5). From the cross-plots, NH_4^+ was confirmed to be positively correlated with DIC and negatively correlated to SO_4^{2-} for most seep-sourced cores (Fig. 3.4). Sulfate porewater ions were also observed to be positively correlated to DIC for most seep sourced cores (Fig. 3.4).

In keeping with causal mechanisms behind statistical patterns, the slope of the regression line is postulated to describe the stoichiometric relationship between ions participating in a specific microbial metabolism (Eqs. 2, 3, 4). However, for those cores that have high coefficients of determination, care must be given as to what guides their statistical relationship as direct metabolic reactions linking SO_4^{2-} or DIC with NH_4^+ are not well established. Additionally, statistical relationships with NH_4^+ were not resolvable in the downcore profiles due to low NH_4^+ concentrations. For this reason, metabolic processes associated with NH_4^+ were not further explored. The relationship between SO_4^{2-} and DIC is the focus of the following section, as both anions are directly liked in MSR and AOM.

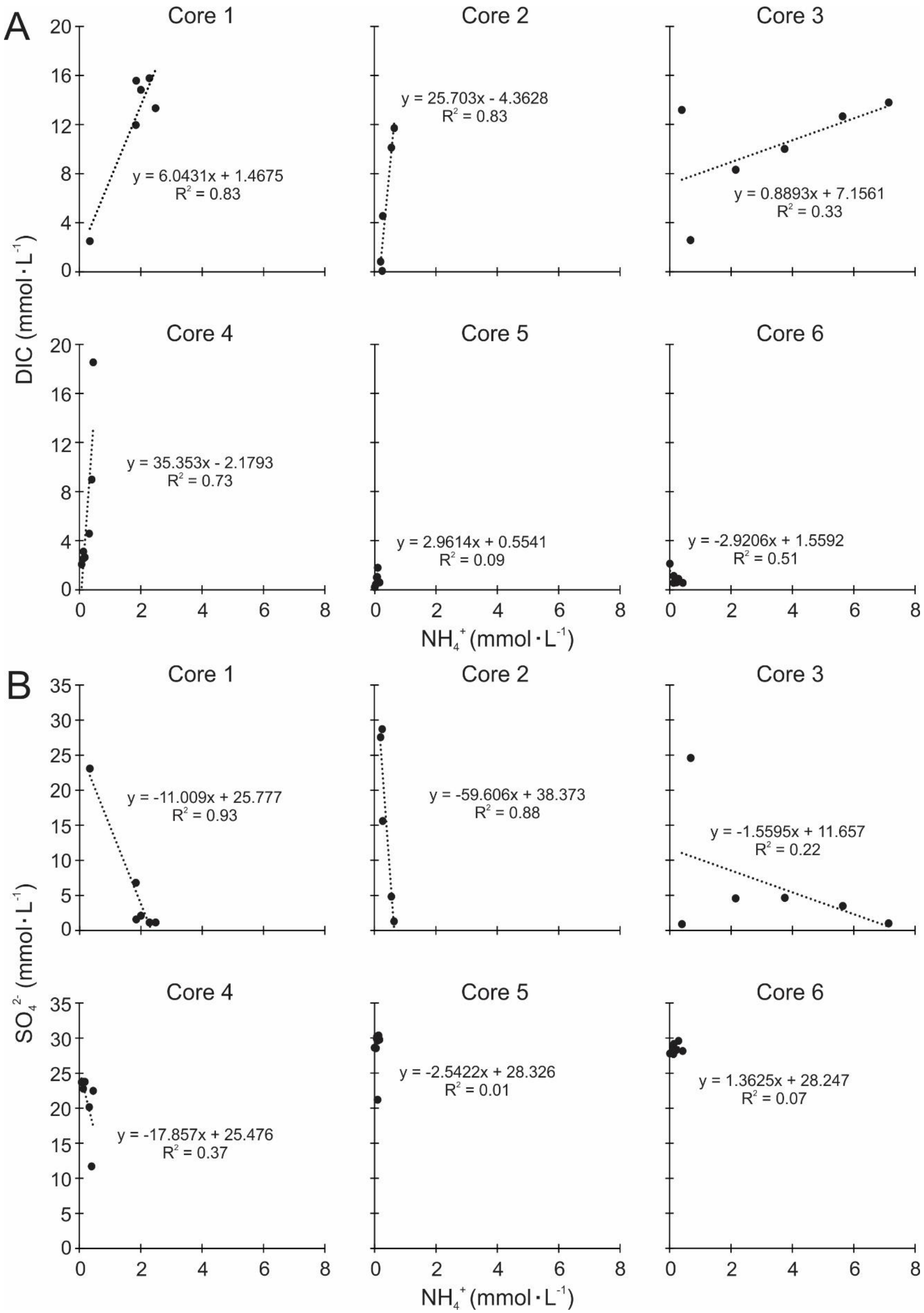

Figure 3.4: Cross-plots of A) NH_4^+ versus DIC and B) SO_4^{2-} versus NH_4^+ ion concentrations.

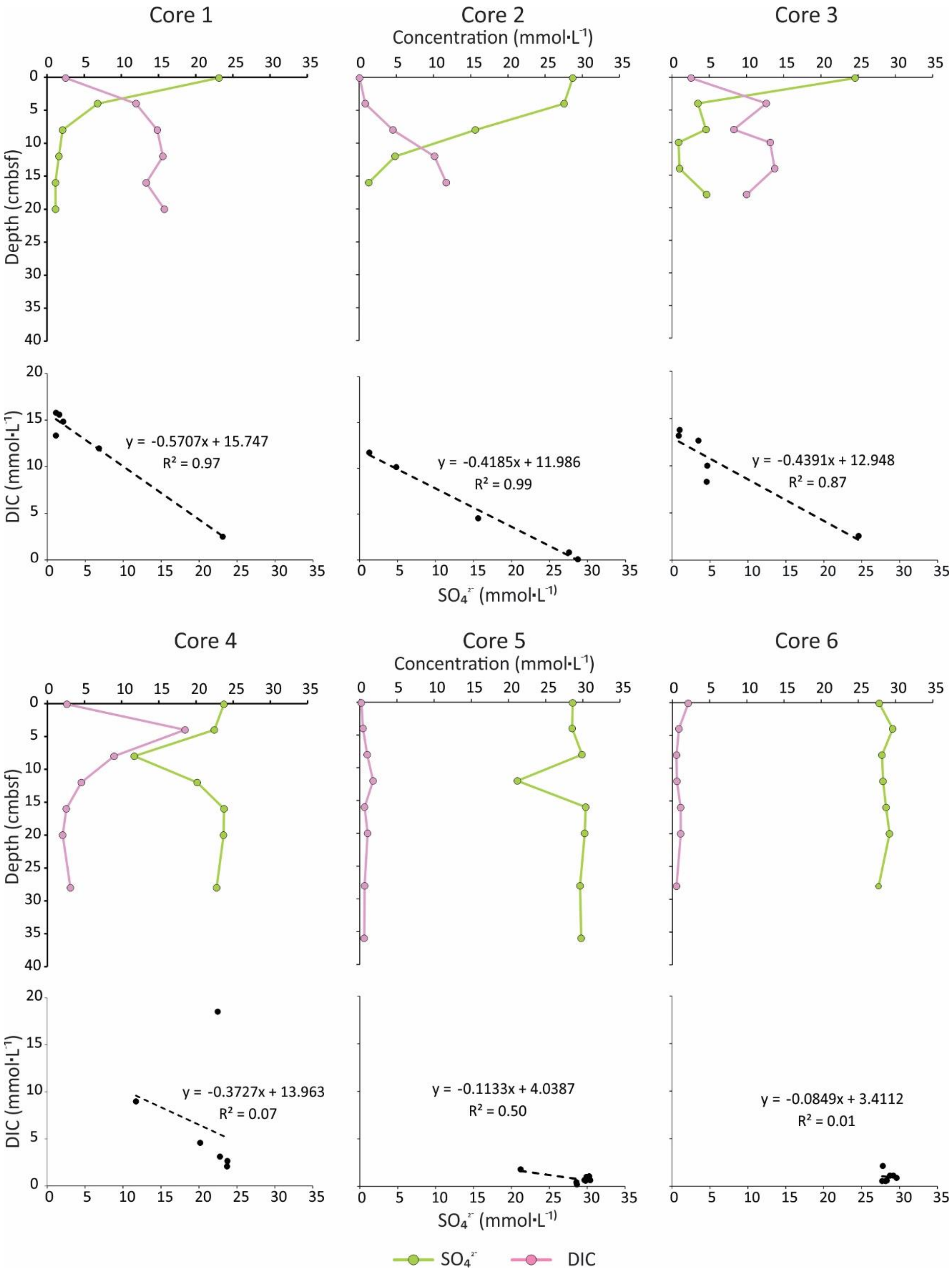

Figure 3.5: Downcore concentration plots of SO_4^{2-} and DIC accompanied below by a cross-plots of the ion pair. The slope of the PLS regression line corresponds to the reaction rate of the ion pair.

3.4.3 Sulfate-Carbonate Transitions

Within cold seep environments, SO_4^{2-} is rapidly depleted from the effects of both decomposing organic matter as well as by compression of the ocean floor shallow sediment oxic layer by the underlying CH_4 flux (Borowski et al., 1996). Porewater SO_4^{2-} and DIC is further intimately connected in marine sediments through MSR (Eq 3), AOM (Eq 4), the remineralization (oxidation) of organic matter, and carbonate formation. An inverse correlation between these two ions is notable in the seep downcore profiles and by the partial least squares regression model (Fig. 3.5). In contrast, within the transect cores, SO_4^{2-} concentrations remain unchanged with depth, as the oxic layers of sediment extend to deeper depths with little to no CH_4 influence (Appendix Fig. A1.4). Interestingly, a high correlation ($R^2 = 0.78$) is further obtained when the analysis is extended to the composite set of all site 2A-1 transect samples in the property-property plot (Fig. 3.6), suggesting a distinct linear dependence for the composite geochemical changes across the ambient to cold seep environments.

Within Figure 3.6, metabolic zones were plotted based on the stoichiometric relationships of MSR and AOM with regards to the coupled pairing of SO_4^{2-} and DIC. These zones are further controlled by changing alkalinity within the sedimentary environment. As carbonate is the dominant component of dissolved inorganic carbon (DIC), changes to porewater alkalinity are fundamentally controlled by carbonate precipitation and the oxidation of organic matter (Burdige & Komada, 2011; Liu et al., 2020). For Figure 3.6 normal marine conditions are assigned to the modern average SO_4^{2-} concentration of seawater (28 $mmol \cdot L^{-1}$) (Vairavamurthy et al., 1995; Canfield, 2004). The boundary distinguishing normal marine conditions from the onset of MSR is determined by the 2:1 ratio of SO_4^{2-} to HCO_3^- (Eq 2). The rate of HCO_3^- production from SO_4^{2-} consumption is further controlled by the stoichiometric balanced of the AOM reaction (Eq 1), where the ion pair exists in a 1:1 ratio. The 1:1 line of Figure 3.6 therefore dictates the theoretical start of AOM conditions, dubbed the sulfate dissolved inorganic carbon transition zone (SDICTZ), with porewater ion pairs falling to the left of this line marking a mix of both SRB and anaerobic methane-oxidizing archaea (AMNE) activities that transition to increasing AOM predominance when SO_4^{2-} exists in near zero (<2 $mmol\cdot L^{-1}$) concentrations (here inferred to be the SMTZ with a concomitant variable range of alkalinity conditions being possible).

For seep site 2A-1, sediment samples largely fall into normal marine, and the mixed sulfate reduction and AMNE zone, with only the shallowest seep samples plotting in the exclusively sulfate reduction zone (Fig. 3.6). Consistent with these zones, shallow sediments and those samples sourced from ambient sites fall within the zones of normal marine conditions. Samples with high DIC, and consequently low values of SO_4^{2-} porewaters concentrations are heavily CH_4 impacted sediments located at deeper depths within the seep. Background samples of porewater measurements from piston, box, and gravity cores collected from the 2015, 2016, 2018, and 2021 expeditions (with some samples extending down to 800 cmbsf) from the Scotian Slope were further added to assess the reproducibility of the 2A-1 seep site trend. These samples are expected to reach sediment depths where AOM is active (Regnier et al., 2011). These samples also follow depth dependent trends with deeper sourced samples falling into anoxic metabolism zones.

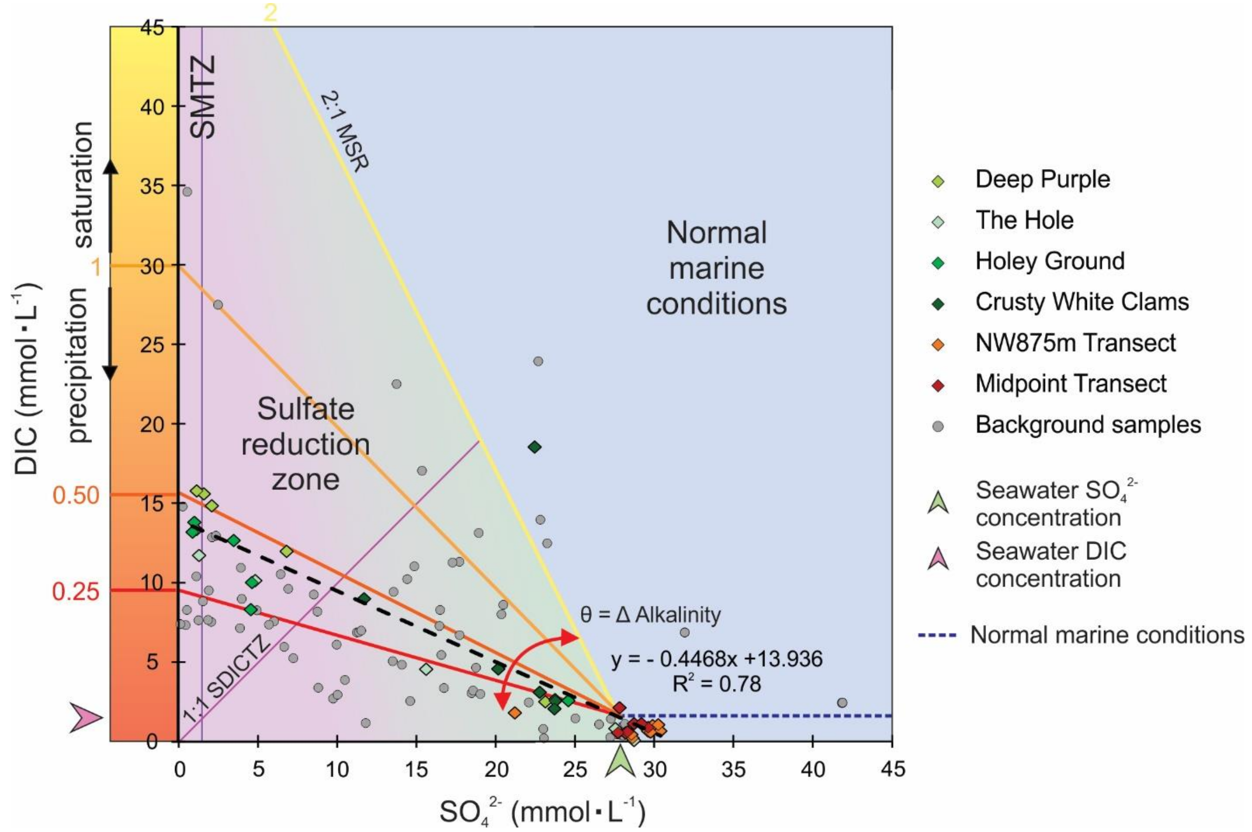

Figure 3.6: Composite cross-plot of sulfate and carbonate porewater concentrations of the push core transect. Black dotted line indicates the PLS regression line (R^2=0.78) formed from the site 2A-1 core transect samples (colored diamonds). The strong correlation suggests a geochemical dependence for these two anions interpreted here to be microbially driven redox reactions associated with concomitant changes in alkalinity. Colored regions mark stochiometric equivalent zones where MSR (green), anaerobic methane oxidizing archaea (ANME; transitioning to pink), and AOM (within purple line) are expected to occur. Colored lines mark varying rates of alkalinity associated with the ion pair (with m indicating the slope of the line). Ratio tie-lines (1:1 and 2:1) are uncorrected for calcium and magnesium loss by authigenic carbonate precipitation. Background samples are a series of SO_4^{2-} and DIC measurements from cores from the 2015, 2016, 2018, and 2021 sampling expeditions (Nikita, 2022).

Additionally, the regression slope of the inverse SO_4^{2-} and DIC arise by different gradient changes in the system. As such, the relationship need not be fixed to a specific slope and should in fact change from seep to seep as a function of the unique alkalinity conditions within the specific monitored environment. It is therefore expected that the activity rate of carbonate production and its removal by precipitation determines the regression slope of a measured seep system. A theoretical outline of this model is described in Appendix Figure A3.1. Treating average seawater sulfate conditions, 28 mmol·L^{-1} as a fixed point on the x-axis, four slopes describing different alkalinity conditions are proposed (Fig. 3.6). Porewater pairs plotting below a slope of 1 characterize increasing carbonate precipitation with low alkalinity co-occurring within a high carbonate production environment. Slopes >1 denote high alkalinity conditions characteristic of carbonate saturation arising from high production and low sequestration due to Ca^{2+} and Mg^{2+} limitation. Furthermore, the manner in which samples within the same core are spaced along a regression slope dictates overall seepage rate of a system (Appendix Fig. A1.5). Diffusion limited environmental systems will equally spaced ion concentration pairs. Progressively elevated diffusion fluxes arise when the distribution of ion concentration pairs are more weighted the to the higher end of their regression slopes.

The predictive power of this technique is limited to sample sets having ion concentrations that change along a gradient. As such, for locations such as cores 5 and 6 where no gradient changes have occurred, these data sets plot exclusively in the normal marine conditions zone, indicating no changes in alkalinity. Most samples on the Scotian Slope, including all seep cores from site 2A-1, plot within a range of low to moderate alkalinity in a zone of carbonate precipitation. Most of the regional Scotian Slope samples plot within similar ranges. Lastly, although, the comparative relationships are intrinsically depth independent, the 2A-1 seep samples are observed to be dispersed across Figure 3.6 in a depth constrained redox order consistent with the existence of diffusion and non-diffusion limited core sites that independently provide an indication of seepage activities (Appendix Figure A3.1). Based on this analysis, site 2A-1 is proposed to mark a moderate alkaline environment with a shallow SMTZ impacted by CH_4 seepage.

3.4.4 Targeted Ion Diffusion Fluxes at the Sediment-Water Interface

Calculation of a porewater ion diffusion flux enables tracking of the rate by which ions move from high to low zones of concentration. Additionally, ionic fluxes can influence the diagenetic alteration of minerals and the overall geochemical balance between sediments and the overlying water column. The diffusion flux of quantified porewater ions was measured according to Fick's First Law (Eq. 5) for five targeted ions based on their availability and importance in biogeochemical cycles. The concentrations of denitrification-based electron acceptors (NO_2^- and NO_3^-) were summed for this calculation. Heatmaps were generated as a novel means of displaying the downcore ion concentrations across the seep transect to define the geochemical boundary of the seep (Fig. 3.7).

Diffusion flux was observed exclusively in the seep and is most prominent in SO_4^{2-} and DIC. A smaller negative flux occurs in NH_4^+ at core 3, which is a direct consequence of the increased NH_4^+ concentrations in the 4-6 and 12-18 cm depth intervals. Negative gradients indicate increasing ion concentrations with depth. No observable flux was established with the combined NO_2^- and NO_3^- concentrations; these remained relatively steady across the seep, which is also reflected in the heat map.

SO_4^{2-} and DIC have the steepest concentration gradients and therefore the highest diffusion fluxes in the seep. The SO_4^{2-} and DIC heat maps highlight the previously observed inverse correlation between zones of high concentration and depletion. The SO_4^{2-} diffusion flux across the seep transect has an inverse relationship to the CH_4 profile. The SO_4^{2-} profile in the seep is indicative of an upwards CH_4 flux (Borowski et al., 1996). The CH_4 concentration decreases moving from the seep to the transect, which lowers the height of the SMTZ and increases the depth of SO_4^{2-} availability in the sediment.

Higher concentrations of NO_2^- and NO_3^- in surface sediments are likely related to the shallow nitrogen cycle. Nitrification and denitrification processes occur in consecutive order, resulting in the near zero diffusive flux. However, based on the porewater profiles, denitrification processes increase with depth, decreasing the concentration of both ions (Cochran et al., 2022). Both processes appear to be largely unaffected by CH_4 availability.

NH_4^+ is only present within the seep in distinct sediment intervals in zones of high DIC concentration. These intervals may be evidence of dissimilatory nitrate reduction to ammonium (DRNA), but this can not be determined without the appropriate bacterial biomarkers.

Cross-plots of ion diffusion fluxes and total petroleum hydrocarbons (TPH) were generated to further examine the influence of seepage on each ionic species (Fig. 3.8). For SO_4^{2-} and DIC, higher TPH values are associated with higher flux, although this is not observed in core 3, where low TPH corresponds to higher fluxes. Both NH_4^+ and the combined NO_3^- and NO_2^- concentration appear to present a linear correlation with the TPH values, again, ignoring the outlier from core 3. The two transect cores consistently plot with low TPH values and low diffusion fluxes. From these results, it can be loosely interpreted that increased TPH concentrations lead to increased diffusion flux.

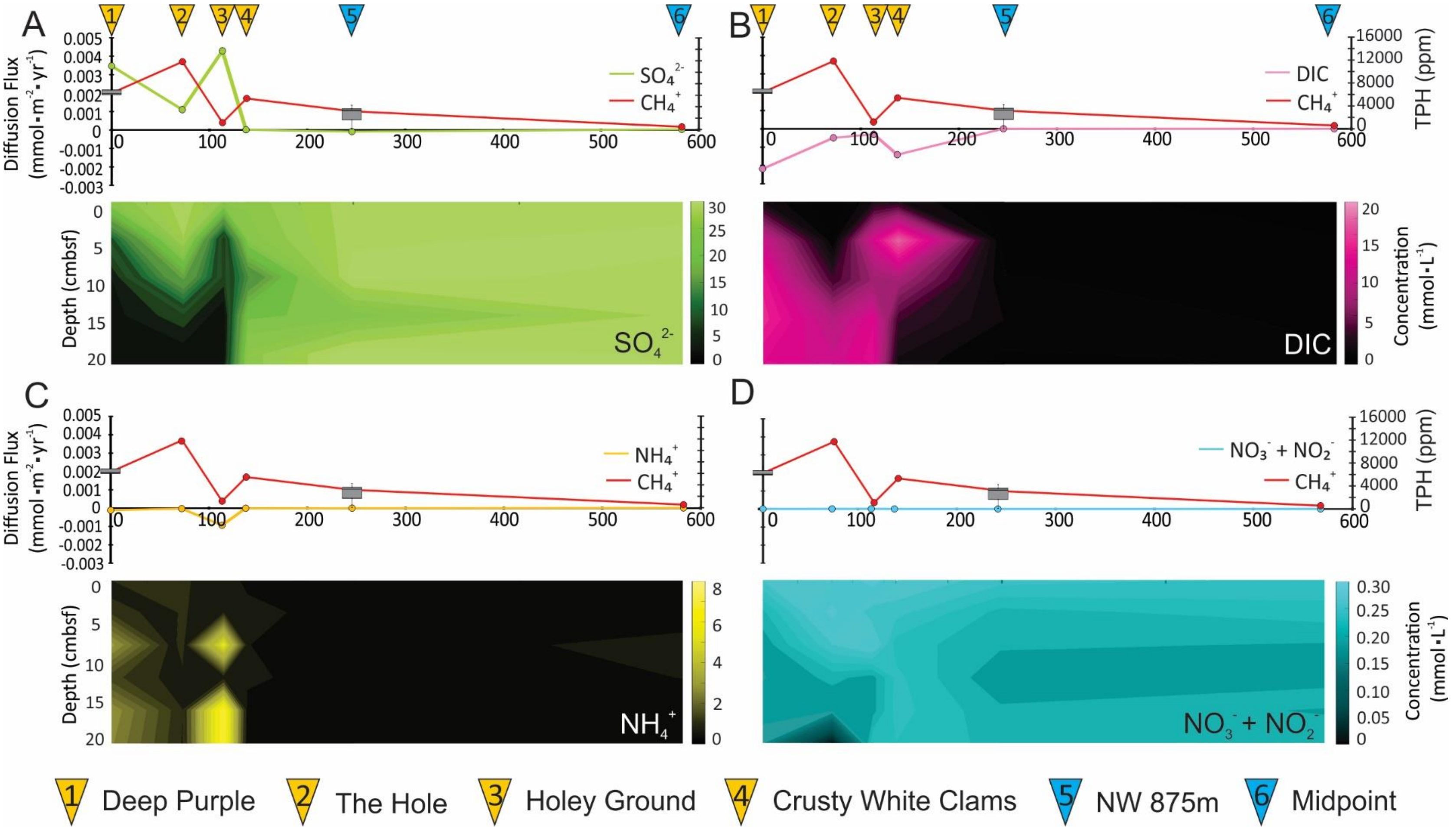

Figure 3.7: Cross-seep diffusion flux (top) and depth-distance interpolated porewater ion concentration heatmap (bottom) of A) SO_4^{2-}, B) DIC, C) NH_4^+, and D) NO_2^- and NO_3^- and total petroleum hydrocarbon (TPH) transect. TPH concentrations for site 2A-1 were provided by Martin Fowler of Applied Petroleum Technologies (open-source file) and Chowdhury et al. (2024).

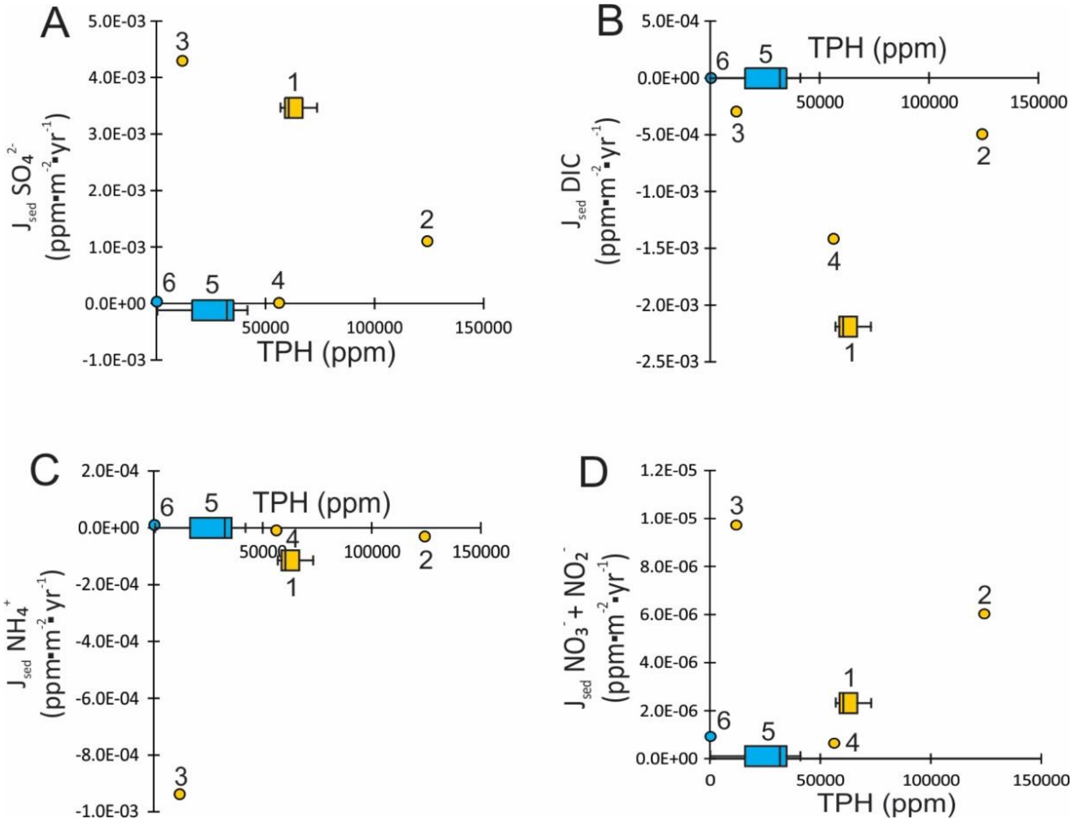

Figure 3.8: Specific ion diffusion flux and TPH cross plots. Seep cores are presented in yellow and transect cores in blue. Box plots present open-source data from Martin Fowler and circles for data from Chowdhury et al. (2024).

3.4.5 Porewater Seep Architecture

The 2A-1 porewater seep architecture (Fig. 3.9) is reconstructed by creating an overlay of each targeted ion's enrichment zone from generated porewater ion concentration heat maps (Fig. 3.7) and the proposed metabolic zones established by the inverse relationships of SO_4^{2-} and DIC (Fig. 3.6). In doing so, it should be noted that heatmaps are partially idealized constructs that assume uniformity across the seep structure. Carbonate mounds, often dominated by thick bivalve communities, form a larger part of the seep platform structure. Sampling locations were selected based on soft sediment availability and their expected geochemical potential to resolve seepage. It also must be noted that the surveyed transect is a snapshot of a geochemical profile of a much larger and complex structure that is likely continuously changing with time. Nonetheless, presenting porewater ion concentrations as heatmaps, provides a novel means of visualizing biogeochemical cycles and their material transfer pathways.

The depth at which denitrification occurs is controlled by the amount of dissolved oxygen in shallow sediment. Where dissolved oxygen was not measured at Site 2A-1, the proposed zone of denitrification is defined by elevated concentrations of NO_2^- and NO_3^- within the shallow seep sediments. Following the redox tower, the zone of microbial sulfate reduction falls below denitrification and above the SMTZ. Like NO_2^- and NO_3^-, SO_4^{2-} concentrations were highest in the shallowest seep sediments and decreased with depth. Concentrations of SO_4^{2-} in the transect were more representative of normal marine conditions, therefore the zone of MSR was confined to the seep sediments. The presence of microbial mats, like those observed at core 1, and the bivalve communities of cores 2, 3, and 4 support observations of shallow nitrogen and sulfur cycles. Microbial mats and macrofaunal symbionts oxidize bisulfide (HS^-) and hydrogen sulfide (H_2S) through NO_3^- and O_2 pathways (Canfield & Des Marais, 1993; Jørgensen & Kasten, 2006; Suess, 2020).

Samples falling to the left of the 1:1 AOM line in Fig. 3.6 are assumed to host a mixed SRB and ANME community. This line is described as the sulfate-carbonate interface and denotes the start of AOM conditions. When using the samples within Figure 3.6's sulfate-carbonate interface, a shallow boundary can be drawn across the seep, extending to core 4, the outermost seep sample.

Metal-AOM pathways, which reduce $Fe(OH)_3$ and MnO_2 result in free Fe^{2+} and Mn^{2+} ions, capable of reacting with HCO_3^- to produce mixed Fe and Mn carbonate phases (Beal et al., 2009). Both Fe^{2+} and Mn^{2+} concentrations were present in such low concentrations compared to SO_4^{2-} and presented no remarkable downcore trends. Metal-AOM is likely not occurring in this system or is not the main AOM reaction occurring and is being overprinted by more traditional AOM signatures.

Where porewater concentration of CH_4 were not available for this project the depth of the STMZ must be estimated through other means. Within the deepest seep sediments, a tentative SMTZ was proposed based on the low SO_4^{2-} content of the porewater. Measurements of CH_4 presented in Fig. 3.7 were recorded from the deepest sediment sample from each sampling location. This is one of the last reactions occurring along the redox tower. Chowdhury et al. (2024) also suggested microenvironments within the seep may likely experience methanogenesis.

The geochemical gradients observed at Site 2A-1 influence the spatial distribution of biogeochemical processes and likely microbial communities mediating those reactions. Similar downcore redox gradients have been observed in cold seep sediments from the Black Sea (Jørgensen et al., 2001; Niemann et al., 2006; Reitz et al., 2011), South China Sea (Cao & Lei, 2012; Luo et al., 2013; Chen et al., 2023), Gulf of Mexico (Joye et al., 2004; Joye et al., 2010; Formolo & Lyons, 2013; Bowles et al., 2016), and Mediterranean Sea (Werne et al., 2004; Haese et al., 2006; Pop Ristova et al., 2015), where extensive cold seep studies have taken place. These studies have laid the groundwork for constructing the porewater seep architecture of Site 2A-1. Changes in the microbial and macrofauna community structure as a function of seep proximity support the differentiation of metabolic zones based on metabolite availability (Lloyd et al., 2010; Cao et al., 2015; Bowles et al., 2016).

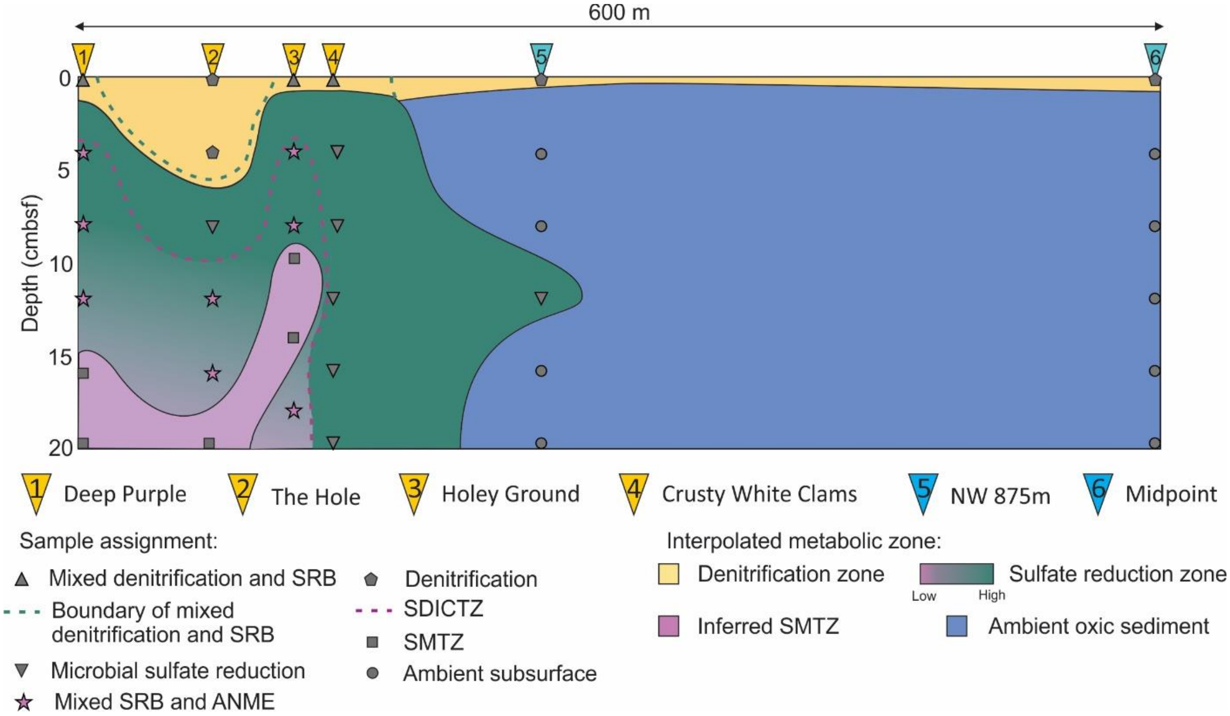

Figure 3.9: Reconstruction of the 2A-1 seep site's geochemical changes based on mapped zones of porewater ion enrichment and associated microbial metabolic redox ranges. Downcore data points and their corresponding microbial metabolisms are derived from the porewater ion data (Figs 3.6–3.7).

3.5. Conclusion

A porewater ion survey is the first step in the formation of a more comprehensive seep architecture reconstruction. This study analyzed the porewater ions of sediment push cores collected along a transect at seep site 2A-1 in the Scotian Slope. Five ions were selected to reconstruct the porewater seep architecture based on concentration, organic matter oxidation trends, and previously established seep metabolic reactions. Ion gradient heat maps are a novel approach to visualize two-dimensional changes in porewater concentrations and can reveal unique relationship between ionic species. Increased concentrations of NO_3^-, NO_2^-, and NH_4^+ in the shallow sediment indicate the presence of a shallow nitrogen cycle. The inverse relationship between concentrations of SO_4^{2-} and DIC tentatively identifies AOM activity within the SMTZ in the absence of a CH_4 profile and microbial data. The relationship was observed throughout a larger

Scotian Slope data set. Samples within the proposed SMTZ within Figure 3.6 plotted within the SO_4^{2-} and DIC transition zone within Figure 3.9. Evidence of AOM activity supports the presence of both the carbon and sulfur cycle. This study cannot provide insights to quantitative material flow between geochemical cycles, but instead allows for a tractable qualitative approach to visualizing carbon, nitrogen, and sulfur cycling within a cold seep ecosystem.

References

Adebayo, O., Bhatnagar, S., Webb, J., Campbell, C., Fowler, M., MacAdam, N. M., Macdonald, A., Li, C., & Hubert, C. R. J. (2024). Hydrocarbon-degrading microbial populations in permanently cold deep-sea sediments in the NW Atlantic. *Marine Pollution Bulletin*, *208*, 117052. https://doi.org/10.1016/j.marpolbul.2024.117052

Barnes, R. O., & Goldberg, E. D. (1976). Methane production and consumption in anoxic marine sediments. *Geology*, *4*(5), 297. https://doi.org/10.1130/0091-7613(1976)4<297:MPACIA>2.0.CO;2

Beal, E. J., House, C. H., & Orphan, V. J. (2009). Manganese- and Iron-Dependent Marine Methane Oxidation. *Science*, *325*(5937), 184–187. https://doi.org/10.1126/science.1169984

Bennett, R., & Desiage, P.-A. (2022). *Expedition report 21CONDOR: Scotian Slope, August 14-29, 2021* (8889; p. 8889). https://doi.org/10.4095/329977

Berner, R. A. (1980). *Early diagenesis: A theoretical approach*. Princeton University Press.

Boetius, A., Ravenschlag, K., Schubert, C. J., Rickert, D., Widdel, F., Gieseke, A., Amann, R., Jørgensen, B. B., Witte, U., & Pfannkuche, O. (2000). A marine microbial consortium apparently mediating anaerobic oxidation of methane. *Nature*, *407*(6804), 623–626. https://doi.org/10.1038/35036572

Borowski, W. S., Paull, C. K., & Ussler, W. (1996). Marine pore-water sulfate profiles indicate in situ methane flux from underlying gas hydrate. *Geology*, *24*(7), 655. https://doi.org/10.1130/0091-7613(1996)024<0655:MPWSPI>2.3.CO;2

Bowles, M., Hunter, K. S., Samarkin, V., & Joye, S. (2016). Patterns and variability in geochemical signatures and microbial activity within and between diverse cold seep habitats along the lower continental slope, Northern Gulf of Mexico. *Deep Sea Research Part II: Topical Studies in Oceanography*, *129*, 31–40. https://doi.org/10.1016/j.dsr2.2016.02.011

Burdige, D. J., & Komada, T. (2011). Anaerobic oxidation of methane and the stoichiometry of remineralization processes in continental margin sediments. *Limnology and Oceanography*, *56*(5), 1781–1796. https://doi.org/10.4319/lo.2011.56.5.1781

Canfield, D. E. (2004). The evolution of the Earth surface sulfur reservoir. *American Journal of Science*, *304*(10), 839–861. https://doi.org/10.2475/ajs.304.10.839

Canfield, D. E., & Des Marais, D. J. (1993). Biogeochemical cycles of carbon, sulfur, and free oxygen in a microbial mat. *Geochimica et Cosmochimica Acta*, *57*(16), 3971–3984. https://doi.org/10.1016/0016-7037(93)90347-Y

Cao, C., & Lei, H. (2012). Geochemical characteristics of pore water in shallow sediments from north continental slope of South China Sea and their significance for natural gas hydrate occurrence. *Procedia Environmental Sciences*, *12*, 1017–1023. https://doi.org/10.1016/j.proenv.2012.01.381

Cao, H., Zhang, W., Wang, Y., & Qian, P.-Y. (2015). Microbial community changes along the active seepage site of one cold seep in the Red Sea. *Frontiers in Microbiology*, *6*. https://doi.org/10.3389/fmicb.2015.00739

Chen, C., Wu, X., Wan, Z., Shang, J., Huang, W., Zhang, W., Liang, J., Xiao, Z., Zhou, W., & Zhong, L. (2023). Geochemical characteristics of sediment and pore water affected by cold seeps in southern South China Sea. *Frontiers in Marine Science*, *10*, 1167578. https://doi.org/10.3389/fmars.2023.1167578

Chowdhury, A., Ventura, G. T., Owino, Y., Lalk, E. J., MacAdam, N., Dooma, J. M., Ono, S., Fowler, M., MacDonald, A., Bennett, R., MacRae, R. A., Hubert, C. R. J., Bentley, J. N., & Kerr, M. J. (2024). Cold seep formation from salt diapir–controlled deep biosphere oases. *Proceedings of the National Academy of Sciences*, *121*(12), e2316878121. https://doi.org/10.1073/pnas.2316878121

Cochran, J. K., Landman, N. H., Jakubowicz, M., Brezina, J., Naujokaityte, J., Rashkova, A., Garb, M. P., & Larson, N. L. (2022). Geochemistry of Cold Hydrocarbon Seeps: An Overview. In A. Kaim, J. K. Cochran, & N. H. Landman (Eds.), *Ancient Hydrocarbon Seeps* (Vol. 53, pp. 3–45). Springer International Publishing. https://doi.org/10.1007/978-3-031-05623-9_1

Formolo, M. J., & Lyons, T. W. (2013). Sulfur biogeochemistry of cold seeps in the Green Canyon region of the Gulf of Mexico. *Geochimica et Cosmochimica Acta*, *119*, 264–285. https://doi.org/10.1016/j.gca.2013.05.017

Gruber, N. (2004). The Dynamics of the Marine Nitrogen Cycle and its Influence on Atmospheric CO2 Variations. In M. Follows & T. Oguz (Eds.), *The Ocean Carbon Cycle and Climate* (pp. 97–148). Springer Netherlands. https://doi.org/10.1007/978-1-4020-2087-2_4

Haese, R. R., Hensen, C., & De Lange, G. J. (2006). Pore water geochemistry of eastern Mediterranean mud volcanoes: Implications for fluid transport and fluid origin. *Marine Geology*, *225*(1–4), 191–208. https://doi.org/10.1016/j.margeo.2005.09.001

Hinrichs, K.-U., Hayes, J. M., Sylva, S. P., Brewer, P. G., & DeLong, E. F. (1999). Methane-consuming archaebacteria in marine sediments. *Nature*, *398*(6730), 802–805. https://doi.org/10.1038/19751

Jørgensen, B. B., & Kasten, S. (2006). Sulfur Cycling and Methane Oxidation. In H. D. Schulz & M. Zabel (Eds.), *Marine Geochemistry* (pp. 271–309). Springer-Verlag. https://doi.org/10.1007/3-540-32144-6_8

Jørgensen, B. B., Weber, A., & Zopfi, J. (2001). Sulfate reduction and anaerobic methane oxidation in Black Sea sediments. *Deep Sea Research Part I: Oceanographic Research Papers*, *48*(9), 2097–2120. https://doi.org/10.1016/S0967-0637(01)00007-3

Joye, S. B., Boetius, A., Orcutt, B. N., Montoya, J. P., Schulz, H. N., Erickson, M. J., & Lugo, S. K. (2004). The anaerobic oxidation of methane and sulfate reduction in sediments from Gulf of Mexico cold seeps. *Chemical Geology*, *205*(3–4), 219–238. https://doi.org/10.1016/j.chemgeo.2003.12.019

Joye, S. B., Bowles, M. W., Samarkin, V. A., Hunter, K. S., & Niemann, H. (2010). Biogeochemical signatures and microbial activity of different cold-seep habitats along the Gulf of Mexico deep slope. *Deep Sea Research Part II: Topical Studies in Oceanography*, *57*(21–23), 1990–2001. https://doi.org/10.1016/j.dsr2.2010.06.001

Judd, A. G., Hovland, M., Dimitrov, L. I., García Gil, S., & Jukes, V. (2002). The geological methane budget at Continental Margins and its influence on climate change. *Geofluids*, *2*(2), 109–126. https://doi.org/10.1046/j.1468-8123.2002.00027.x

Knittel, K., & Boetius, A. (2009). Anaerobic Oxidation of Methane: Progress with an Unknown Process. *Annual Review of Microbiology*, *63*(1), 311–334. https://doi.org/10.1146/annurev.micro.61.080706.093130

Kuypers, M. M. M., Sliekers, A. O., Lavik, G., Schmid, M., Jørgensen, B. B., Kuenen, J. G., Sinninghe Damsté, J. S., Strous, M., & Jetten, M. S. M. (2003). Anaerobic ammonium oxidation by anammox bacteria in the Black Sea. *Nature*, *422*(6932), 608–611. https://doi.org/10.1038/nature01472

Levin, L. A. (2005). Ecology of Cold Seep Sediments: Interactions of Fauna with Flow, Chemistry and Microbes. In *Oceanography and Marine Biology*. CRC Press.

Liu, W., Wu, Z., Xu, S., Wei, J., Peng, X., Li, J., & Wang, Y. (2020). Pore-water dissolved inorganic carbon sources and cycling in the shallow sediments of the Haima cold seeps, South China Sea. *Journal of Asian Earth Sciences*, *201*, 104495. https://doi.org/10.1016/j.jseaes.2020.104495

Lloyd, K. G., Albert, D. B., Biddle, J. F., Chanton, J. P., Pizarro, O., & Teske, A. (2010). Spatial Structure and Activity of Sedimentary Microbial Communities Underlying a Beggiatoa spp. Mat in a Gulf of Mexico Hydrocarbon Seep. *PLoS ONE*, *5*(1), e8738. https://doi.org/10.1371/journal.pone.0008738

Luo, M., Chen, L., Wang, S., Yan, W., Wang, H., & Chen, D. (2013). Pockmark activity inferred from pore water geochemistry in shallow sediments of the pockmark field in southwestern Xisha Uplift, northwestern South China Sea. *Marine and Petroleum Geology*, *48*, 247–259. https://doi.org/10.1016/j.marpetgeo.2013.08.018

Milkov, A. V. (2004). Global estimates of hydrate-bound gas in marine sediments: How much is really out there? *Earth-Science Reviews*, *66*(3–4), 183–197. https://doi.org/10.1016/j.earscirev.2003.11.002

Mucci, A., Sundby, B., Gehlen, M., Arakaki, T., Zhong, S., & Silverberg, N. (2000). The fate of carbon in continental shelf sediments of eastern Canada: A case study. *Deep Sea Research Part II: Topical Studies in Oceanography*, *47*(3–4), 733–760. https://doi.org/10.1016/S0967-0645(99)00124-1

Niemann, H., Duarte, J., Hensen, C., Omoregie, E., Magalhães, V. H., Elvert, M., Pinheiro, L. M., Kopf, A., & Boetius, A. (2006). Microbial methane turnover at mud volcanoes of the Gulf of Cadiz. *Geochimica et Cosmochimica Acta*, *70*(21), 5336–5355. https://doi.org/10.1016/j.gca.2006.08.010

Nikita. (2022). *Survey of porewater geochemistry within deep marine hydrocarbon seep sediments of the Scotian Slope, Canada*. Saint Mary's University Institutional Repository; Honours Thesis.

Orcutt, B. N., LaRowe, D. E., Biddle, J. F., Colwell, F. S., Glazer, B. T., Reese, B. K., Kirkpatrick, J. B., Lapham, L. L., Mills, H. J., Sylvan, J. B., Wankel, S. D., & Wheat, C. G. (2013). Microbial activity in the marine deep biosphere: Progress and prospects. *Frontiers in Microbiology*, *4*. https://doi.org/10.3389/fmicb.2013.00189

Orphan, V. J., Hinrichs, K.-U., Ussler, W., Paull, C. K., Taylor, L. T., Sylva, S. P., Hayes, J. M., & Delong, E. F. (2001). Comparative Analysis of Methane-Oxidizing Archaea and Sulfate-Reducing Bacteria in Anoxic Marine Sediments. *Applied and Environmental Microbiology*, *67*(4), 1922–1934. https://doi.org/10.1128/AEM.67.4.1922-1934.2001

Pop Ristova, P., Wenzhöfer, F., Ramette, A., Felden, J., & Boetius, A. (2015). Spatial scales of bacterial community diversity at cold seeps (Eastern Mediterranean Sea). *The ISME Journal*, *9*(6), 1306–1318. https://doi.org/10.1038/ismej.2014.217

Reeburgh, W. S. (2007). Oceanic Methane Biogeochemistry. *Chemical Reviews*, *107*(2), 486–513. https://doi.org/10.1021/cr050362v

Reitz, A., Pape, T., Haeckel, M., Schmidt, M., Berner, U., Scholz, F., Liebetrau, V., Aloisi, G., Weise, S. M., & Wallmann, K. (2011). Sources of fluids and gases expelled at cold seeps offshore Georgia, eastern Black Sea. *Geochimica et Cosmochimica Acta*, *75*(11), 3250–3268. https://doi.org/10.1016/j.gca.2011.03.018

Regnier, P., Dale, A. W., Arndt, S., LaRowe, D. E., Mogollón, J., & Van Cappellen, P. (2011). Quantitative analysis of anaerobic oxidation of methane (AOM) in marine sediments: A modeling perspective. *Earth-Science Reviews*, *106*(1), 105–130. https://doi.org/10.1016/j.earscirev.2011.01.002

Rooze, J., Peterson, L., Peterson, R. N., & Meile, C. (2020). Porewater flow patterns in surficial cold seep sediments inferred from conservative tracer profiles and early diagenetic modeling. *Chemical Geology*, *536*, 119468. https://doi.org/10.1016/j.chemgeo.2020.119468

Schulz, H. D. (2000). Quantification of Early Diagenesis: Dissolved Constituents in Marine Pore Water. In H. D. Schulz & M. Zabel (Eds.), *Marine Geochemistry* (pp. 85–128). Springer Berlin Heidelberg. https://doi.org/10.1007/978-3-662-04242-7_3

Solomon, E. A., Kastner, M., Jannasch, H., Robertson, G., & Weinstein, Y. (2008). Dynamic fluid flow and chemical fluxes associated with a seafloor gas hydrate deposit on the northern Gulf of Mexico slope. *Earth and Planetary Science Letters*, *270*(1–2), 95–105. https://doi.org/10.1016/j.epsl.2008.03.024

Sommer, S., Pfannkuche, O., Linke, P., Luff, R., Greinert, J., Drews, M., Gubsch, S., Pieper, M., Poser, M., & Viergutz, T. (2006). Efficiency of the benthic filter: Biological control of the emission of dissolved methane from sediments containing shallow gas hydrates at Hydrate Ridge. *Global Biogeochemical Cycles*, *20*(2). https://doi.org/10.1029/2004GB002389

Suess, E. (2020). Marine Cold Seeps: Background and Recent Advances. In H. Wilkes (Ed.), *Hydrocarbons, Oils and Lipids: Diversity, Origin, Chemistry and Fate* (pp. 747–767). Springer International Publishing. https://doi.org/10.1007/978-3-319-90569-3_27

Vairavamurthy, M. A., Orr, W. L., & Manowitz, B. (1995). Geochemical Transformations of Sedimentary Sulfur: An Introduction. In *Geochemical Transformations of Sedimentary Sulfur* (Vol. 612, pp. 1–14). American Chemical Society. https://doi.org/10.1021/bk-1995-0612.ch001

Werne, J. P., Haese, R. R., Zitter, T., Aloisi, G., Bouloubassi, I., Heijs, S., Fiala-Médioni, A., Pancost, R. D., Sinninghe Damsté, J. S., De Lange, G., Forney, L. J., Gottschal, J. C., Foucher, J.-P., Mascle, J., & Woodside, J. (2004). Life at cold seeps: A synthesis of biogeochemical and ecological data from Kazan mud volcano, eastern Mediterranean Sea. *Chemical Geology*, *205*(3–4), 367–390. https://doi.org/10.1016/j.chemgeo.2003.12.031

Zeebe, R. E., & Wolf-Gladrow, D. (2001). Chapter 1 Equilibrium. In *Elsevier Oceanography Series* (Vol. 65, pp. 1–84). Elsevier. https://doi.org/10.1016/S0422-9894(01)80002-7

Chapter 4: Microbial Lipidomic Transect Survey and Geochemical Seep Architecture Reconstruction of Cold Seep Site 2A-1, Scotian Slope, Atlantic Canada

Abstract

Reduced fluid seepage at deep marine cold seeps creates a diverse microbiome that is unique from the surrounding ocean floor sediments. To better understand the extent of alteration from fluid seepage, a six-push core transect was collected from a newly discovered Scotian Slope cold seep Site 2A-1 to describe the lipidome and monitor changes along an environmental gradient. Intact polar lipids and core lipids were extracted from 76 sediment samples using a modified Bligh and Dyer protocol and analysed using reversed-phase high performance liquid chromatography. Twenty-three lipid classes, predominantly sourced from Archaea, were tentatively identified across the transect. Lipid concentrations were visualized as downcore profiles as well as two-dimensional density heatmaps. Increased lipidomic diversity is shown to exit within the seep. Higher level lipid degradation rates are further revealed by downcore profiles of crenarchaeal and photosynthetic pigments. Biomarker lipid proxies indicate an ANME-1 community and high levels of anaerobic oxidation of methane activity. Principal Component Analysis on the lipid classes revealed that 55% of the variance can be explained by the first two components, which presumably separate classes based on concentration and relation to seepage activity. The addition of porewater ions revealed correlation between lipid classes and the geochemical environment. The combined lipidomic and porewater survey enabled the creation of a novel two-dimensional reconstruction of the microbial and geochemical seep architecture.

4.1. Introduction

Highly reduced fluid seepage at deep marine cold seeps sustains unique ecosystems distinct from the surrounding ocean floor (Levin, 2005; Suess, 2020). Cold seep sediments host diverse microbial communities that convert available volatile hydrocarbons into living biomass. The cellular membrane lipids of the chemosynthetic microbial consortia can be used to provide insights to community structure and dynamics of cold seeps. Lipids from all three domains of life, Bacteria, Archaea, and Eukaryotes, have been identified in marine sediments. The structural configuration of archaeal lipids fundamentally differs from those of Bacteria and Eukaryotes (Koga et al., 1993; Valentine, 2007). In Archaea, hydrocarbon chains are bound to the glycerol moiety exclusively by ether linkages. Bacteria and Eukaryotes have ester linkages between fatty acid chains and a glycerol moiety (Koga & Morii, 2005).

Characterization of the cold seep lipidome relies on the presence of intact polar lipid (IPL) and core lipid (CL) biomarkers. Intact polar lipids are lipids found in their biological form with a polar headgroup attached. Based on the assumed labile nature of the polar head groups (White et al., 1979), IPLs are considered to be the product of living cells (Sturt et al., 2004) and indicate the conditions of a modern seep environment. Individual lipid classes are chemotaxonomically unique (Rütters et al., 2002; Schubotz et al., 2009; Elling et al., 2017) and are specific to their environment (Yunker et al., 2005; Rossel et al., 2008; Pitcher et al., 2011). Core lipids can persist for millions of years in marine sediments (e.g., Kuypers et al., 2001), representing extant or fossilized biomass. The perseverance of CLs lends to their use as biomarkers to trace paleoenvironmental conditions and changes.

Glycerol dialkyl glycerol tetraethers (GDGTs) are the most widespread group of archaeal lipids and their abundance allows them to be used as molecular biomarkers for modern and ancient marine environments. Within this context, ratios, such as the TEX_{86} (Schouten et al., 2002) and the methane index (MI) (Y. Zhang et al., 2011) are popular for interpreting geological conditions of the past. Ratios are magnitude non-dependent; they provide valuable information on paleoenvironmental conditions but no information on system energetics.

Distinct lipid classes are associated with fluid seepage (Boetius et al., 2000; Orphan, Hinrichs, et al., 2001). A consortium of anaerobic oxidizing archaea (ANME) and sulfate reducing bacteria (SRB) (Hinrichs et al., 1999; Boetius et al., 2000) regulates the efflux of methane from marine sediments to the atmosphere through the anaerobic oxidation of methane (AOM; equation 1). Anaerobic methane oxidation predominantly occurs in the sulfate-methane transition zone (SMTZ), a dynamic sediment interval where non-zero concentrations methane (CH_4) and sulfate (SO_4^{2-}) overlap (R. Barnes & Goldberg, 1976). Biomarkers of AOM include 3 classes of ANME (-1, -2, -3), all distantly related to methanogens from the orders *Methanosarcinales* and *Methanomicrobiales* (Boetius et al., 2000; Knittel et al., 2005; Orphan et al., 2002) and each can be distinguished by their associated sulfate reducing bacteria partners (Boetius et al., 2000; Niemann et al., 2006) and lipid biomarker ratios (Blumenberg et al., 2004; Niemann & Elvert, 2008).

$$CH_4 + SO_4^{2-} \rightarrow HCO_3^- + HS^- + H_2O \quad (1)$$

Anaerobic methane oxidation by-products include bisulfide (HS^-) and bicarbonate (HCO_3^-), each of which lend themselves to further reactions within the seep. Bisulfide is a highly sought after substrate for sulfur-oxidizing bacterial communities within microbial mats as well as symbiotic macrofauna. Free metal ions in the system can react with HS^- to form iron sulfides or participate in secondary metal-AOM pathways. The precipitation of cold seep carbonates stems from HCO_3^-, produced either by AOM or methanogenesis, reacting with magnesium (Mg^{2+}) and calcium (Ca^{2+}).

Cold seeps can indicate the presence of a subsurface petroleum reservoir. Oil and gas exploration on the Scotian Margin began in the 1960's and focused on salt canopies in the shallow shelf waters (Kendell, 2012). Since the decommissioning of the Deep Panuke Project in 2018, more recent exploration expeditions have focused on deep water prospects, targeting seabed direct hydrocarbon indicators on the Scotian Slope. Site 2A-1 was identified by the presence of multiple direct hydrocarbon indicators and previous promising metagenomic and hydrocarbon gas analyses (Campbell, 2019; Bennett & Desiage, 2022). The cold seep is teaming with benthic fauna, authigenic carbonates, and a stream of gas seeping from a central depression.

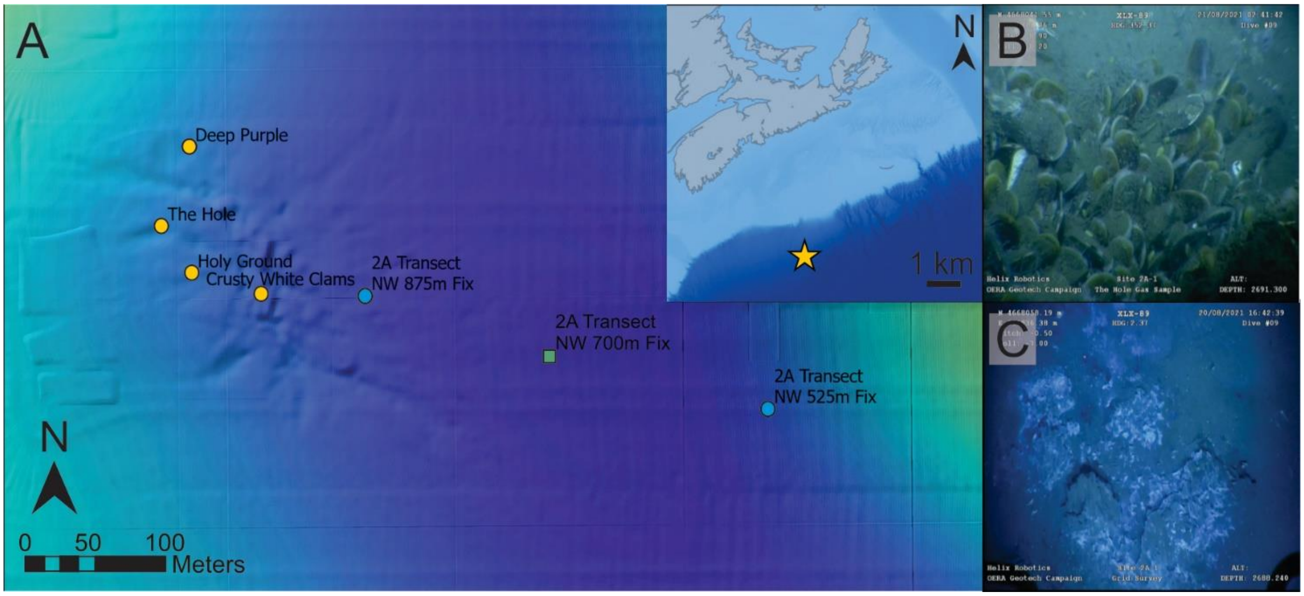

Figure 4.1: A) 2A-1 Site location. Yellow circles represent seep cores and blue circles for the transect. The green square denotes the core from which ^{14}C measurements were obtained. Images captured by ROV at the seep revealed B) dense bivalve beds and C) microbial mats.

These complex microbial systems are likely stratified and spatially chemically controlled. To better understand microbial community dynamics and metabolic processes occurring at cold seeps, maps of individual ion concentrations and lipidomes can be reconstructed from the sediment and porewater profiles. This study uses a six push-core transect to map the stratigraphic trends of archaeal lipids, in addition to limited bacterial and eukaryotic lipids, within an active Scotian Slope biogenic cold seep. The transect intersects the seep centre and extends ~600 m into ambient sediments traversing a wide range of geochemical conditions. Porewater ion concentrations, provided from Chapter 3 Section 3.2, tentatively established a geochemical gradient within the seep largely driven by the concentrations of SO_4^{2-} and dissolved inorganic carbon (DIC) and founded in AOM. The results from the lipidomic survey build upon the porewater background to present a novel 2D reconstruction of the subsurface microbial and geochemical seep architecture.

4.2. Methodology

4.2.1 Sample Collection

In 2021, the Atlantic Condor, outfitted with MEOPAR's Modular Ocean Research Infrastructure (MORI), undertook a remotely operated vehicle (ROV) push coring cruise to the bottom of the Scotian Slope of Atlantic Canada. The ROV was a Triton XLX ROV, operated by Helix Robotics Solutions Ltd. A northwest-southeast trending, six push core, transect was collected at seep site 2A-1, located at approximately, 2500 m water depth (Fig. 4.1, Table 4.1). The transect includes four push cores that span a large portion of the seep structure and two push cores that were further collected from ambient sediments ~125 m and ~500 m southeast of the seep structure. Upon retrieval, the push cores were subsampled into 2-cm intervals, packed in baked aluminium foil, and immediately stored in a -80 °C freezer until they could be further processed.

Table 4.1: Push core sample collection locations and measurements.

Core Name	ID	Location (Lat., Long)	Water Depth (m)	Core Length (cm)
Deep Purple	2A-1, 36	42.163275, -62.372022	2686	28
The Hole	2A-1, 78	42.162698, -62.372356	2687	20
Holey Ground	2A-1, 18	42.162353, -62.302762	2688	24
Crusty White Clams	2A-1, 29	42.162198, -62.371378	2684	38
NW875m	2A-66	42.162180, -62.370351	2686	40
Midpoint	2A-41	42.161334, -62.366394	2693	36

4.2.2 Sedimentary Organic Carbon

4.2.2.1 Total Organic Carbon

Total organic carbon (TOC) was measured using a Perkin-Elmer 2400 Series II CHNS/O Elemental Analyzer (EA) located in the Centre for Environmental Analysis and Remediation, Saint Mary's University. The EA was programmed for CHN analysis (a full account of the procedure is provided in Chapter 3, Section 2.2).

4.2.2.2 Sedimentary Carbon Isotopes

Thirteen decarbonated sediment samples from 4 cores were additionally selected for $\delta^{13}C_{TOC}$ analysis. The samples were processed by the Isotope Science Laboratory at the University of Calgary, Alberta, Canada. Measurements were collected using Continuous Flow-Elemental Analysis-Isotope Ratio Mass Spectrometry coupled with an Elementary Isotope CUBE® elemental analyser. The stable isotope ratios are expressed as delta (δ) and measured as the per mill difference between the sample and the 'Vienna Peedee Belemnite' formation for Carbon (Craig, 1957).

4.2.2.3 Radiocarbon Measurements

Four sediment samples from an additional transect push core (Site 2A-49) were exported to the André E. Lalonde AMS Laboratory at the University of Ottawa (Ontario, Canada) for radiocarbon age dating. Samples were prepared following the methods outlined in Crann et al., (2017) and Murseli et al. (2019). ^{14}C yr BP (BP = AD 1950) measurements were collected using an Ionplus AG MICADAS (Mini Carbon Dating System).

4.2.3 Porewater

The extraction and preparation procedures for the porewater analysis can be found in Chapter 3, Section 2.3. Porewater ions were collected from alternating intervals dependant on instrumentation. Anions SO_4^{2-}, DIC, nitrate (NO_3^-), nitrite (NO_2^-), fluoride (F^-) were measured using a Thermo Scientific Dionex Aquion Chromatography Conductivity System. Ion concentrations were measured against an external calibration curve created by an anion standard (Thermo Scientific Dionex Seven Anion Standard II)/carbonate stock (2000 mg·L^{-1} Na_2CO_3)/HPLC water [2:1:1, v/v/v] with standard mixture dilutions of 0.5, 1, 2, 5, 10, 20, and 50 ppm. A Hanna Instruments Benchtop Multiparameter Photometer (HI-83300) was used to measure ammonium (NH_4^+), iron (Fe^{2+}), manganese (Mn^{2+}), and phosphate (PO_4^{3-}). Porewater availability limited measurements of Fe^{2+}, Mn^{2+}, and PO_4^{3-}.

4.2.4 Lipidomic Analysis

4.2.4.1 Lipid Extraction

Total Lipid Extracts (TLEs) were collected from frozen sediment following a modified Bligh and Dyer (MBD) protocol as outlined in (Bentley et al., 2022). Prior to extraction, each sediment sample was spiked with 1 µg·ml^{-1} of 1-alkyl-2-acetoyl-sn-glycero-3-phosphocholine (PAF), an internal standard. The MBD protocol employed a six-step extraction with three solvent mixtures. Each extraction used ~ 20 g of frozen sediment. Steps one through four use ~20 ml of a methanol (MeOH)/dichloromethane (DCM)/buffer [2:1:0.8; v/v/v] mix. The first two steps use a phosphate buffer (5.5 g·L^{-1} Na_2HPO_4 adjusted to pH of 7.4), with steps three and four using a trichloroacetic acid buffer (50 g·L^{-1} $C_2HCl_3O_2$, pH of 2). The final two steps were a ~20 ml MeOH/DCM [5:1; v/v] mix. For each extraction step, the solvent mixture was decanted and combined in a pre-combusted separation funnel. The resulting TLE was then thrice extracted with ~20 ml of DCM followed by ~20 ml of milli-Q water for purification. In between each extraction, the aqueous phase was separated from the organic phase and disposed of. Extracts were dried at 50 °C under a steady stream of dry nitrogen (N_2). Prior to injection, each extract was ingested in 2000 μL of MeOH/DCM [1:1] and filters through a 0.45-micron filter and injected with 2,2'-di-O-decyl-3,3'-di-O-(1'',ω''-eicosanyl)-1,1'-di-(rac-glycerol) C_{46}.

4.2.4.2 Mass Spectral Analysis

An aliquot representing 3% of the samples TLE was injected into an Agilent 1260 infinity high performance liquid chromatography-quadrupole time of flight mass spectrometer (HPLC-qToF-MS). The HPLC was fitted with a ZORBAX RRHD Eclipse Plus C18 column (2.1-mm × 150-mm × 1.8-μm) with an Agilent Guard Column maintained at 45 °C using a flow rate of 0.300 ml·min^{-1}. Two mobile phases and gradient elution were used for the separation. Mobile phase A (MeOH/formic acid (FA)/ammonium hydroxide (NH_4OH) [100:0.04:0.10] v/v/v) ran 100% for ten minutes and would then progressively mix with mobile phase B (propan-2-ol (IPA)/FA/NH_4OH [100:0.04:0.10] v/v). Mobile phases mixed on a linear gradient for an 85-min run.

4.2.4.3 Quantification

Lipids of interest were identified by their elution times, molecular ions [M^+], and respective fragmentation patterns in Agilent Technologies MassHunter 10.0 Software (Appendix Table A1-3). Integrated peak areas of the $[M+H]^+$, $[M+NH_4]^+$, and $[M+Na]^+$ adducts were summed in order to quantify targeted compounds. Concentrations were calculated relative to the C46:0 internal standard and injection dilution. Lipid concentrations are reported in $\mu g \cdot g^{-1}$ sediment weight.

4.2.5 Statistical Analysis

Principal component analysis (PCA) was carried out using the "factomineR" package in RStudio. The "psych" package was used to complete the Kaiser-Mayeer-Olkin (KMO) and Barlett's test on the data set prior to analysis. A KMO score above 0.6 and a p-value of <0.05 indicates that the data set is acceptable for PCA. The "factoextra" package was used to visualize the results of the PCA. A scree plot of the eigenvectors was used to determine the number of principal components to retain.

4.3. Results

4.3.1 Sedimentation rate and bulk organic matter trends

Radiocarbon age dates from core 2A-49 indicate an average sedimentation rate of $0.0038\ cm \cdot yr^{-1}$, or $259\ yr \cdot cm^{-1}$ (Appendix Table B2.1). Sedimentation rate has been calculated from adjusted ^{14}C values to account for reservoir effect, a phenomenon in which surface sediments appear older than they are as an effect of slow deposition in the water column (Fig. 4.2a). Dates are adjusted by subtracting the measured value of the 0-2 cmbsf sample. Sedimentation rate decreases with depth, although this may be an artifact of sediment compaction observed at the bottom of the core. Sediments reach a maximum age of 13777 ± 13 ^{14}C yr BP.

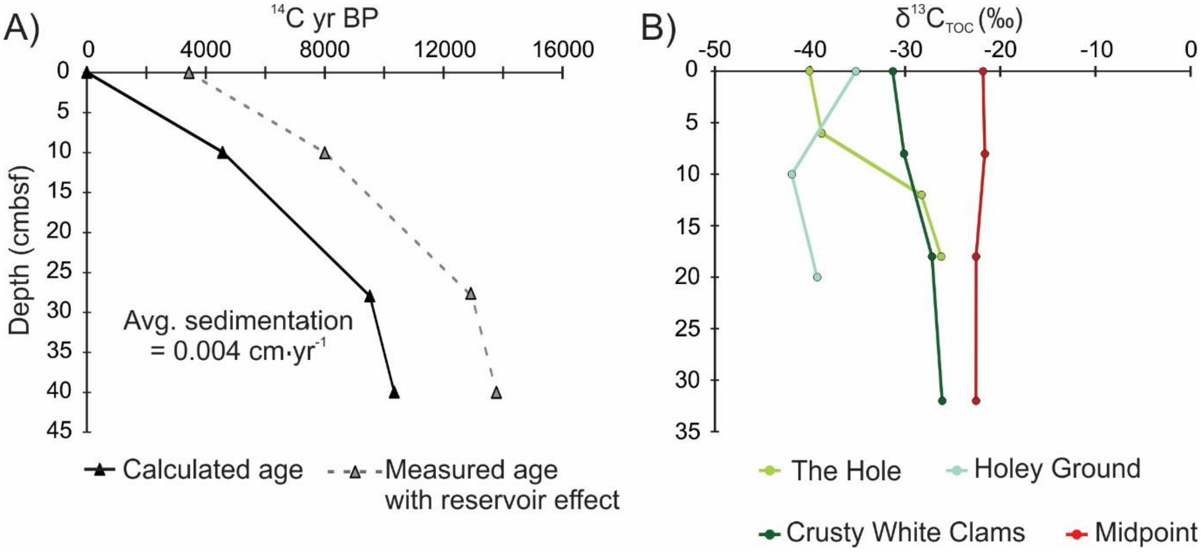

Figure 4.2: A) Sedimentation rate as determined from radiocarbon age data of core 2A-49. The rate is calculated from the reservoir effect adjusted ^{14}C age. B) Downcore profiles of δ^{13}C measurement.

The average TOC at site 2A-1 was 0.55 wt.% and ranged from 0.35 to 1.09 wt.%. Thirty-six measurements were recorded from the 4 seep cores. The TOC decreased with depth within the seep. No TOC was measured for NW 875m Transect and only 4 measurements were recorded for the Midpoint Transect. The TOC in Midpoint was far above the seep average (0.89 wt.%) and increased with depth. The δ^{13}C$_{TOC}$ was measured from 15 of TOC samples across 4 cores (Fig. 4.2b). The values of δ^{13}C$_{TOC}$ are more depleted within the seep sediments, and increase moving into the transect. The strongly depleted δ^{13}C$_{TOC}$ measurements from the 0-2 cmbsf interval are a strong indication of a shallow sediment carbon cycle strongly influenced by CH_4 seepage. The ebullient CH_4 collected at The Hole has a carbon isotope composition of δ^{13}C of -71.0 ± 0.3‰ (Chowdhury et al., 2024).

4.3.2 Lipidomic Survey

Detected lipid biomarkers included archaeal sourced IPL, CL, and CL decay products (CL-DP) as well as photosynthetic plant pigments. Figure 4.3 provides the down core profile of measured lipids. Lipid quantification is presented as sediment normalized concentrations (μg·g sed^{-1}).

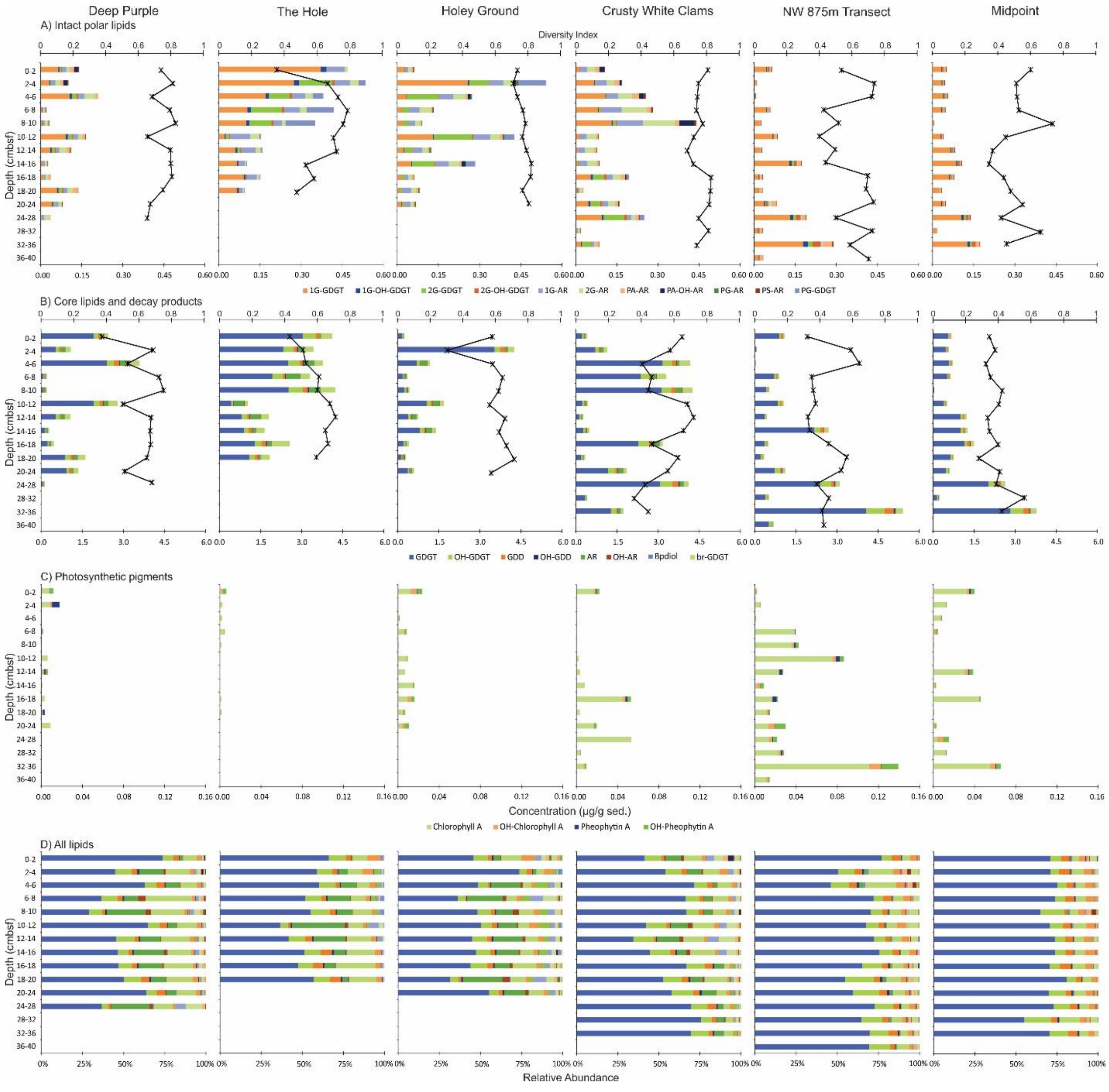

Figure 4.3: Lipidomic survey of site 2A-1 and transect. Data is presented as the A) Concentrations of IPLs, B) concentrations of core lipids and degradation products, C) water column sourced pigments, and finally as D) the relative abundance of all identified lipids at each core site. Downcore profiles of the Simpson's Diversity Index for the IPL community and the CL and CL-DP community are presented with their respective downcore lipid concentration profiles.

4.3.2.1 Archaeal Lipids

4.3.2.1.1 Intact Polar Lipids

Archaeal IPLs were tentatively identified by their LC elution patterns and mass spectral characteristics as previously reported in the literature (Appendix Table B3.1-3.6). The resolved lipidomes included both hexose- and phosphate-headgroups, with the former consistently found in higher relative abundance. Glycolipids included IPLs with monoglycosyl (1G) and diglycosyl (2G) head groups linked to either a C_{40} glycerol dialkyl glycerol tetraether (GDGT) or a C_{20} diphytanyl diether (archaeol; AR). Three phosphate-headgroups were identified in the samples set. Only phosphatidylglycerol (PG) was found linked to the GDGTs, but all 3 groups were found in association with AR.

The 1G-GDGTs include isoprenoidal core lipid with 0–4 cyclopentyl moieties (1G-GDGT-0 to -4) as well as 1G-GDGT-5 (crenarcheol), which contains four cyclopentyl and one cyclohexyl moiety. Summed, the 1G-GDGTs recorded a maximum concentration of 0.37 $\mu g \cdot g\ sed^{-1}$ to an average 0.0637 $\mu g \cdot g\ sed^{-1}$. In The Hole, these compounds systematically decreased downcore. The other seep samples do not closely follow this trend, but instead contain discrete intervals of increased 1G-GDGT abundance (Fig. 4.3). The two transect cores show an increase of 1G-GDGT abundance with depth. 2G-GDGT-0 to -2 were tentatively identified in each sample, but 2G-GDGTs (3-4) were more elusive, occurring in discrete sediment intervals. 2G-GDGT-5 has only been tentatively identified in the transect cores. The summed average of the 2G-GDGTs is low, measuring only 0.02 $\mu g \cdot g\ sed^{-1}$. The abundance of 2G-GDGT was markedly less than the 1G-GDGT class. The hydroxylated counterparts of the 1G- and 2G-GDGT were limited to 0–2 cyclopentyl moieties. The concentrations of the 1G- and 2G-OH-GDGTs each reached a maximum concentration of only 0.02 $\mu g \cdot g\ sed^{-1}$.

Monoglycosyl- and 2G-AR are relatively abundant within the seep, but their concentrations decrease drastically in the transect. In The Hole and Holey Ground, the concentrations decrease systematically with depth. Crusty White Clams experiences an increase in concentration up to a depth of 8 cm, followed by a systematic decrease. The average concentration 1G- and 2G-AR within the seep measure 0.03 and 0.02 µg·g sed^{-1}, respectively. No 2G-AR has been reported from the Midpoint Transect and concentrations on average in the transect for both head groups are less than 0.01 µg·g sed^{-1}.

Phospholipids degrade at a faster rate than glycolipids (Harvey et al., 1986; Schouten et al., 2010), which may account for their elusiveness in seep site 2A-1. The phospho-based head groups were tentatively identified in low concentrations (<0.05 µg·g sed^{-1}.). PG-GDGT was only identified in The Hole and in a few discrete intervals of Holey Ground and Crusty White Clams. Similarly, PG-AR was only identified in Holey Ground and Crusty White Clams. The other two headgroups, the phosphatidic acid (PA) and the phosphatidylserine (PS) were exclusively linked to AR and identified more consistently throughout the dataset. No phospholipid ARs were identified in The Hole, but these compounds were found throughout the other transect core samples with concentrations that decrease with sediment depth.

4.3.2.1.2 Core Lipids

The most abundant lipids within this study are the isoprenoidal GDGT core lipids. Similar to the 1G- and 2G-GDGTs, these isoprenoid core lipids contain 0–4 cyclopentyl moieties, as well as crenarchaeaol, GDGT-5, containing four cyclopentyl moieties and one cyclohexyl moiety, and the regional isomer of crenarchaeaol, GDGT-5′. The summed concentration of GDGTs ranged from 4.07 µg·g sed^{-1} to 0.02 µg·g sed^{-1} for an average 1.04 µg·g sed^{-1}. The hydroxylated versions of these compounds are also present in lower concentrations (avg. 0.15 µg·g sed^{-1}), and like their

1G- and 2G- precursors, only OH-GDGTs containing 0,1, and 2 cyclopentyl moieties are reported. Within the seep, both the GDGTs and OH-GDGTs experience a systematic decrease downcore, with the exception of Crusty White Clams. In the transect, these compound classes increase with depth.

A second core lipid, AR has been tentatively identified in the sample set. The structure of AR is a single glycerol ether bonded to two phytanyl chains. AR is more abundant than its 1G- and 2G-AR precursors, with an average concentration of 0.10 µg·g sed^{-1}. The concentration of AR decreases with depth within the seep and increases with depth within the transect.

4.3.2.1.3 Core Lipid Degradation Products

Glycerol dibiphytanol diethers (GDDs) lack a direct biological precursor but possess a similar structure to the GDGTs. With a structure of two biphytanyl chains bonded to a glycerol through two ether linkages, it has been proposed that these compounds represent partial GDGT degradation products (Liu et al., 2012b; Meador et al., 2014; Hingley et al., 2024) of GDGTs. The GDD-0 to -5 series is distinguished by an increasing number of cyclopentyl moieties. Within the seep, GDD concentrations are variable and do not present any systematic trends, but like the other previously mentioned core lipids, there is an increase with depth within the transect that reaches a maximum concentration of 0.34 µg·g sed^{-1}. Hydroxylated GDDs (OH-GDDs) containing 0, 1, and 2 cyclopentyl moieties were tentatively identified in trace amounts (avg. 0.01 µg·g sed^{-1}). Like the GDDs, no remarkable trend is present in seep samples, but transect samples exhibit an increase in concentration with depth.

Biphytanediols are the carbon skeletons of GDGTs and their IPL precursors and represent the latest stage of polar core lipid degradation (Schouten et al., 1998). These single chain structures posses 0–3 cyclopentyl moieties. These compounds were tentatively identified in most samples, albeit in low concentrations (avg. ≤0.01 µg·g sed^{-1}) that increased with sediment depth.

4.3.2.2 Eukaryotic Lipids

Photosynthetic pigments, chlorophyll *a* (Chl *a*) and pheophytin *a (*Phy *a)*, the breakdown product of Chl *a*, and their hydroxylated derivatives have been tentatively identified. Chl *a* is a fundamental pigment of many photosynthetic organisms, such as plants and algae and therefore represent euphotic zone allochthonous to the benthic sediments. All pigments recorded low concentrations, however, Chl *a* was the most abundant with an average concentration of 0.01 µg·g sed^{-1}. OH-chlorophyll *a* and OH-pheophytin *a* have been identified in very low concentrations (avg. <0.01 µg·g sed^{-1}). The concentrations of these pigments were higher in the ambient transect cores, and lowest within The Hole.

4.3.2.3 Mixed Source Lipids

Branched-GDGTs (*br*GDGTs) are non-isoprene core lipids that are distinguished based on their degree of methylation (increasing from four to six for *br*GDGT-I through *br*GDGT-III) and cyclization (with the range from zero to two cyclopentane moieties; a,b,c). In marine sediments *br*GDGT are primarily derived from the transportation of terrestrial materials but can also be produced in situ in anoxic marine water columns and sediments (Peterse et al., 2009; Liu et al., 2014; Z. Zhang et al., 2020). The biological sources of these compounds have yet to be fully resolved, although their origin is interpreted to likely be bacterial over archaeal (Damsté et al., 2000; Xiao et al., 2016). Within the seep transect *br*GDGTs are found in lower abundance than the GDGTs (avg. = 0.14 µg·g sed^{-1}).

4.3.3 Spatial Variation of Lipids

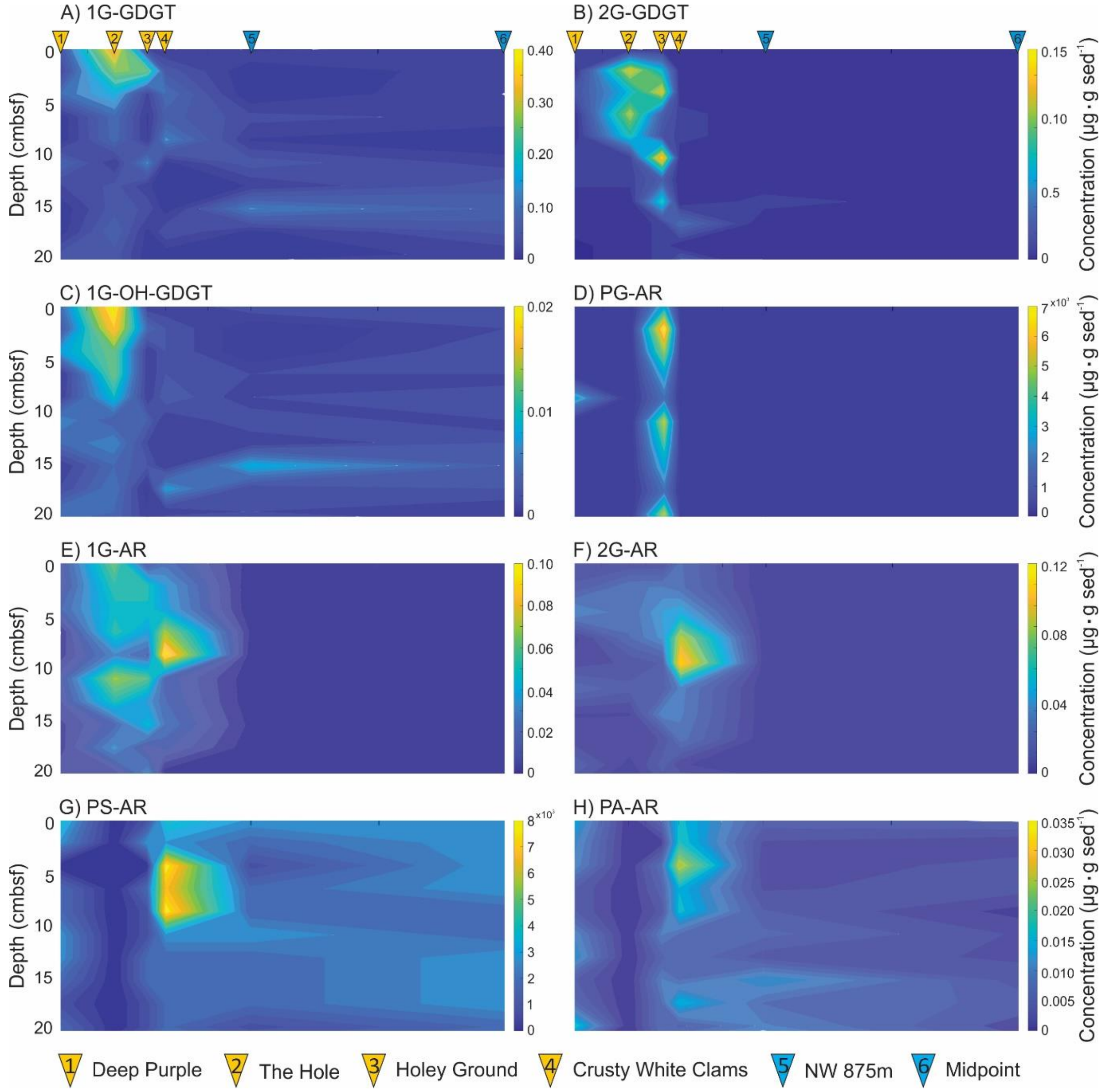

Figure 4.4: Lipid density heatmaps of Archaeal IPLs. Classes were chosen based on their availability through the data set or for their unique downcore profiles. Visualized communities are the A) 1G-GDGTs, B) 2G-GDGTs, C) 1G-OH-GDGTs, D) PG-ARs, E) 1G-ARs, F) 2G-ARs, G) PS-ARs, and H) PA-ARs.

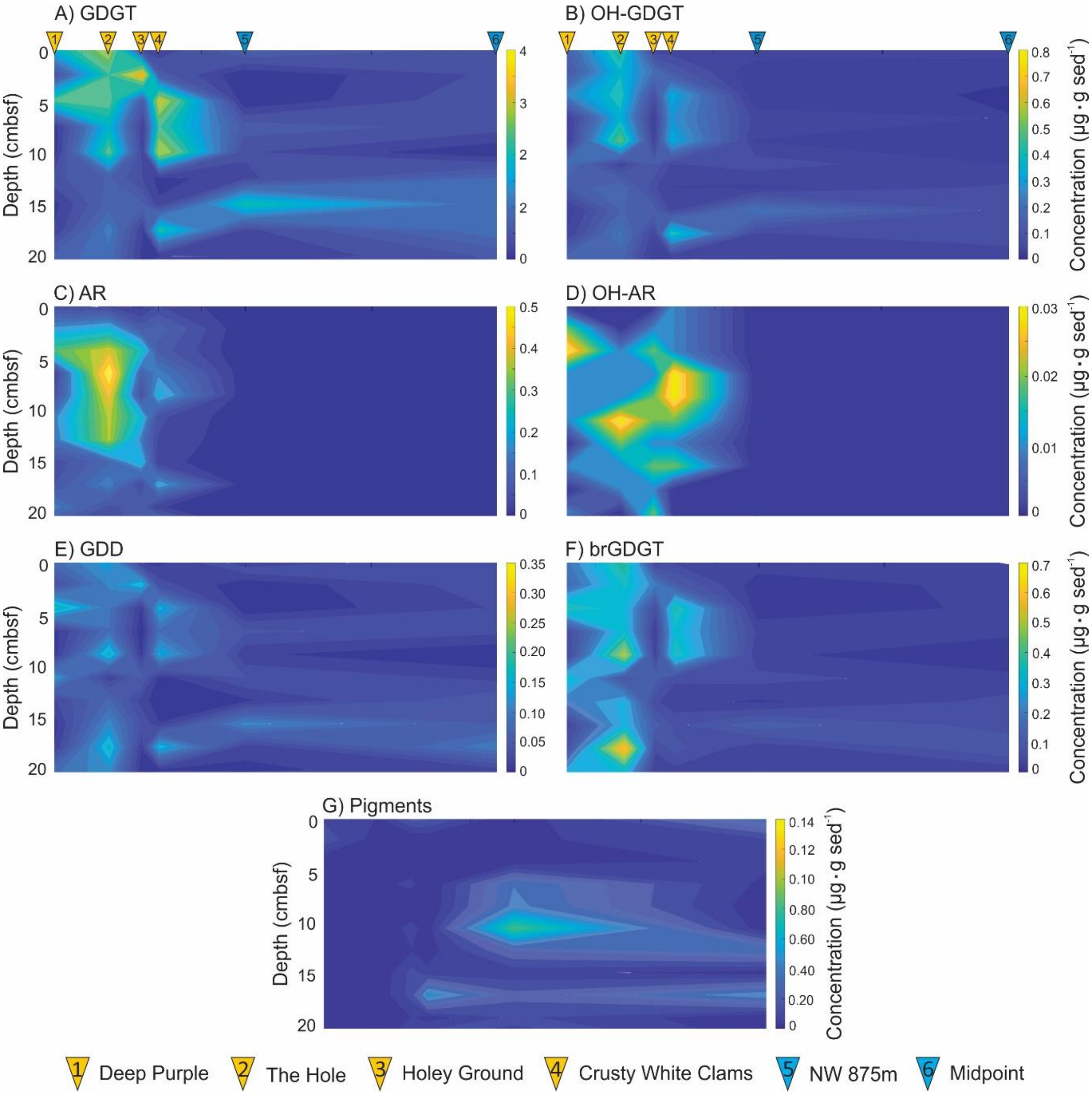

Figure 4.5: Lipid density heatmaps of selected CL communities. Archaeal CLs are the A) GDGTs, B) OH-GDGTs, C) ARs, D) OH-ARs, and E) GDDs. Mixed sourced lipids are the F) *br*GDGTs. The G) Pigments represent a Eukaryotic community.

The measured concentrations of tentatively identified lipid classes have been resolved as spatially discrete two-dimensional density heatmaps to display changes in community composition across the seep structure. The plots have been organized as a function of IPLs, CLs, CL-DPs, and photosynthetic pigments to contrast the proposed lived and fossilized microbial community (Figs.

4.4 and 4.5). Depth profiles on the heatmaps extends to a maximum depth of 20 cmbsf, resulting in a loss of the bottom of the transect cores. Excluding the pigments and the PS-AR and PA-AR communities, lipid density increases within the seep and decreases into the transect. Lipid classes as spatially constrained across the 2A-1 transect, presenting heterogeneous communities within individual cores.

4.3.4 Simpson's Diversity Index

Simpson's Index (Eq. 2; Simpson, 1949) measures community diversity by estimating the probability that two randomly selected individuals from a community will belong to the same species. Accordingly, diversity (D) is calculated based on the proportion of individuals (*p*) of a given species (*i*), with the proportion of individuals (Eq. 3) based on the number of individuals in the i^{th} species (n_i) and the total number of species within the data set (N). The results of the Simpson's Index are often expressed as the complement (1-D) that ranges from 0 to 1 (with 1 representing infinite diversity).

$$D = \sum_{i=1}^{S}(p_i)^2 \tag{2}$$

$$p_i = \frac{n_i}{N} \tag{3}$$

For this study, Simpson's index is applied in a modified form to enable an estimate of lipidome diversity by setting *p* as the proportion of lipids in the lipidome; n_i reassigned as the concentration of a lipid class and N being the total concentration of all lipid classes. The calculation was then applied to the full set of resolved lipid classes in the push core sediment (excluding upper water column sourced pigments) across the 2A-1 transect (Appendix Table B3.7).

The diversity of both IPL and CL lipidomes were independently calculated across the transect and reconstructed as diversity heatmaps (Figure 4.3). Heatmaps of lipid diversity where further produced to reveal two-dimensional community structure that can not otherwise be observed exclusively through relative abundance profiles of each core (Figure 4.6).

Index results followed expected trends in lipid diversity across an environmental gradient. IPL diversities were expectedly higher than that of CLs. Increased lipidomic diversity was also recorded across both of these groups for seep sediments. This significantly decreased moving out of the seep structure into the ambient sediments of the transect. Fluid seepage within the seep sediments is likely producing a richer ecosystem manifesting a more diverse lipidome. On average, IPL diversity is expectedly higher than CL diversity, due to the limited number of CL moieties that become shared across various head group classes.

The highest IPL diversity was observed in Deep Purple, Holey Ground, and Crusty White Clams. The lower diversity at The Hole is likely a result of limited phospholipid detection. Values were even lower for the two transect cores where not only limited phospholipids were detected, but also both 1G- and 2G-ARs. For CLs, the average diversity remained steady across Deep Purple, The Hole, and Holey Ground before steadily decreasing in Crusty White Clams and further in the transect. Heatmaps reveal heterogenous community structure within each core in both the IPL and CL communities.

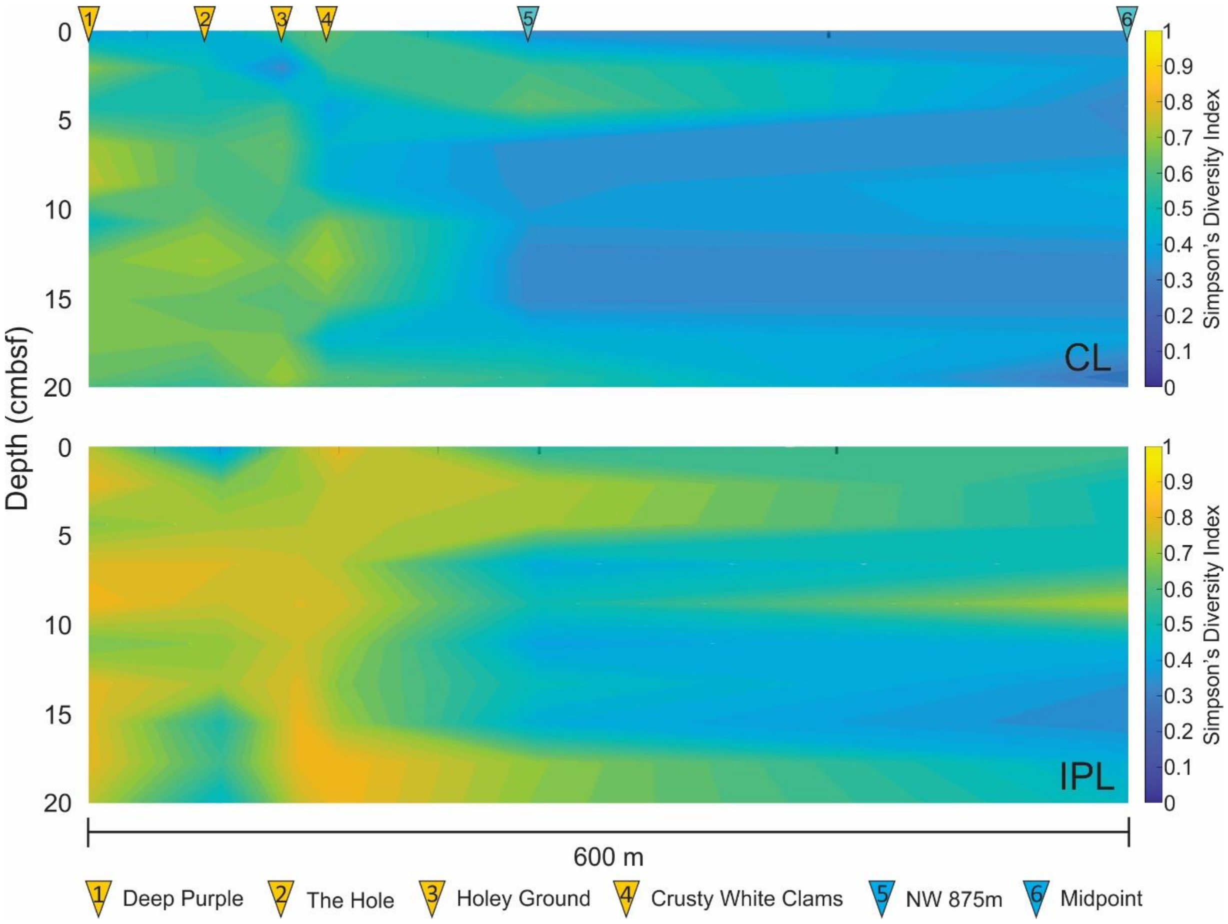

Figure 4.6: Heatmaps of IPL and CL Simpson's Diversity Index.

4.4. Discussion

4.4.1 Lipid Sources in the Marine Environment

The microbial lipidomic survey of Site 2A-1 focused primarily on archaeal lipids, specifically GDGTs and ARs and their respective IPL precursors and decay products. GDGTs are ubiquitous in marine sediments and are predominantly sourced from ammonia-oxidizing *Thaumarchaeota* in the sub-photic zone of the water column (Schouten et al., 2000; Lincoln et al., 2014; Pearson et al., 2016) prior to their deposition on the seabed. In-situ production of GDGTs has been proposed by Lipp et al., (2008) and a subsequent study by Lipp & Hinrichs, (2009).

Growth temperatures control the relative amount of ring structures in the GDGTs (Schouten et al., 2002). In cultivated archaea, GDGT-0 is the most commonly occurring GDGT, occurring in all major groups of Archaea. In environments where GDGTs 1-4 dominate in concentration over crenarchaeol, methanotrophic archaea of ANME-1 are believed to be an important source of GDGTs 1-4. Crenarchaeaol is treated as the biomarker of ammonia-oxidizing Thaumarchaeota (De La Torre et al., 2008; Pitcher et al., 2011). GDDs, based on their structure and distribution, are treated as a decay product of GDGTs (Liu et al., 2012b), although (Meador et al., 2014) did detect an IPL-GDD within an archaeal culture, suggesting a biosynthetic origin. Various members of Euryarchaeota, Crenarchaeota, and Thaumarchaeota synthesize AR (Koga et al., 1993). The relative contribution of these two targeted lipid classes can be used to decode the lipid community structure and provide insights to environmental conditions. The ANME-1 dominated communities contain GDGTs with glycosidic and phosphoglycerol head groups and whereas ANME-2, and -3 dominated communities contain AR based IPLs (Blumenberg et al., 2004; Rossel et al., 2008, 2011).

4.4.2 Archaeal Lipid Decay Pathways

It is expected that biomolecules will become progressively changed as they pass from being apart of living organisms into progressively more buried layers of sedimentary organic matter. Fundamental to this change is the expected hydrolysis of an IPL's polar head group to yield a CL, which is later followed by the loss of π-bonds and functional groups and eventually the breakdown of the CL structure to yield a pure hydrocarbon biomarker (White et al., 1997). While the pathway of this process is believed to be well resolved, the timing to which each step happens is not constrained. Here we shed light on the process by comparing the process of change following a single upper water column sourced lipid.

Crenarchaeol (GDGT-5), is a five ringed GDGT containing four cyclopentyl and 1 hexose ring. The compound is largely considered to be a biomarker for chemoautotrophic, ammonia oxidizing Thaumarchaeota largely inhabiting the sub-photic zone (~200 to 500 mbsl) of the water column (Schouten et al., 2000; Pearson et al., 2016). Thus far, no evidence of in situ IPL crenarchaeal production has been reported for marine sediments. Instead, $\delta^{13}C$ compositions support production through lipid recycling pathways (Zhu et al., 2021). The lack of *de novo* production in marine sediments therefore makes crenarchaeal ideal for tracking lipidomic decay pathways. Intact polar lipid crenarchaeol can be found in marine sediments with both glycosidic- or phosphate-based headgroups. Only the 1G headgroup was consistently identified throughout the sample set used in this study. Additionally, the crenarchaeol five ring structure is also found in a modified CL referred to as GDD-5, which lacks the second glycerol moiety found in GDGT-5. The source of GDDs in the marine environment remains a topic of continued study. Meador et al. (2014) found monoglycosidic- and diglycosidic-GDDs in culture samples, but IPL-GDDs have yet to be identified from environmental samples. This is consistent with findings from other recent work focusing on sedimentological relationships which indicate that GDDs are largely early-stage degradation products (Liu et al., 2012b; Hingley et al., 2024).

The downcore variations in concentration can therefore be interpretated as an indication of productivity through time, with higher concentrations corresponding to higher periods of microbial productivity. Additionally, upon deposition at the seabed, the concentrations of IPL-Cren (1G-GDGT-5) should systematically decrease giving rise to an equal increase in Cren (GDGT-5) and CL-DP-Cren (GDD-5) from diagenetic changes that accompany the ~10,000 yr burial history.

To track these changes, the relative proportions of 1G-GDGT-5, GDGT-5, and GDD-5 were measured as down core profiles for all sediment samples of the transect survey (Fig. 4.7). For these three compounds, the down core profiles show large shifts with sediment depth that is unique to each core. However, for the most part, the relative abundance of the three compounds remains the same. In fact, at any given depth across the transect the relationship can be describe using an average ratio of 5:85:10 (Appendix Table B4.1). The lack of systematic divergence, coupled with the general understanding that there is no in situ production of crenarchaeol, indicates systematic down-core degradation trends are not operating on this lipid class with continued burial.

Productivity is not a satisfactory explanation for the profiles observed at site 2A-1, in fact, the downcore profiles observed at Site 2A-1 support a more recent line of question into the origins and rate of IPL-GDGT degradation in marine sediments. The turnover rates of IPL-GDGTs in marine sediments have been modeled to reach up to tens of thousands of years (Schouten et al., 2010; Lin et al., 2013; Xie et al., 2013). This result has called into question the application of using glycosidic-GDGTs as living biomarkers. A lack of systematic change in the GDD profile also supports a biosynthetic origin proposed by (Meador et al., 2014). For this study, the sediment reaches a maximum depth of 40 cm, which based on ^{14}C measurements, has an age of 10343 ^{14}C yr BP ± 31 (Appendix B2). At this age, some level of degradation is expected, but is not observed within the data.

Cross plots of 1G-GDGT-5 and GDD-5 versus GDGT-5 are displayed in Figure 4.7 to further investigate relationships between the three classes and potentially provide insights into lipid sourcing. The concentration of GDGT-5 is a magnitude higher than 1G-GDGT-5 and GDD-5, suggesting that distribution plotting with a ratio of 1:10 would describe a perfect decay pathway. A 1:10 ratio assumes that 100% of the CL or DP-CL, GDGT-5 and GDD-5, respectively, is produced by the IPL or CL precursor. This proposed relationship is most closely observed in NW 875 m and Midpoint, where microbial activity is lower, increasing preservation. The four cores from the seep present more complex relationships. Across all cores, degradation products are more closely related to GDGT-5. This observation may be an effect of the multiple headgroups crenarchaeol can posses as an IPL, whereas the GDGT-5 would decay directly to GDD-5. The strong correlation between CL and CL-DP indicates that GDD-5 is predominantly a degradation product of GDGT-5. These observations coincide with recent findings from Hingley et al., (2024) which concluded that GDDs occur primarily as degradation products of GDGTs, as opposed to a biosynthetic origin.

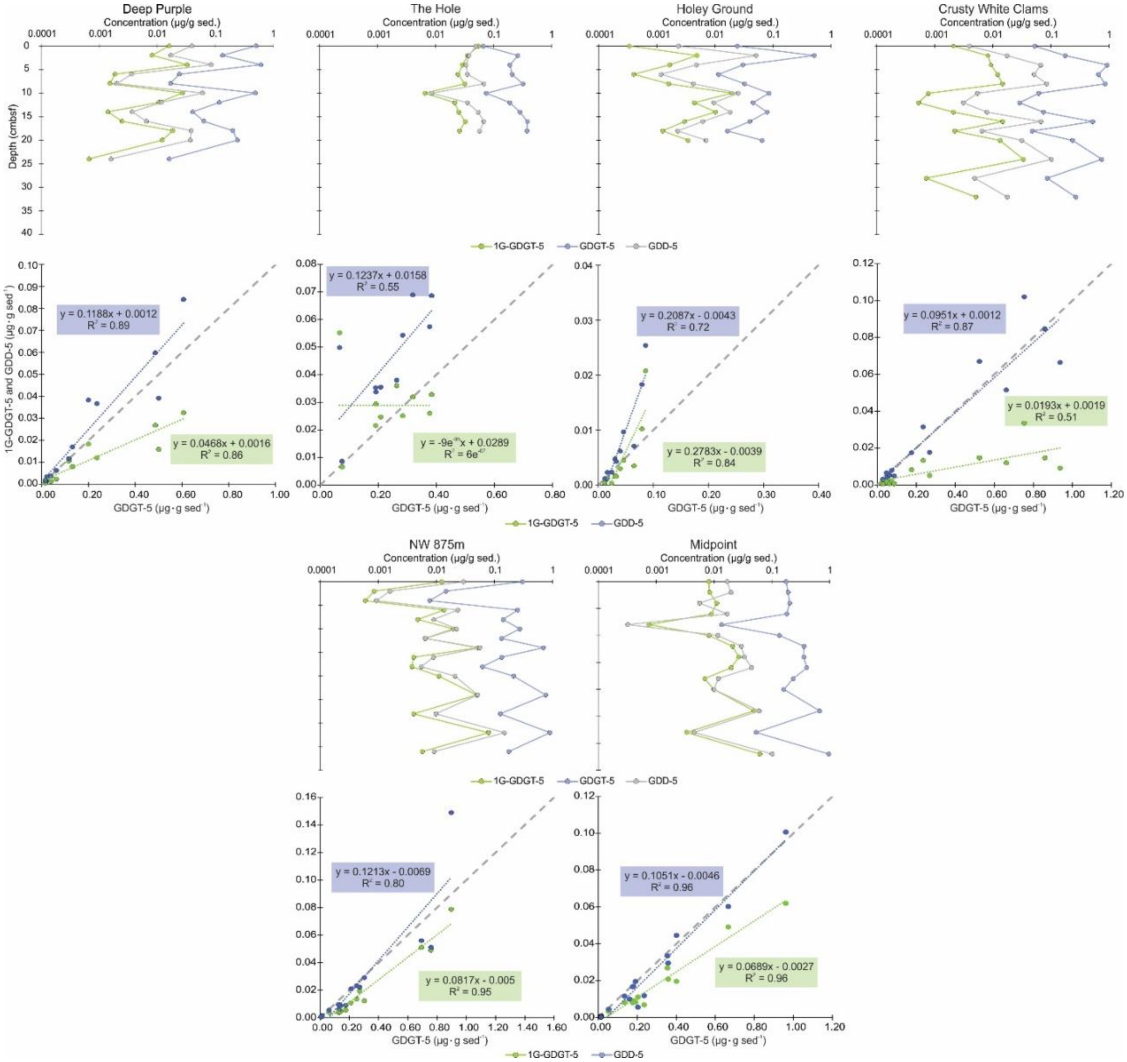

Figure 4.7: A) Downcore profiles of crenarchaeol in life conditions as an IPL along side two diagenetic decay stages (as the CL GDGT-5 and the CL-DP GDD-5). Concentrations are displayed on a logarithmic scale to better identify the correlated downcore trends. B) Cross-plots of GDD-5 and 1G-GDGT-5 concentrations versus GDGT-5. The dashed grey line represents a 1:10 ratio.

4.4.3 Principal Component Analysis

The distribution of membrane lipids from site 2A-1 were further examined by PCA (Fig. 4.8a). The scree plot revealed that the first four principal components explained 74.5% of the total variance (Appendix Figure B5.1). All but two lipid classes had positive loading on the PC 1, with the strongest loadings belonging to GDGTs and GDDs, including CL and 1G-IPLs. The PC 2 accounted for 21.2% of the total sample variance.

The first component appears to be separating lipid classes based on concentration. The GDGTs have the largest positive loading and are found ubiquitously throughout the marine environment and occur in the highest concentration. Other GDGT classes, including IPL-, OH-, and br-GDGTs are also found in relatively high concentrations within the samples and have a high positive loading on PC 1. Archaeol species are more likely to be soured in-situ from the seep environment, as they are used as ANME biomarkers for indications of AOM activity. Depending on AR species, these lipids have a moderately positive to slightly positive loading on PC 1. The pigments are exclusively sourced from the upper water column and were found in small concentration in the transect. Pigments have a slight positive loading on PC 1, with Pheo having a slight negative loading.

The second component marks a distinction between ambient and seep environments. Pigments have a negative loading on PC 2, which aligns with the transect samples. The GDGTs do not have any loading along the second component but they're found ubiquitously in marine sediment, regardless of environment. AR lipid classes were more prominent in the seep samples, and no IPL-ARs were identified in the transect. Lipid classes found either exclusively or predominantly in the seep have a positive loading on PC 2.

Samples are also distributed along the first component based on their lipid content. Those with a high TLE have positive loadings on PC 1 and samples with very low TLE values have a negative loading. PCA also revels clear differences between samples from the seep and the transect based on their distribution along PC 2. This is largely controlled by the availability of AR species in the seep samples which are not present in the ambient sites, and the preservation of pigments in the ambient sites. PCA of the full lipidomic survey, separating lipid species by their ring structure, reveals separation along PC 2 in classes such as the GDGTs which have no loading when observed as a whole (Appendix Fig. B.3).

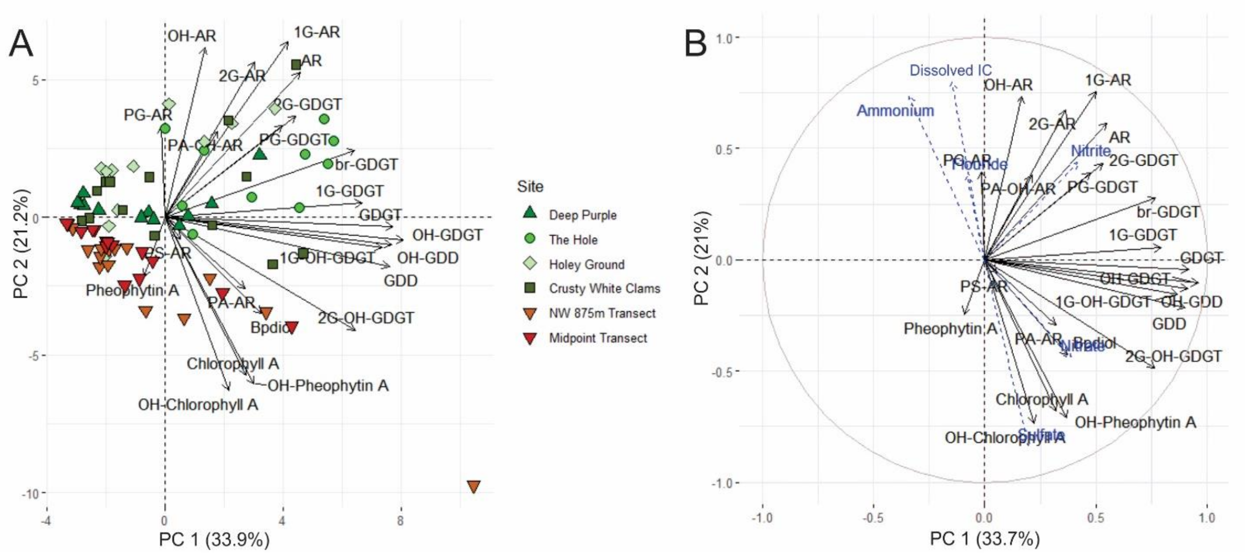

Figure 4.8: A) PCA biplot of lipid classes and samples at site 2A-1. B) Combined PCA analysis of seep site 2A-1 lipid classes and porewater ions. The porewater ions concentrations is treated as a supplementary variable to the lipid concentrations.

Results from the porewater PCA from Chapter 2, Section 4.1 distinguished ambient and seep sites based on the site geochemistry. A combined porewater and lipidomic PCA relates lipid classes to their respective geochemical environments (Fig. 4.8b). By treating the porewater ion concentrations as supplementary variables, when added to the lipidomic PCA, ions with the highest concentration at depth within the seep have high positive loadings on PC 2. Lipid classes with high positive loadings along the second component and indicative of a seep environment. Similarly, ions with high concentrations at depth in the transect have negative loadings on PC 2. The pigments and SO_4^{2-} plot close together in this analysis. Ions with minimal changes between seep and ambient sites have both moderate positive and negative loadings on PC 2, and plot closely to the GDGTs and more ubiquitous lipids species.

4.4.4 Microbial Community Reconstruction

4.4.4.1 The Methane Index

The methane index (MI) (Eq. 4) was introduced as a GDGT-based molecular indicator that can detect destabilization of marine gas hydrates (Y. Zhang et al., 2011) or other methane impacted sediments by comparing the relative proportion of two end-member GDGT sources (lipids sourced from methanotrophic ANMEs that belong to the phylum of Euryarchaeota with those that derive from planktonic Thaumarchaeota) (Y. Zhang et al., 2011; Kim & Zhang, 2023). Accordingly, in methane-rich environments, GDGT-1, -2, and -3, predominantly produced by ANME-1 (Blumenberg et al., 2004), become synthesized in larger quantities than the planktonic Thaumarchaeota lipids GDGT-0, -4, and crenarchaeol. As such, the MI qualitatively distinguishes methane impacted sediments from normal marine sediments with values that can range from 0–1 (>0.3 generally being accepted as indicative of methane having been present in the depositional environment). Based on this premise, MI is now used as a qualitative, paleo-indicator of AOM.

$$MI = \frac{[GDGT-1]+[GDGT-2]+[GDGT-3]}{[GDGT-1]+[GDGT-2]+[GDGT-3]+[GDGT-5]+[GDGT-5']} \quad (4)$$

For seep site 2A-1, higher abundances of AMNE-1 based lipids relative to planktonic Thaumarchaeota is supported by the PCA results. When analysed as a whole, the GDGTs have no loading along PC 2. When divided by individual ring structures, the classes separate along PC 2, with GDGT-1, -2 and -3 experiencing positive loadings and negative loadings are observed for

GDGT-5 and -5′ (Appendix Fig. B5.3). Positive loadings along PC 2 appear to correspond to seep related lipids and in situ production, while negative loadings relate to lipids sourced from the water column.

Methane index values closely match porewater gradient seepage trends (Fig. 4.8a). By reconstructing downcore profiles across the seep transect as a heat map, it is apparent where the seep centre is located and the extent of the methane impact (Fig. 4.10a). MI values for the seep are high with an average value of 0.6 (Appendix Table B6.1). The Hole has a MI value of 0.95 at the surface (the highest calculated MI value of within the seep site), that decreases to 0.25 by 20 cmbsf. The transect has an MI of only 0.26, indicating that these sediments have not been exposed to methane and reflect normal marine conditions.

Since IPLs are considered products of living or recently deceased organisms (Sturt et al., 2004), the concentrations of IPL-GDGTs can therefor be used in the MI to indicate methane seepage activity within the modern microbial community. Due to low concentrations and limited availability of the phospho-based and the 2G- headgroups, only concentrations of 1G-GDGT were used for this calculation. This new model increases the range of methane presence within the seep (Fig. 4.10b). Whereas the MI for Deep Purple and The Hole appears to be unchanged between the two models, the MI values for Holey Ground and Crusty White Clams notably increased. Holey Ground has a surface MI of 0.98, the highest $\mathrm{IPL_{MI}}$ and even higher than the $\mathrm{CL_{MI}}$ at The Hole. The $\mathrm{IPL_{MI}}$ is also lower in the transect cores than the $\mathrm{CL_{MI}}$. High MI values at Holey Ground and The Hole are coupled with depleted $\delta^{13}C_{TOC}$ values, which are similar to the isotopic signature of biogenic methane (Whiticar, 1999; Joye, 2020). Geochemical analyses thus far indicate true ambient conditions in Midpoint, the furthest point on the seep transect. The $\delta^{13}C_{TOC}$ values (avg. = -22.00 ‰) at this location represent normal marine conditions ($\delta^{13}C_{TOC}$ = -21 ‰; Meyers, 1994).

4.4.3.1.1 MI_{IPL} versus MI_{CL}

Later applications have seen IPLs with the index's CL GDGT configurations used as a modified MI_{IPL} proxy (T. Zhang et al., 2023; Kim & Zhang, 2023). High values (>0.5) for the MI_{CL} and MI_{IPL} indicate that AMNE-1 AOM activity has been sustained over a long period of time and is likely still active within the seep. Treating the MI_{IPL} as an indication of modern seepage, any changes observed between the MI_{CL} and the MI_{IPL} mark shifts in the site's seepage history. A high MI_{CL} coupled with a high MI_{IPL} indicate sustained active seepage, while high MI_{CL} and low MI_{IPL} would indicate a paleo-seep. A cross plot of the MI for Scotian Slope cold seeps, including the six cores from Site 2A-1 has been supplied by Umoh et al., (in prep).

While Chapter 3 established that the correlation between SO_4^{2-} and DIC can qualitatively identify a diffusion limited system and determine systems alkalinity, the MI correlations can be used to qualitatively determine the age of seepage (Fig. 4.9). This cross plot provides an alternative visualization method for two data sets that compare the living and fossil components of the same seep system. Deep Purple and Holey Ground plot exclusively in the zone of sustained seepage with Deep purple plotting near the centre and Holey Group near the upper end of the range. Moving up the sustained seepage zone to higher MI values indicates an increase in AOM activity. The cross plot shows the subtle shift in the MI heatmaps which includes elevated values of MI_{IPL} in Crusty White Clams and potential paleo-seepage in The Hole. This shift could indicate a change in CH_4 seepage pathways, not yet observed at the seafloor. NW 875m and Midpoint both plot at the border of sustained seepage and no seepage, further proof of their ambient nature.

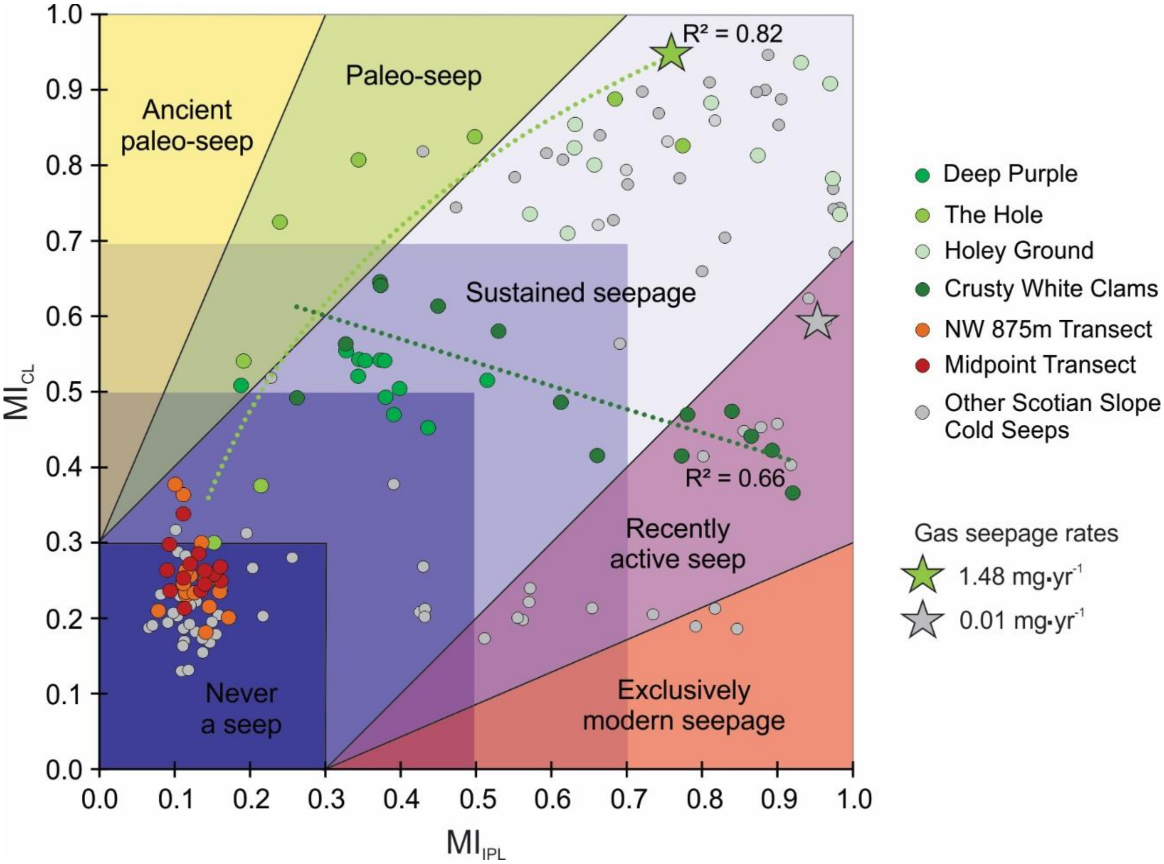

Figure 4.9: Cross plot of the MI_{IPL} and MI_{CL}. Seepage zones were constructed using MI values of 0.3 and 0.7, which denote no AOM activity and extremely high activity. The colour gradient has been used to mark increases in AOM activity, moving up towards higher MI values. Other Scotian Slope samples provided by Umoh et al. (in prep). Gas seepage rates for selected sites are reported in Chowdhury et al. (2024).

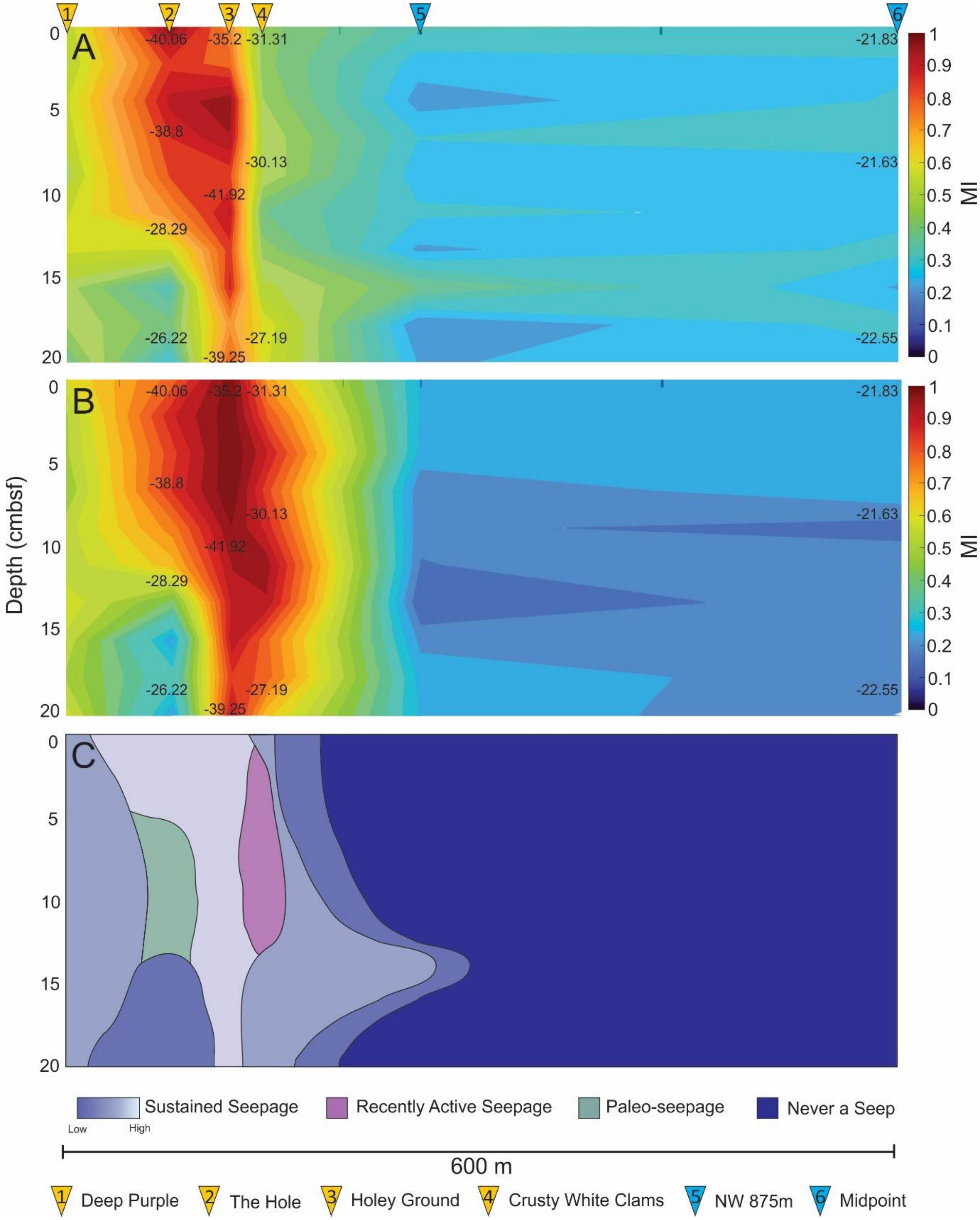

Figure 4.10: Heatmaps of A) MI_{CL}, B) MI_{IPL}, and C) a reconstruction of the inferred seepage zones based on Figure 3.7. Values on MI_{CL} and MI_{IPL} are $\delta^{13}C_{TOC}$ measurements.

4.4.4.2 Branched GDGTs

Branched and cyclic, non-isoprenoidal GDGTs, collectively referred to as branched GDGTs (*br*GDGTs), are traditionally considered to be derived from soil microbes (Hopmans et al., 2004) and therefore mark allochthonous carbon input into marine basin sediments. However, more recently, in situ production of *br*GDGTs in marine systems was identified by distinct changes in the *br*GDGT distribution with varying rates of AOM activity (Zhang et al., 2020). Concentrations of *br*GDGT-Ia, -IIa (Zhang et al., 2020) and -IIb (Zhang et al., 2024) were significantly influenced by increased rates of AOM in cold seep systems. 16S rRNA genes revealed a high correlation of *br*GDGT-Ia, -IIa, and -IIb with sulfate reducing bacterial groups, particularly those associated with AOM (Zhang et al., 2024). Following similar logistics used by Zhang et al. (2011) to create the MI, here we consider a new proxy referred to as the Branched Sulfate Reduction Index, *br*SRI (Eq. 5) for identifying zones MSR within seep environments.

$$brSRI = \frac{[brGDGT-Ia\ ]+[brGDGT-IIa]+[brGDGT-IIb]}{[\sum brGDGT-Ia,b,c]+[\sum brGDGT-IIa,b,c]+[\sum brGDGT-IIIa,b,c]} \qquad (5)$$

For this index, active MSR is implied with *br*SRI >0.5, the median of the index. Values greater than 0.7 can be used to describe an extremely actively community, likely in a location where MSR is the dominant metabolic reaction. On the opposite side of the index, values below 0.5 still indicate the presence of sulfate reducers, however the community is likely not active. This is the case in more ambient sediment conditions where sulfate is able to penetrate into the sediments at a much greater depth with no impetus for high rates of reduction.

In order to understand the results described in Figure 4.11, the MI must also be considered as ANME and SRB are competing communities belonging to two distinct metabolisms that only directly interact within the SMTZ. The highest MI is reported in Holey Ground, where consequently, lower values of the *br*SRI are reported for the seep cores. This indicates the dominance of methane oxidation and the ANME community within this core. In Deep Purple, where MI values indicate moderate levels of ANME activity (MI = ~ 0.5), the *br*SRI is higher. Both communities are actively competing in this environment. When both parameters are conjoined, the results suggest that CH_4 seepage alters the dominance of microbial activity, such that MSR as a metabolism is more dominant of the seep periphery but is out competed at the seep centre by ANME. Furthermore, Figure 4.11B reveals a positive correlation (R2=0.51) between *br*SRI values and the percent loss of SO_4^{2-} in the sediment porewater. Interestingly, the PLS regression line has a y-intercept that is close to the inferred initiation point of 0.5 for the *br*SRI inferred activation point and a final rise of the slope to the total SO_4^{2-} loss at ~0.7 brSRI.

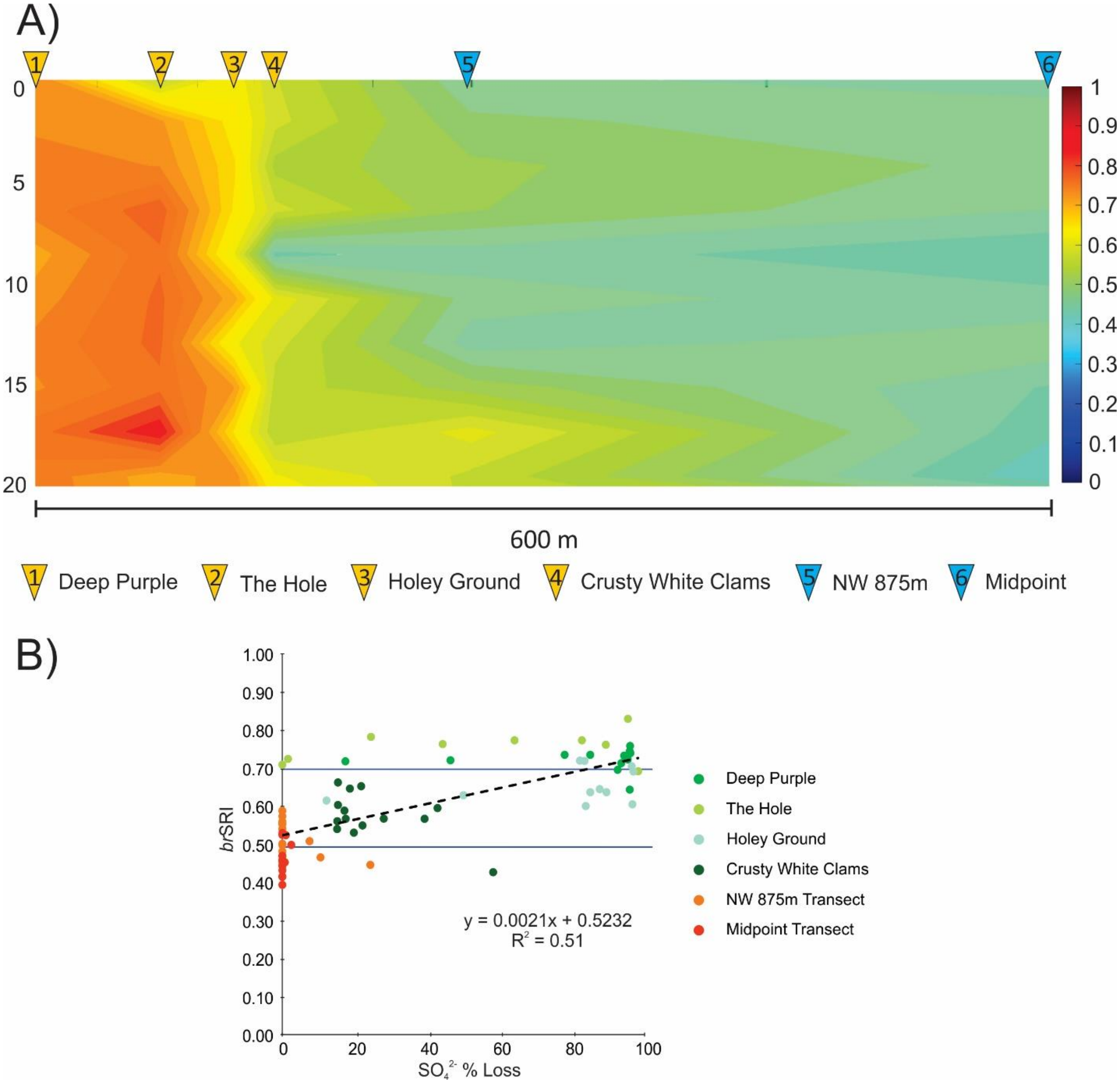

Figure 4.11: A) *br*SRI heatmap of site 2A-1. B) Cross plot of SO_4^{2-} lost vs *br*SRI. Sulfate loss is calculated as the difference between normal marine conditions of SO_4^{2-} and measured SO_4^{2-} concentrations. Horizontal lines a 0.5 and 0.7 *br*SRI approximately corresponds to the y-intercept where SO_4^{2-} loss in the transect samples begins and the maximum mean peak average loss, respectively.

4.4.4.3 ANME Community

Archaeol and OH-AR with highly depleted carbon isotope compositions are biomarkers of methane oxidation under anaerobic conditions (Hinrichs et al., 1999; Elvert et al., 2000). While individual carbon isotope compositions of lipid biomarkers are unavailable for this study, the highly depleted $^{13}\delta C_{TOC}$ values within the seep sediments in comparison to values from the ambient sediment indicates a contribution from ^{13}C depleted lipids to the organic carbon pool.

The ratio of OH-AR:AR can be used to differentiate the ANME community present. It is generally accepted that values below 0.8 indicate an ANME-1 dominated community. The ratio calculated at Site 2A-1 was extremely low (avg. = 0.11, sd = 0.11) suggesting that the seep is dominated by an ANME-1 type community (Appendix Table B6.1). No OH-AR was identified in the transect, therefor the ratio could not be calculated for these samples. High MI values (>0.3) further support observations of an ANME-1 community. ANME-2 type communities are not capable of synthesizing internally cyclized GDGTs and instead favour production of OH-AR (Blumenberg et al., 2004).

ANME-1 has been observed to occur as single cells or in short chains. Unlike ANME-2 and -3 type communities, ANME-1 is only loosely associated with its bacterial partner (Knittel & Boetius, 2009). This has led to some speculation that single-cell ANME-1 communities may couple AOM to sulfate reduction without a bacterial partner (Orphan et al., 2002; Knittel et al., 2005). ANME-1 type communities produce have been found to dominate microbial mat environments, like the black sea (Knittel et al., 2005). The dominance of an ANME-1 type community, coupled with the moderate increase of SRB related *br*GDGTs within the seep, supports previous observations of the ability of ANME-1 to couple AOM to sulfate reduction on its own.

4.4.5 Microbial Seep Architecture

The microbial seep architecture was reconstructed using ion concentration heat maps and lipid class density heat maps generated to identify communities and geochemical reactions of interest. Generated heatmaps assume continuous geochemical conditions between sample sites.

This is a modified interpretation of the true seep environment, due to the presence of cold seep carbonates which are not revealed in this model. Carbonates divert porewater flow pathways, which would create fine scale changes in the geochemical zonation described (Solomon et al., 2008; Rooze et al., 2020). Carbonate formation relies on the presence of Ca^{2+} and Mg^{2+} ions. While these ions were not measured a site 2A-1, the existence of cold seep carbonates points to their availability within the sediment. Free Mn^{2+} and Fe^{2+} ions also have the capacity to react with CO_3^{2-} to form cold seep carbonates.

Interpretations of geochemical zones created through porewater ions have been described in detail in Chapter 3, section 4.4 (Fig. 4.12a). Nitrite and NO_3^- ion concentration revealed a shallow nitrogen cycle, likely denitrification, within the seep sediments that tapered out moving into more ambient conditions Below denitrification, a halo of SO_4^{2-} reduction surrounds the interpreted SCI. The SO_4^{2-} reduction zone extends out into the ambient sediments, although the rection is not occurring at the same magnitude due to the lack of fluid seepage (Borowski et al., 1996). The sulfate dissolved inorganic carbon transition zone (SDICTZ) has been tentatively interpreted as the zone in which both DIC and SO_4^{2-} concentrations exist in a 1:1 ratio as described in Chapter 3, section 4.2. Increased DIC concentration sit below the SDICTZ in the deep seep sediments (>10 cmbsf). Chowdhury et al., (2024) only detected small amounts of CO_2 (<10% of total hydrocarbon gasses) within site 2A-1. Methanogenesis is therefor acting as a stand-alone metabolism to CH_4 oxidation, leaving DIC as a biomarker of methanogenic activity. An interpretated SMTZ has been plotted at the bottom of the seep sediments, in areas of near complete SO_4^{2-} depletion.

The CL-MI was used to identify the extent and magnitude of AOM activity. The majority of the seep sediments had MI values consistent with AOM activity (MI >0.5) (Fig. 4.12b), so to highlight extremely elevated levels within the seep centre only MI values of 0.7 were plotted in the full seep interpretation (Fig. 4.12c). These extremely high values occurred exclusively in The Hole and Holey Ground. As previously noted, these values coincided with the most depleted $^{13}\delta C_{TOC}$ values. This supports evidence of a dominant ANME-1 type community. An ANME-1 type community coupled with low concentrations of alternative electron acceptors, discourages the presence of nitrogen- and metal-AOM.

Changes in the SO_4^{2-} gradient were used to map the geochemically defined boundary of the seep (Fig. 4.12a). Crusty White Clams presents a unique downcore profile, where increased concentrations of both SO_4^{2-} and DIC between 4 and 10 cmbsf correspond to increased concentrations of most lipid classes (Fig. 4.3). Increased microbial activity, coupled with promising geochemical conditions, supports the interpretation of the SMTZ.

The presence of microbial mats and elevated concentrations of NO_3^- and NO_2^- indicate that the nitrogen cycle is active in the shallowest sediment layers. The abundance of NO_3^- and NO_2^- relative to NH_4^+ in the shallowest sediment intervals points to denitrification as the dominant process acting in this depth (Chapter 3, Figure 3.2). Extending into the sediment profile, concentrations of nitrogen species ions vary with depth, obscuring a dominant metabolic signal.

Archaea are responsible for a significant amount of ammonia oxidation (Francis et al., 2005; Könneke et al., 2005). Originally, bacteria were thought to be solely responsible for nitrification in the marine environment. The first observation of nitrification in archaea was recorded by Könneke et al., (2005). Since this discovery, it has been found that AOA are responsible for the first-rate limiting step of nitrification. This revelation highlighted the importance of AOA in the biogeochemical cycling of nitrogen. Archaeal biomarkers for AOA are less distinct than markers for other metabolic processes. Crenarchaeol, despite being ubiquitously present across most marine systems, is considered the diagnostic biomarker AOA (De La Torre et al., 2008). AOA are capable of synthesizing the full suite of non-source specific GDGTs, leading researchers to use these biomarkers as a means of palaeothermometry reconstruction (Schouten et al., 2002; Rush & Sinninghe Damsté, 2017). Interestingly, the distribution of 1G-OH-GDGTs corresponds to the denitrification zone identified by the porewater profiles. 1G-OH-GDGTs are synthesized by Thaumarchaeota, the producers of AOA, which may lend to their usage as nitrogen cycle biomarkers when porewater profiles are available. Most lipid biomarkers associated with the nitrogen cycle are produced by Bacteria (Rush & Sinninghe Damsté, 2017). The lack of bacterial lipid biomarkers measured in this study limits the understanding of the nitrogen cycle occurring at site 2A-1.

Moving out of the seep, the lipid community structure changes in the ambient transect sediments. Based on SO_4^{2-} profiles, these sediment cores host more oxic sediments, not experiencing the same steep redox gradient as within the seep. Community composition throughout the seep is dominated by GDGTs, but the relative abundance between the seep and transect varies by almost 25%, highlighting the diverse communities within the seep sediments (Fig. 4.3). Simpson's Index calculations also demonstrate increased lipidomic diversity within the seep. The oxic conditions of the transect sediments create a zone of increased preservation in which PS- and PA- headgroups persisted, where they were lost in seep sediments. Similarly, most pigments were not preserved within the seep.

Photosynthetic pigments are a ubiquitous component of organic matter in marine sediments and may be used as an indicator of organic mater decay (Woulds & Cowie, 2009). Pigments can be used to identify organic mater sources and history, as well as model bioturbation over short timescales (Boon & Duineveld, 1998; Sun & Dai, 2005). Chl *a* is the most abundant pigment component in phytoplankton species. Specific pigment decay product ratios with Chl *a* can further provide insights to grazing patterns (Ingalls et al., 2000; Woulds & Cowie, 2009).

The degradation of Chl *a* has been proven to be largely controlled by sedimentary redox conditions, as well as bioturbation and biological mixing (Bianchi et al., 2000; Ingalls et al., 2000; Sun & Dai, 2005). Pigment decay is accelerated in zones of high redox gradients or where redox oscillations may occur (Sun et al., 1993; Ingalls et al., 2000). Seep sediments have high redox gradients, as previously expressed by the compressed sulfate profiles, and have microbial mats and bivalves present at the seafloor, resulting in low pigment concentrations within these cores. The Hole is almost completely devoid of pigments, and those present are in trace concentrations. Cold seep macrofaunal communities contribute to biological mixing, Preservation increases into the transect, where microbial activity is lower, decreasing the risk of grazing and heterotrophy. Higher organic matter preservation in the transect supports increased pigment concentration.

Based on a sedimentation rate of 0.004 $cm \cdot yr^{-1}$, this complex geochemical architecture of the top 20 cmbsf of Site 2A-1 has been forming over the past 5200 years (Fig. 4.2a). Methane seepage has formed strong porewater redox gradients in the seep sediments, which are supported by the microbial communities hosted within. The incorporation of depleted $\delta^{13}C$ into the sedimentary organic matter provides evidence of reduced fluid seepage and shallow carbon cycling at the sediment-water interface. Lipid biomarker proxies of the IPL and CL communities reveal how the microbial community structure and diversity have changed as a function of seepage over the seep's history. These findings highlight the dynamic interactions between reduced fluid seepage and microbial activity in shaping the geochemical environment at Site 2A-1, demonstrating how long-term seepage spatially influences biogeochemical cycling and microbial community evolution at cold seeps.

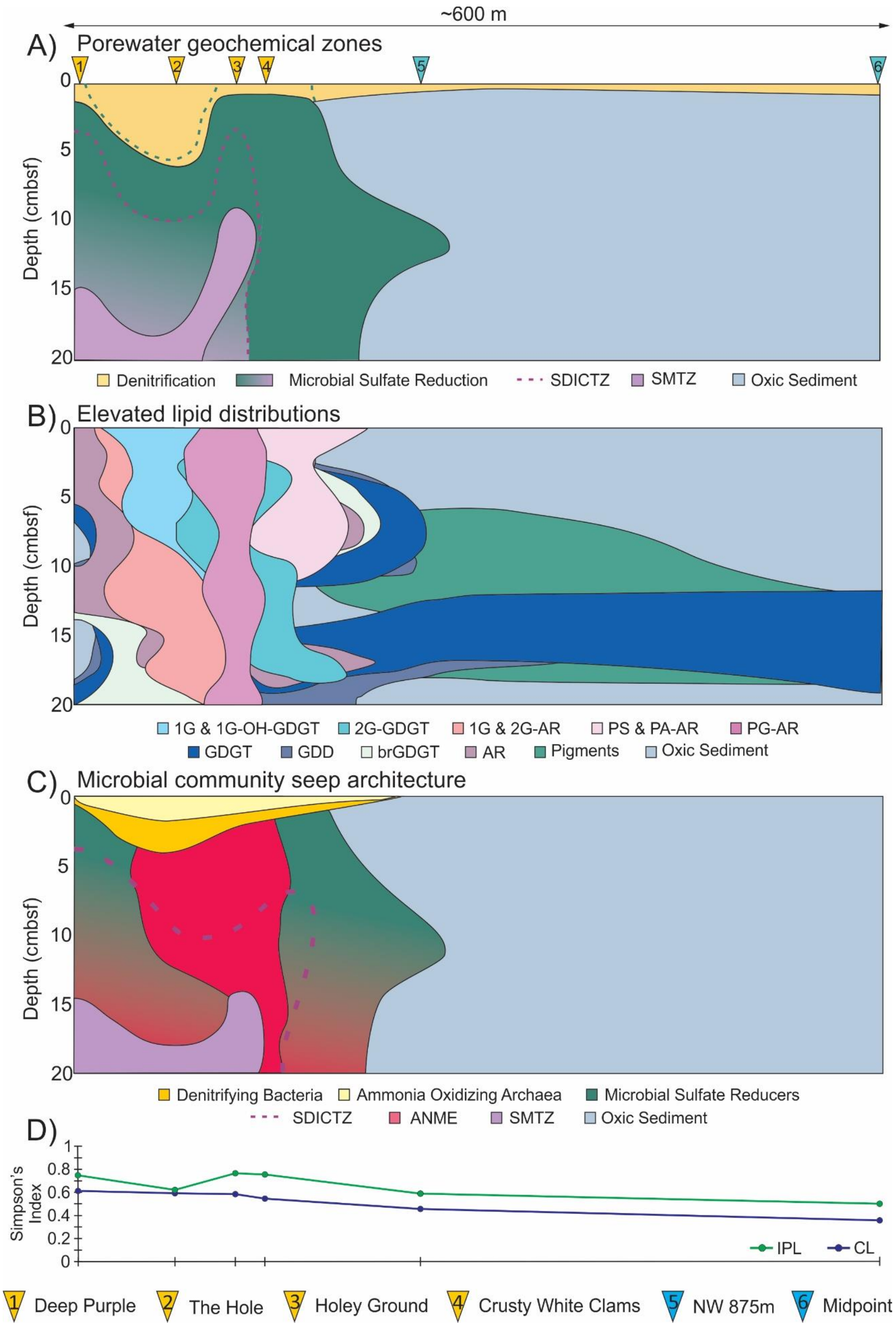
~600 m
A) Porewater geochemical zones
1
2
3
4
5
6
Depth (cmbsf)
0
5
10
15
20
Denitrification
Microbial Sulfate Reduction
SDICTZ
SMTZ
Oxic Sediment
B) Elevated lipid distributions
Depth (cmbsf)
0
5
10
15
20
1G & 1G-OH-GDGT
2G-GDGT
1G & 2G-AR
PS & PA-AR
PG-AR
GDGT
GDD
brGDGT
AR
Pigments
Oxic Sediment
C) Microbial community seep architecture
Depth (cmbsf)
0
5
10
15
20
Denitrifying Bacteria
Ammonia Oxidizing Archaea
Microbial Sulfate Reducers
SDICTZ
ANME
SMTZ
Oxic Sediment
D)
Simpson's Index
1
0.8
0.6
0.4
0.2
0
IPL
CL
1 Deep Purple
2 The Hole
3 Holey Ground
4 Crusty White Clams
5 NW 875m
6 Midpoint

Figure 4.12: Site 2A-1 microbial seep architecture. A) Porewater seep architecture (from Fig. 2.9). B) Lipid community structure based on geochemical proxies and IPL distributions. The GDGT distribution has been interpreted using the MI to represent not only CH_4 impact in the sediment but to visualize the ANME-1 community structure. C) Combined porewater and lipidomic microbial seep reconstruction. Lipid communities have been shaped by the underlying sediment and porewater geochemistry, modifying their interpretation from the above image. D) Average Simpson's Index value for each core across the 2A-1 transect.

4.5. Conclusion

The microbial lipidomic survey of Scotian Slope site 2A-1 tentatively identified 23 distinct lipid classes. CLs were found in a higher abundance across the seep transect than their intact precursors. Microbial diversity was higher within the seep sediments compared to the two ambient sites. Pigments were more concentrated in the ambient sites, suggesting selective heterotrophy is occurring within the seep. The CL-MI and IPL-MI reach up to a maximum of 0.9 within the seep sediments, suggesting that an ANME-1 type community is dominating AOM. Values of $\delta^{13}C_{TOC}$ are increasingly depleted within in the seep, reflecting values more closely associated with biogenic methane. The novel *br*SRI identified zones of increased SRB related activities. The porewater survey from Chapter 2, coupled to the extensive lipidomic survey presented in this chapter produced a novel two-dimensional reconstruction of the subsurface microbial communities and geochemical environment of Scotian Slope cold seep 2A-1. This reconstruction highlights the changes in the lipidome across an environmental gradient.

References

Barnes, R. O., & Goldberg, E. D. (1976). Methane production and consumption in anoxic marine sediments. *Geology*, *4*(5), 297. https://doi.org/10.1130/0091-7613(1976)4<297:MPACIA>2.0.CO;2

Bennett, R., & Desiage, P.-A. (2022). Expedition report 21CONDOR: Scotian Slope, August 14-29, 2021 (8889; p. 8889). https://doi.org/10.4095/329977

Bentley, J. N., Ventura, G. T., Dalzell, C. J., Walters, C. C., Peters, C. A., Mennito, A. S., Nelson, R. K., Reddy, C. M., Seewald, J. S., & Sievert, S. M. (2022). Archaeal lipid diversity, alteration, and preservation at the Cathedral Hill deep sea hydrothermal vent, Guaymas Basin, Gulf of California, and its implications regarding the deep time preservation paradox. *Organic Geochemistry*, *163*, 104302. https://doi.org/10.1016/j.orggeochem.2021.104302

Bianchi, T. S., Johansson, B., & Elmgren, R. (2000). Breakdown of phytoplankton pigments in Baltic sediments: Effects of anoxia and loss of deposit-feeding macrofauna. *Journal of Experimental Marine Biology and Ecology*, *251*(2), 161–183. https://doi.org/10.1016/S0022-0981(00)00212-4

Blumenberg, M., Seifert, R., Reitner, J., Pape, T., & Michaelis, W. (2004). Membrane lipid patterns typify distinct anaerobic methanotrophic consortia. *Proceedings of the National Academy of Sciences*, *101*(30), 11111–11116. https://doi.org/10.1073/pnas.0401188101

Boetius, A., Ravenschlag, K., Schubert, C. J., Rickert, D., Widdel, F., Gieseke, A., Amann, R., Jørgensen, B. B., Witte, U., & Pfannkuche, O. (2000). A marine microbial consortium apparently mediating anaerobic oxidation of methane. *Nature*, *407*(6804), 623–626. https://doi.org/10.1038/35036572

Boon, A., & Duineveld, G. (1998). Chlorophyll a as a marker for bioturbation and carbon flux in southern and central North Sea sediments. *Marine Ecology Progress Series*, *162*, 33–43. https://doi.org/10.3354/meps162033

Borowski, W. S., Paull, C. K., & Ussler, W. (1996). Marine pore-water sulfate profiles indicate in situ methane flux from underlying gas hydrate. *Geology*, *24*(7), 655. https://doi.org/10.1130/0091-7613(1996)024<0655:MPWSPI>2.3.CO;2

Campbell, D. C. (2019). CCGS Hudson Expedition 2016-011, phase 2. Cold seep investigations on the Scotian Slope, offshore Nova Scotia, June 15-July 6, 2016 (8525; p. 8525). https://doi.org/10.4095/313603

Chen, K., Ríos, J. J., Roca, M., & Pérez-Gálvez, A. (2015). Development of an accurate and high-throughput methodology for structural comprehension of chlorophylls derivatives. (II) Dephytylated derivatives. *Journal of Chromatography A*, *1412*, 90–99. https://doi.org/10.1016/j.chroma.2015.08.007

Chowdhury, A., Ventura, G. T., Owino, Y., Lalk, E. J., MacAdam, N., Dooma, J. M., Ono, S., Fowler, M., MacDonald, A., Bennett, R., MacRae, R. A., Hubert, C. R. J., Bentley, J. N., & Kerr, M. J. (2024). Cold seep formation from salt diapir–controlled deep biosphere oases. *Proceedings of the National Academy of Sciences*, *121*(12), e2316878121. https://doi.org/10.1073/pnas.2316878121

Craig, H. (1957). Isotopic standards for carbon and oxygen and correction factors for mass-spectrometric analysis of carbon dioxide. *Geochimica et Cosmochimica Acta*, *12*(1–2), 133–149. https://doi.org/10.1016/0016-7037(57)90024-8

Crann, C. A., Murseli, S., St-Jean, G., Zhao, X., Clark, I. D., & Kieser, W. E. (2017). First Status Report on Radiocarbon Sample Preparation Techniques at the A.E. Lalonde AMS Laboratory (Ottawa, Canada). *Radiocarbon*, *59*(3), 695–704. https://doi.org/10.1017/RDC.2016.55

Damsté, J. S. S., Hopmans, E. C., Pancost, R. D., Schouten, S., & Geenevasen, J. A. J. (2000). Newly discovered non-isoprenoid glycerol dialkylglycerol tetraether lipids in sediments. *Chemical Communications*, *17*, 1683–1684. https://doi.org/10.1039/B004517I

De La Torre, J. R., Walker, C. B., Ingalls, A. E., Könneke, M., & Stahl, D. A. (2008). Cultivation of a thermophilic ammonia oxidizing archaeon synthesizing crenarchaeol. *Environmental Microbiology*, *10*(3), 810–818. https://doi.org/10.1111/j.1462-2920.2007.01506.x

Elling, F. J., Könneke, M., Nicol, G. W., Stieglmeier, M., Bayer, B., Spieck, E., de la Torre, J. R., Becker, K. W., Thomm, M., Prosser, J. I., Herndl, G. J., Schleper, C., & Hinrichs, K.-U. (2017). Chemotaxonomic characterisation of the thaumarchaeal lipidome. *Environmental Microbiology*, *19*(7), 2681–2700. https://doi.org/10.1111/1462-2920.13759

Elvert, M., Suess, E., Greinert, J., & Whiticar, M. J. (2000). Archaea mediating anaerobic methane oxidation in deep-sea sediments at cold seeps of the eastern Aleutian subduction zone. *Organic Geochemistry*, *31*(11), 1175–1187. https://doi.org/10.1016/S0146-6380(00)00111-X

Francis, C. A., Roberts, K. J., Beman, J. M., Santoro, A. E., & Oakley, B. B. (2005). Ubiquity and diversity of ammonia-oxidizing archaea in water columns and sediments of the ocean. *Proceedings of the National Academy of Sciences*, *102*(41), 14683–14688. https://doi.org/10.1073/pnas.0506625102

Harvey, H. R., Fallon, R. D., & Patton, J. S. (1986). The effect of organic matter and oxygen on the degradation of bacterial membrane lipids in marine sediments. *Geochimica et Cosmochimica Acta*, *50*(5), 795–804. https://doi.org/10.1016/0016-7037(86)90355-8

Hingley, J. S., Martins, C. C., Walker-Trivett, C., Adams, J. K., Naeher, S., Häggi, C., Feakins, S. J., & Naafs, B. D. A. (2024). The global distribution of Isoprenoidal Glycerol Dialkyl Diethers (isoGDDs) is consistent with a predominant degradation origin. *Organic Geochemistry*, *192*, 104782. https://doi.org/10.1016/j.orggeochem.2024.104782

Hinrichs, K.-U., Hayes, J. M., Sylva, S. P., Brewer, P. G., & DeLong, E. F. (1999). Methane-consuming archaebacteria in marine sediments. *Nature*, *398*(6730), 802–805. https://doi.org/10.1038/19751

Hopmans, E. C., Schouten, S., Pancost, R. D., Van Der Meer, M. T. J., & Sinninghe Damsté, J. S. (2000). Analysis of intact tetraether lipids in archaeal cell material and sediments by high performance liquid chromatography/atmospheric pressure chemical ionization mass spectrometry. *Rapid Communications in Mass Spectrometry*, *14*(7), 585–589. https://doi.org/10.1002/(SICI)1097-0231(20000415)14:7<585::AID-RCM913>3.0.CO;2-N

Hopmans, E. C., Weijers, J. W. H., Schefuß, E., Herfort, L., Sinninghe Damsté, J. S., & Schouten, S. (2004). A novel proxy for terrestrial organic matter in sediments based on branched and isoprenoid tetraether lipids. *Earth and Planetary Science Letters*, *224*(1–2), 107–116. https://doi.org/10.1016/j.epsl.2004.05.012

Ingalls, A. E., Aller, R. C., Lee, C., & Sun, M.-Y. (2000). The influence of deposit-feeding on chlorophyll-<I>a</I> degradation in coastal marine sediments. *Journal of Marine Research*, *58*(4), 631–651. https://doi.org/10.1357/002224000321511052

Joye, S. B. (2020). The Geology and Biogeochemistry of Hydrocarbon Seeps. *Annual Review of Earth and Planetary Sciences*, *48*(1), 205–231. https://doi.org/10.1146/annurev-earth-063016-020052

Kendell, K. L. (2012). Variations in salt expulsion style within the Sable Canopy Complex, central Scotian margin ^{1} This article is one of a series of papers published in this CJES Special Issue on the theme of *Mesozoic–Cenozoic geology of the Scotian Basin* . *Canadian Journal of Earth Sciences*, *49*(12), 1504–1522. https://doi.org/10.1139/e2012-069

Kim, B., & Zhang, Y. G. (2023). Methane Index: Towards a quantitative archaeal lipid biomarker proxy for reconstructing marine sedimentary methane fluxes. *Geochimica et Cosmochimica Acta*, *354*, 74–87. https://doi.org/10.1016/j.gca.2023.06.008

Knittel, K., & Boetius, A. (2009). Anaerobic Oxidation of Methane: Progress with an Unknown Process. *Annual Review of Microbiology*, *63*(1), 311–334. https://doi.org/10.1146/annurev.micro.61.080706.093130

Knittel, K., Lösekann, T., Boetius, A., Kort, R., & Amann, R. (2005). Diversity and Distribution of Methanotrophic Archaea at Cold Seeps. *Applied and Environmental Microbiology*, *71*(1), 467–479. https://doi.org/10.1128/AEM.71.1.467-479.2005

Koga, Y., & Morii, H. (2005). Recent Advances in Structural Research on Ether Lipids from Archaea Including Comparative and Physiological Aspects. *Bioscience, Biotechnology, and Biochemistry*, *69*(11), 2019–2034. https://doi.org/10.1271/bbb.69.2019

Koga, Y., Nishihara, M., Morii, H., & Akagawa-Matsushita, M. (1993). Ether polar lipids of methanogenic bacteria: Structures, comparative aspects, and biosyntheses. *Microbiological Reviews*, *57*(1), 164–182. https://doi.org/10.1128/mr.57.1.164-182.1993

Könneke, M., Bernhard, A. E., de la Torre, J. R., Walker, C. B., Waterbury, J. B., & Stahl, D. A. (2005). Isolation of an autotrophic ammonia-oxidizing marine archaeon. *Nature*, *437*(7058), 543–546. https://doi.org/10.1038/nature03911

Kuypers, M. M. M., Blokker, P., Erbacher, J., Kinkel, H., Pancost, R. D., Schouten, S., & Sinninghe Damsté, J. S. (2001). Massive Expansion of Marine Archaea During a Mid-Cretaceous Oceanic Anoxic Event. *Science*, *293*(5527), 92–95. https://doi.org/10.1126/science.1058424

Lengger, S. K., Sutton, P. A., Rowland, S. J., Hurley, S. J., Pearson, A., Naafs, B. D. A., Dang, X., Inglis, G. N., & Pancost, R. D. (2018). Archaeal and bacterial glycerol dialkyl glycerol tetraether (GDGT) lipids in environmental samples by high temperature-gas chromatography with flame ionisation and time-of-flight mass spectrometry detection. *Organic Geochemistry*, *121*, 10–21. https://doi.org/10.1016/j.orggeochem.2018.03.012

Levin, L. A. (2005). Ecology of Cold Seep Sediments: Interactions of Fauna with Flow, Chemistry and Microbes. In *Oceanography and Marine Biology*. CRC Press.

Lin, Y., Lipp, J. S., Elvert, M., Holler, T., & Hinrichs, K. (2013). Assessing production of the ubiquitous archaeal diglycosyl tetraether lipids in marine subsurface sediment using intramolecular stable isotope probing. *Environmental Microbiology*, *15*(5), 1634–1646. https://doi.org/10.1111/j.1462-2920.2012.02888.x

Lincoln, S. A., Wai, B., Eppley, J. M., Church, M. J., Summons, R. E., & DeLong, E. F. (2014). Planktonic Euryarchaeota are a significant source of archaeal tetraether lipids in the ocean. *Proceedings of the National Academy of Sciences*, *111*(27), 9858–9863. https://doi.org/10.1073/pnas.1409439111

Lipp, J. S., & Hinrichs, K.-U. (2009). Structural diversity and fate of intact polar lipids in marine sediments. *Geochimica et Cosmochimica Acta*, *73*(22), 6816–6833. https://doi.org/10.1016/j.gca.2009.08.003

Lipp, J. S., Morono, Y., Inagaki, F., & Hinrichs, K.-U. (2008). Significant contribution of Archaea to extant biomass in marine subsurface sediments. *Nature*, *454*(7207), 991–994. https://doi.org/10.1038/nature07174

Liu, X.-L, Summons, R. E., & Hinrichs, K. (2012a). Extending the known range of glycerol ether lipids in the environment: Structural assignments based on tandem mass spectral fragmentation patterns. *Rapid Communications in Mass Spectrometry*, *26*(19), 2295–2302. https://doi.org/10.1002/rcm.6355

Liu, X.-L., Lipp, J. S., Schröder, J. M., Summons, R. E., & Hinrichs, K.-U. (2012b). Isoprenoid glycerol dialkanol diethers: A series of novel archaeal lipids in marine sediments. *Organic Geochemistry*, *43*, 50–55. https://doi.org/10.1016/j.orggeochem.2011.11.002

Liu, X.-L., Lipp, J. S., Simpson, J. H., Lin, Y.-S., Summons, R. E., & Hinrichs, K.-U. (2012c). Mono- and dihydroxyl glycerol dibiphytanyl glycerol tetraethers in marine sediments: Identification of both core and intact polar lipid forms. *Geochimica et Cosmochimica Acta*, *89*, 102–115. https://doi.org/10.1016/j.gca.2012.04.053

Liu, X.-L., Zhu, C., Wakeham, S. G., & Hinrichs, K.-U. (2014). In situ production of branched glycerol dialkyl glycerol tetraethers in anoxic marine water columns. *Marine Chemistry*, *166*, 1–8. https://doi.org/10.1016/j.marchem.2014.08.008

Meador, T. B., Zhu, C., Elling, F. J., Könneke, M., & Hinrichs, K.-U. (2014). Identification of isoprenoid glycosidic glycerol dibiphytanol diethers and indications for their biosynthetic origin. *Organic Geochemistry*, *69*, 70–75. https://doi.org/10.1016/j.orggeochem.2014.02.005

Meyers, P. A. (1994). Preservation of elemental and isotopic source identification of sedimentary organic matter. *Chemical Geology*, *114*(3–4), 289–302. https://doi.org/10.1016/0009-2541(94)90059-0

Milenkovic, S., Zvezdanović, J., Anđelković, T., & Marković, D. (2012). The identification of chlorophyll and its derivatives in the pigment mixtures: HPLC-chromatography, visible and mass spectroscopy studies. *Savremene Tehnologije*, *1*, 16–24.

Murseli, S., Middlestead, P., St-Jean, G., Zhao, X., Jean, C., Crann, C. A., Kieser, W. E., & Clark, I. D. (2019). The Preparation of Water (DIC, DOC) and Gas (CO_2, CH_4) Samples for Radiocarbon Analysis at AEL-AMS, Ottawa, Canada. *Radiocarbon*, *61*(5), 1563–1571. https://doi.org/10.1017/RDC.2019.14

Niemann, H., & Elvert, M. (2008). Diagnostic lipid biomarker and stable carbon isotope signatures of microbial communities mediating the anaerobic oxidation of methane with sulphate. *Organic Geochemistry*, *39*(12), 1668–1677. https://doi.org/10.1016/j.orggeochem.2007.11.003

Niemann, H., Lösekann, T., De Beer, D., Elvert, M., Nadalig, T., Knittel, K., Amann, R., Sauter, E. J., Schlüter, M., Klages, M., Foucher, J. P., & Boetius, A. (2006). Novel microbial communities of the Haakon Mosby mud volcano and their role as a methane sink. *Nature*, *443*(7113), 854–858. https://doi.org/10.1038/nature05227

Orphan, V. J., Hinrichs, K.-U., Ussler, W., Paull, C. K., Taylor, L. T., Sylva, S. P., Hayes, J. M., & Delong, E. F. (2001). Comparative Analysis of Methane-Oxidizing Archaea and Sulfate-Reducing Bacteria in Anoxic Marine Sediments. *Applied and Environmental Microbiology*, *67*(4), 1922–1934. https://doi.org/10.1128/AEM.67.4.1922-1934.2001

Orphan, V. J., House, C. H., Hinrichs, K.-U., McKeegan, K. D., & DeLong, E. F. (2002). Multiple archaeal groups mediate methane oxidation in anoxic cold seep sediments. *Proceedings of the National Academy of Sciences*, *99*(11), 7663–7668. https://doi.org/10.1073/pnas.072210299

Pearson, A., Hurley, S. J., Walter, S. R. S., Kusch, S., Lichtin, S., & Zhang, Y. G. (2016). Stable carbon isotope ratios of intact GDGTs indicate heterogeneous sources to marine sediments. *Geochimica et Cosmochimica Acta*, *181*, 18–35. https://doi.org/10.1016/j.gca.2016.02.034

Peterse, F., Kim, J.-H., Schouten, S., Kristensen, D. K., Koç, N., & Sinninghe Damsté, J. S. (2009). Constraints on the application of the MBT/CBT palaeothermometer at high latitude environments (Svalbard, Norway). *Organic Geochemistry*, *40*(6), 692–699. https://doi.org/10.1016/j.orggeochem.2009.03.004

Pitcher, A., Hopmans, E. C., Mosier, A. C., Park, S.-J., Rhee, S.-K., Francis, C. A., Schouten, S., & Sinninghe Damsté, J. S. (2011). Core and Intact Polar Glycerol Dibiphytanyl Glycerol Tetraether Lipids of Ammonia-Oxidizing Archaea Enriched from Marine and Estuarine Sediments. *Applied and Environmental Microbiology*, *77*(10), 3468–3477. https://doi.org/10.1128/AEM.02758-10

Rooze, J., Peterson, L., Peterson, R. N., & Meile, C. (2020). Porewater flow patterns in surficial cold seep sediments inferred from conservative tracer profiles and early diagenetic modeling. *Chemical Geology*, *536*, 119468. https://doi.org/10.1016/j.chemgeo.2020.119468

Rossel, P. E., Elvert, M., Ramette, A., Boetius, A., & Hinrichs, K.-U. (2011). Factors controlling the distribution of anaerobic methanotrophic communities in marine environments: Evidence from intact polar membrane lipids. *Geochimica et Cosmochimica Acta*, *75*(1), 164–184. https://doi.org/10.1016/j.gca.2010.09.031

Rossel, P. E., Lipp, J. S., Fredricks, H. F., Arnds, J., Boetius, A., Elvert, M., & Hinrichs, K.-U. (2008). Intact polar lipids of anaerobic methanotrophic archaea and associated bacteria. *Organic Geochemistry*, *39*(8), 992–999. https://doi.org/10.1016/j.orggeochem.2008.02.021

Rush, D., & Sinninghe Damsté, J. S. (2017). Lipids as paleomarkers to constrain the marine nitrogen cycle. *Environmental Microbiology*, *19*(6), 2119–2132. https://doi.org/10.1111/1462-2920.13682

Rütters, H., Sass, H., Cypionka, H., & Rullkötter, J. (2002). Phospholipid analysis as a tool to study complex microbial communities in marine sediments. *Journal of Microbiological Methods*, *48*(2), 149–160. https://doi.org/10.1016/S0167-7012(01)00319-0

Schouten, S., Hoefs, M. J. L., Koopmans, M. P., Bosch, H.-J., & Sinninghe Damsté, J. S. (1998). Structural characterization, occurrence and fate of archaeal ether-bound acyclic and cyclic biphytanes and corresponding diols in sediments. *Organic Geochemistry*, *29*(5), 1305–1319. https://doi.org/10.1016/S0146-6380(98)00131-4

Schouten, S., Hopmans, E. C., Pancost, R. D., & Damsté, J. S. S. (2000). Widespread occurrence of structurally diverse tetraether membrane lipids: Evidence for the ubiquitous presence of low-temperature relatives of hyperthermophiles. *Proceedings of the National Academy of Sciences*, *97*(26), 14421–14426. https://doi.org/10.1073/pnas.97.26.14421

Schouten, S., Hopmans, E. C., Schefuß, E., & Sinninghe Damsté, J. S. (2002). Distributional variations in marine crenarchaeotal membrane lipids: A new tool for reconstructing ancient sea water temperatures? *Earth and Planetary Science Letters*, *204*(1–2), 265–274. https://doi.org/10.1016/S0012-821X(02)00979-2

Schouten, S., Hopmans, E. C., & Sinninghe Damsté, J. S. (2013). The organic geochemistry of glycerol dialkyl glycerol tetraether lipids: A review. *Organic Geochemistry*, *54*, 19–61. https://doi.org/10.1016/j.orggeochem.2012.09.006

Schouten, S., Middelburg, J. J., Hopmans, E. C., & Sinninghe Damsté, J. S. (2010). Fossilization and degradation of intact polar lipids in deep subsurface sediments: A theoretical approach. *Geochimica et Cosmochimica Acta*, *74*(13), 3806–3814. https://doi.org/10.1016/j.gca.2010.03.029

Schubotz, F., Wakeham, S. G., Lipp, J. S., Fredricks, H. F., & Hinrichs, K. (2009). Detection of microbial biomass by intact polar membrane lipid analysis in the water column and surface sediments of the Black Sea. *Environmental Microbiology*, *11*(10), 2720–2734. https://doi.org/10.1111/j.1462-2920.2009.01999.x

Simpson, E. H. (1949). Measurement of Diversity. *Nature*, *163*(4148), 688–688. https://doi.org/10.1038/163688a0

Solomon, E. A., Kastner, M., Jannasch, H., Robertson, G., & Weinstein, Y. (2008). Dynamic fluid flow and chemical fluxes associated with a seafloor gas hydrate deposit on the northern Gulf of Mexico slope. *Earth and Planetary Science Letters*, *270*(1–2), 95–105. https://doi.org/10.1016/j.epsl.2008.03.024

Sturt, H. F., Summons, R. E., Smith, K., Elvert, M., & Hinrichs, K. (2004). Intact polar membrane lipids in prokaryotes and sediments deciphered by high-performance liquid chromatography/electrospray ionization multistage mass spectrometry—New biomarkers for biogeochemistry and microbial ecology. *Rapid Communications in Mass Spectrometry*, *18*(6), 617–628. https://doi.org/10.1002/rcm.1378

Suess, E. (2020). Marine Cold Seeps: Background and Recent Advances. In H. Wilkes (Ed.), *Hydrocarbons, Oils and Lipids: Diversity, Origin, Chemistry and Fate* (pp. 747–767). Springer International Publishing. https://doi.org/10.1007/978-3-319-90569-3_27

Sun, M.-Y., & Dai, J. (2005). Relative influences of bioturbation and physical mixing on degradation of bloom-derived particulate organic matter: Clue from microcosm experiments. *Marine Chemistry*, *96*(3–4), 201–218. https://doi.org/10.1016/j.marchem.2004.11.003

Sun, M.-Y., Lee, C., & Aller, R. C. (1993). Anoxic and oxic degradation of ^{14} C-labeled chloropigments and a ^{14} C-labeled diatom in Long Island Sound sediments. *Limnology and Oceanography*, *38*(7), 1438–1451. https://doi.org/10.4319/lo.1993.38.7.1438

Valentine, D. L. (2007). Adaptations to energy stress dictate the ecology and evolution of the Archaea. *Nature Reviews Microbiology*, *5*(4), 316–323. https://doi.org/10.1038/nrmicro1619

White, D. C., Davis, W. M., Nickels, J. S., King, J. D., & Bobbie, R. J. (1979). Determination of the sedimentary microbial biomass by extractible lipid phosphate. *Oecologia*, *40*(1), 51–62. https://doi.org/10.1007/BF00388810

Whiticar, M. J. (1999). Carbon and hydrogen isotope systematics of bacterial formation and oxidation of methane. *Chemical Geology*, *161*(1–3), 291–314. https://doi.org/10.1016/S0009-2541(99)00092-3

Woulds, C., & Cowie, G. L. (2009). Sedimentary pigments on the Pakistan margin: Controlling factors and organic matter dynamics. *Deep Sea Research Part II: Topical Studies in Oceanography*, *56*(6–7), 347–357. https://doi.org/10.1016/j.dsr2.2008.05.033

Xiao, W., Wang, Y., Zhou, S., Hu, L., Yang, H., & Xu, Y. (2016). Ubiquitous production of branched glycerol dialkyl glycerol tetraethers (brGDGTs) in global marine environments: A new source indicator for brGDGTs. *Biogeosciences*, *13*(20), 5883–5894. https://doi.org/10.5194/bg-13-5883-2016

Xie, S., Lipp, J. S., Wegener, G., Ferdelman, T. G., & Hinrichs, K.-U. (2013). Turnover of microbial lipids in the deep biosphere and growth of benthic archaeal populations. *Proceedings of the National Academy of Sciences*, *110*(15), 6010–6014. https://doi.org/10.1073/pnas.1218569110

Yoshinaga, M. Y., Kellermann, M. Y., Rossel, P. E., Schubotz, F., Lipp, J. S., & Hinrichs, K. (2011). Systematic fragmentation patterns of archaeal intact polar lipids by high-performance liquid chromatography/electrospray ionization ion-trap mass spectrometry. *Rapid Communications in Mass Spectrometry*, *25*(23), 3563–3574. https://doi.org/10.1002/rcm.5251

Yunker, M. B., Belicka, L. L., Harvey, H. R., & Macdonald, R. W. (2005). Tracing the inputs and fate of marine and terrigenous organic matter in Arctic Ocean sediments: A multivariate analysis of lipid biomarkers. *Deep Sea Research Part II: Topical Studies in Oceanography*, *52*(24), 3478–3508. https://doi.org/10.1016/j.dsr2.2005.09.008

Zhang, T., He, W., Liang, Q., Zheng, F., Xiao, X., Zeng, Z., Zhou, J., Yao, W., Chen, H., Zhu, Y., Zhao, J., Zheng, Y., & Zhang, C. (2023). Lipidomic diversity and proxy implications of archaea from cold seep sediments of the South China Sea. *Frontiers in Microbiology*, *14*, 1241958. https://doi.org/10.3389/fmicb.2023.1241958

Zhang, Y. G., Zhang, C. L., Liu, X.-L., Li, L., Hinrichs, K.-U., & Noakes, J. E. (2011). Methane Index: A tetraether archaeal lipid biomarker indicator for detecting the instability of marine gas hydrates. *Earth and Planetary Science Letters*, *307*(3), 525–534. https://doi.org/10.1016/j.epsl.2011.05.031

Zhang, Z.-X., Li, J., Chen, Z., Sun, Z., Yang, H., Fu, M., & Peng, X. (2020). The effect of methane seeps on the bacterial tetraether lipid distributions at the Okinawa Trough. *Marine Chemistry*, *225*, 103845. https://doi.org/10.1016/j.marchem.2020.103845

Zhang, Z.-X., Li, J., Lu, H., Yang, H., Zhang, Y., Tang, Y., Fu, M., & Peng, X. (2024). Bacterial glycerol tetraethers as a potential tool to trace marine methane cycling. *Limnology and Oceanography*, *69*(1), 104–120. https://doi.org/10.1002/lno.12462

Zhu, Q.-Z., Elvert, M., Meador, T. B., Becker, K. W., Heuer, V. B., & Hinrichs, K. (2021). Stable carbon isotopic compositions of archaeal lipids constrain terrestrial, planktonic, and benthic sources in marine sediments. *Geochimica et Cosmochimica Acta*, *307*, 319–337. https://doi.org/10.1016/j.gca.2021.04.037

Chapter 5: Conclusions and Future Directions

5.1 Key Conclusions

Seventy-six sediment samples collected from Site 2A-1 on the Scotian Slope were studied to provide new insights into the microbial communities that inhabit cold seep shallow sediments. This project achieved the objectives outlined in Chapter 1, section 4.

The first objective was to resolve biochemical cycling of targeted ions by linking porewater profiles with lipid-based proxies. Downcore ion concentration profiles resolved as heatmaps, coupled with principal component analysis (PCA) revealed a high correlation between the inverse concentrations of sulfate (SO_4^{2-}) and dissolved inorganic carbon (DIC). A composite cross plot of SO_4^{2-} and DIC concentrations was used to interpret a potential depth for the sulfate-methane transition zone (SMTZ) as well as a zone of microbial sulfate reduction (MSR) and the sulfate dissolved inorganic carbon transition zone. An idealized model of the SDICTZ was used to classy the system as non-diffusion limited and used the stoichiometric relationship of SO_4^{2-} and DIC to qualitatively gauge the systems alkalinity and carbonate precipitation. Heatmaps of lipid biomarkers, related to the anaerobic oxidation of methane (AOM) were used to interpret the microbial community structure associated with each porewater designated geochemical zone.

The second objective was to explore the spatial arrangement of push cores and resolve the changes along an environmental gradient. The porewater and lipid concentration downcore profiles were spatially resolved across the transect using heatmaps generated as contour plots in MATLAB_plsToolKit. The spatial resolution supports the hypothesis of a level of seep heterogeneity created by horizontal hydrocarbon flux. This technique is a novel visualization, previously unobserved in cold seep literature. The microbial community diversity was calculated using a modified Simpson's Diversity Index equation which revealed distinct differences in community structure between the living and fossilised membrane lipids as well as within and out of the seep. These results support the hypothesis that microbial diversity is an effect of the level of chemical energy available within a system. Spatial resolution of the porewater and lipid concentrations were used to define the geochemical seep boundary.

Finally, the last objective was to resolve the porewater-lipid interaction as whole scale reconstruction of the geochemical seep architecture. Statistical relationships between members of the lipid community and porewater geochemical zones were resolved using PCA. Geochemical zones previously defined by the porewater chemistry were used to shape lipid communities within the seep structure. This two-dimensional reconstruction supports the hypothesis that the lipid community is directly affected CH_4 seepage.

5.2 Future Work

The main target of the microbial lipid survey was Archaeal lipids. To provide a more complete view of the lipidome, bacterial lipids must be included in future surveys. Bacterial lipids of Site 2A-1 could be studied in future work by injecting an aliquot of the total lipid extract (TLE) to be analysed using hydrophilic interaction chromatography (HILIC) HPLC. This would expand the biomarker window to reveal more energy transfer pathways in marine biogeochemical cycles studied in this project. AOM is a coupled reaction between anaerobic methane oxidizing archaea (ANME) and sulfate reducing bacteria (SRB), but the analytical techniques used do not allow for the detection of any SRB biomarkers. Additionally, as the ubiquitous glycerol dialkyl glycerol tetraethers GDGTs are the only archaeal biomarkers of nitrogen cycle activity, bacterial biomarkers could be used to better constrain zones of denitrification and ammonia oxidation. In addition of bacterial lipids, ^{13}C isotopes of AOM lipid biomarkers, would reveal carbon cycling pathways and can better constrain the depth of the SMTZ.

The porewater ion survey could be expanded to include calcium (Ca^{2+}) and magnesium (Mg^{2+}). Cross-plots of ($\Delta DIC + \Delta Ca^{2+} + \Delta Mg^{2+}$) versus ΔSO_4^{2-} can be used to quantify the relative consumption of SO_4^{2-} during AOM and MSR (Haese et al., 2003; Chen et al., 2010; Luo et al., 2013). The addition of this figure could improve the results presented in Chapter 2, section 4.2. Mg^{2+} and Ca^{2+} downcore profiles and concentration heat maps could also prove useful identifying zones of high carbonate precipitation.

The unique downcore profiles presented in this project by crenarchaeal and its respective intact polar lipid (IPL) precursor and glycerol dibiphytanyl diether (GDD) decay product lay the groundwork for continued research into lipid decay rates and preservation potential on the Scotian Slope. Using crenarchaeal as a biomarker for water column sourced Thaumarcheota, downcore profiles revealed potential evidence for in-situ production of GDGT-5 and for a biosynthetic origin for GDDs. The lack of systematic divergence in the downcore profiles of 1G-GDGT-5, GDGT-5, and GDD-5 calls into question current understandings of glycosidic headgroup hydrolysis rates and preservation in shallow sediments. The persistence of the 1G- headgroup has been previously noted by Schouten et al. (2010) and within the Site 2A-1 sediments appears to be extending past its calculated decay rate. These results challenge the application of glycosidic headgroups as IPL biomarkers for indicating modern environmental conditions. No definitive conclusions can be drawn from these results but encourage future research into lipid formation and decay rates.

5.3 The Big Picture

On a larger scale this project contributes to a Nova Scotia Department of Natural Resources and Renewables open-source database of the Scotian Slope with the objective of encouraging oil and gas development on Nova Scotia's offshore. The project dovetails immense efforts from a variety of government and academic organizations to contain the petroleum system on the Scotian Slope. The two-dimensional reconstruction of Site 2A-1 can be applied across the basin to map hydrocarbon alteration at different seep sites. The sampling and analytical techniques used in this project can be applied to any cold seep or hydrothermal vent system, creating new ways to investigate ancient and modern microbial life and environments.

References

Chen, Y., Ussler, W., Haflidason, H., Lepland, A., Rise, L., Hovland, M., & Hjelstuen, B. O. (2010). Sources of methane inferred from pore-water δ13C of dissolved inorganic carbon in Pockmark G11, offshore Mid-Norway. *Chemical Geology*, *275*(3–4), 127–138. https://doi.org/10.1016/j.chemgeo.2010.04.013

Haese, R. R., Meile, C., Van Cappellen, P., & De Lange, G. J. (2003). Carbon geochemistry of cold seeps: Methane fluxes and transformation in sediments from Kazan mud volcano, eastern Mediterranean Sea. *Earth and Planetary Science Letters*, *212*(3–4), 361–375. https://doi.org/10.1016/S0012-821X(03)00226-7

Luo, M., Chen, L., Wang, S., Yan, W., Wang, H., & Chen, D. (2013). Pockmark activity inferred from pore water geochemistry in shallow sediments of the pockmark field in southwestern Xisha Uplift, northwestern South China Sea. *Marine and Petroleum Geology*, *48*, 247–259. https://doi.org/10.1016/j.marpetgeo.2013.08.018

Schouten, S., Middelburg, J. J., Hopmans, E. C., & Sinninghe Damsté, J. S. (2010). Fossilization and degradation of intact polar lipids in deep subsurface sediments: A theoretical approach. *Geochimica et Cosmochimica Acta*, *74*(13), 3806–3814. https://doi.org/10.1016/j.gca.2010.03.029

Appendix A: Supplementary Materials for Chapter 2

1. Principal Component Analysis

The "factoextra" package was used to visualize results of the PCA. A scree plot was used to determine the number of principal components used in the analysis (Fig. A1). The first two components were retained, as they explained nearly 80% of the variance in the data set.

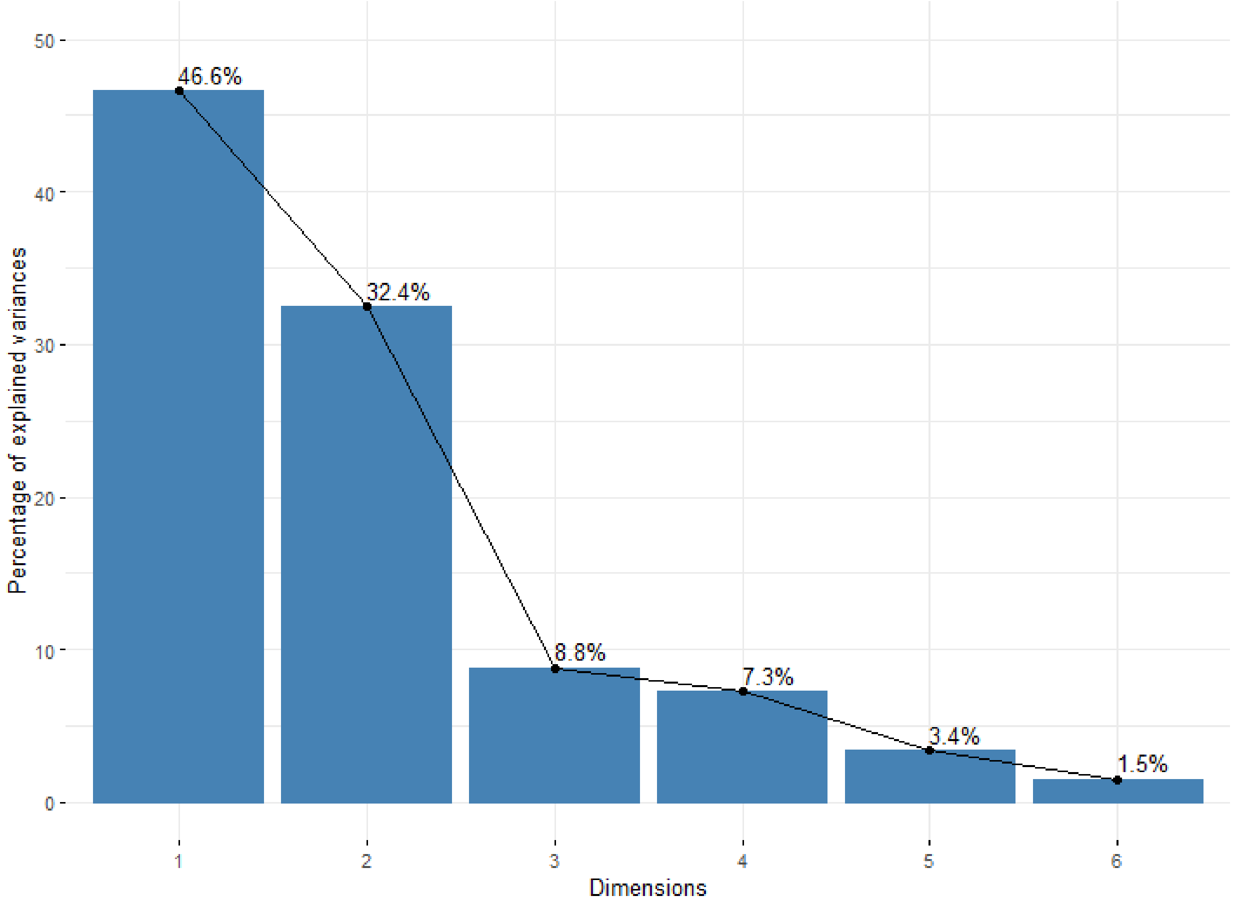

Figure A1.1: Scree plot of the porewater ion concentrations.

Using the result of the PCA, the $\cos^2$ of each ion was calculated to visualize the quality of representation of each variable by the principal components (Fig. A1.2a). A high cos2 value indicates that the variable is well represented by the PC and contributes significantly to the formation of the component. Similarly, the variable contribution was calculated to demonstrate the proportion of variance explain by the PC for each variable (Fig. A1.2b)

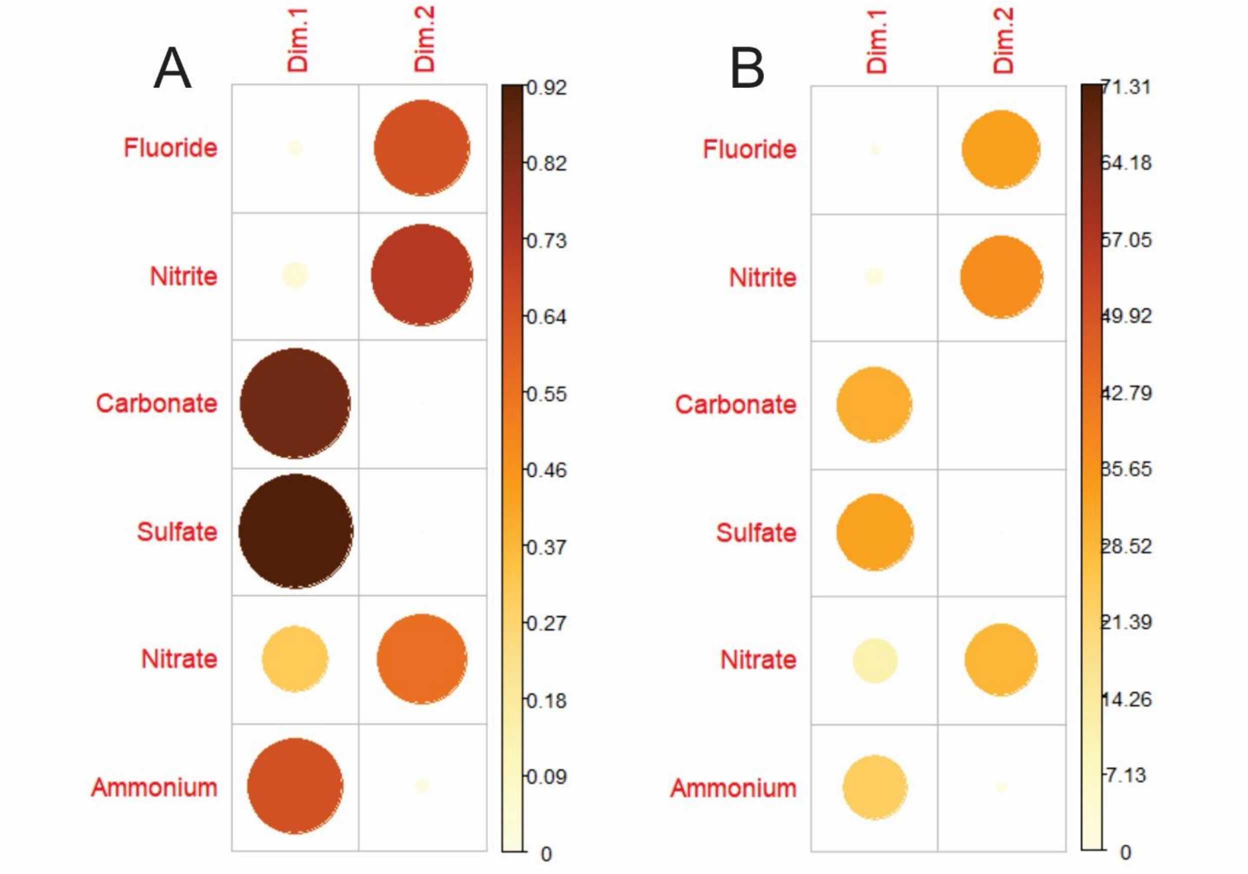

Figure A1.2: A) Cos2 values of each ion. B) Variable contribution values of each ion.

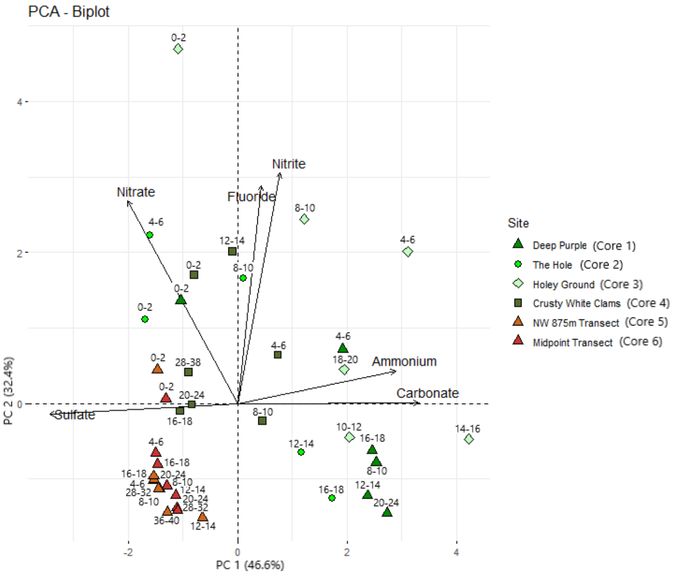

Figure A1.3: Depth annotated PCA biplot, modified from Figure 3.3.

2. Seep CH_4 Concentration

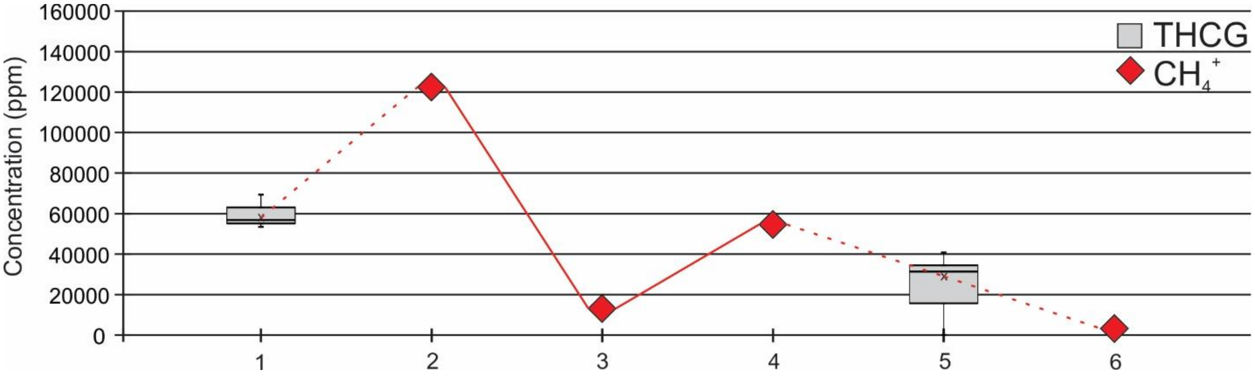

Figure A1.4: Methane (from Chowdhury et al., 2024) and total hydrocarbon gas (THCG; unpublished open-source file data supplied by Martin Fowler of Applied Petroleum Technologies) concentrations across the push core transect.

The seep gas at site 2A-1 is dominated by methane and is biogenic in origin (Chowdhury et al., 2024). The methane was formed at an approximate depth of ~1000 m. CH_4 concentrations were measured from the bottom of each core, approximately 30 to 40 cmbsf.

On average, CH_4 concentrations are highest in the seep and lower in the transect. The highest concentration of CH_4, 124268 ppm, was measured in core 2, which as observed by the ROV, was the only site of active gas seepage, or marcoseepage. The presence of gas bubbles escaping from the sediment here indicates that some CH_4 is bypassing the SMTZ and is not fully consumed during AOM (Knittel & Boetius, 2009). Unconstrained CH_4 fluxes at cold seeps, like at core 2, contribute to uncertainties in the global methane budget and carbon cycle (Knittel & Boetius, 2009; Reeburgh, 2007). Concentrations of CH_4 in core 2 are double the next highest concentration, 60618 ppm, from core 1.

Sampling location for cores 1, 2, and 3 were all chosen based on surficial indicators of CH_4 seepage, therefore varying CH_4 concentrations at these cores reflect different levels of microseepage. Core 3 had an anomalous low measurement of 11902 ppm. This does not necessarily imply that CH_4 seepage at this site is not occurring; low concentrations may be a result of extremely efficient AOM activity or high carbonate precipitation (Reeburgh, 2007). However, this anomaly cannot be solved without further analysis, such as depleted $\delta^{13}C$ values from lipid biomarkers, carbonates, or the sedimentary organic carbon (Hinrichs et al., 1999).

3. Seep Alkalinity Model

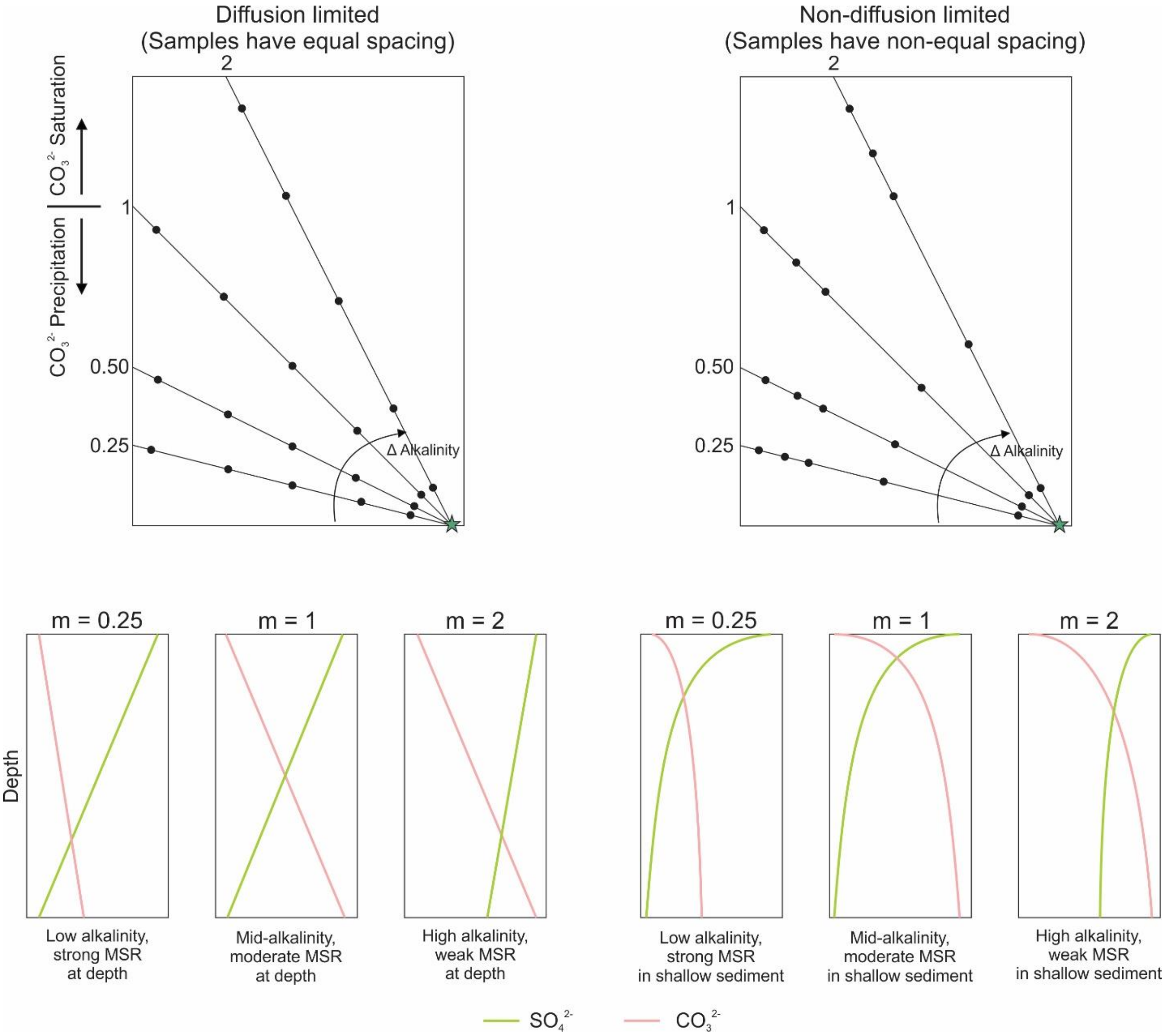

Figure A1.5: Expected modeled conditions required for the Figure 3.6 property-property plot. Sulfate versus carbonate property-property plot with ions pair flux changes indicated as four unique slopes following two styles of core sample distributions (top). Core samples that are evenly space along a gradient follow diffusive flow dynamics. Those non-linearly spaced require additional factors such as microbial mediated cycling, seepage, and ion sequestration. These conditions are further detailed in a series of down core profiles (bottom) covering three different gradient conditions.

Appendix B: Supplementary Materials for Chapter 3

1. Mass spectral characteristics of tentatively identified lipids

Table B1.1: Archaeal lipids names and diagnostic mass spectral characteristics used for identification.

Chemical Name	Abbreviation	RT (min)	Molecular Ion $[M^{+}H]^{+}$	Diagnostic Fragment Ion	References
Hydroxyl phosphatidic acid archaeol	PA-OH-AR	4	749.6	453.3	Yoshinaga et al., 2011
sn2-Hydroxyl Archaeol	OH-AR	8	669.17	367, 341	
Phosphatidic acid archaeol	PA-AR	9	733.6	453.3, 357.4	Yoshinaga et al., 2011
Phosphatidyl glycerol archaeol	PG-AR	9	807.7	733.6, 653.7	Yoshinaga et al., 2011
Biphytanediol	Bp-Diol	10	595.6388, 593.6244, 591.6100, 589.5956		Schouten et al., 1998
Diglycosidic Archaeol	2G-AR	11	977.7862	653, 373	Lipp and Hinrichs, 2009; Yoshinaga et al., 2011
Monoglycosidic Archaeol	1G-AR	13	815.7334	653, 373	Lipp and Hinrichs, 2009; Yoshinaga et al., 2011
Phosphatidylserine Archaeol	PS-AR	14	803.6735	733.6, 453.3	Yoshinaga et al., 2011
Archaeol	AR	19	653.6806	373.3	Lipp and Hinrichs, 2009; Yoshinaga et al., 2011
Hydroxylated glycerol dialkanol diether	OH-GDD (0-2)	33	1262.2913, 1260.2757, 1258.2601	686.6	Liu et al., 2012a
Phosphatidylglycerol glycerol dialkyl glycerol tetraether	PG-GDGT	34	1456.3227, 1454.3070, 1452.2914, 1450.2757, 1448.2601, 1446.2444	1380.3, 1300.0	Yoshinaga et al., 2011
Hydroxyl diglycosidic glycerol dialkyl glycerol tetraether	2G-OH-GDGT-0; 2G-OH-GDGT-2	34	1642.4283, 1640.4075, 1638.3919	1318.3, 760.7, 668.7	Lipp and Hinrichs, 2009; Liu et al., 2012c

Hydroxyl monoglycosidic glycerol dialkyl glycerol tetraether	1G-OH-GDGT (0-2)	38	1480.3704, 1478.3548, 1476.3391	1318.3, 760.7, 668.7	Lipp and Hinrichs, 2009; Liu et al., 2012a
Diglycosidic glycerol dialkyl glycerol tetraether	2G-GDGT (0-5)	40	1626.4283, 1624.4127, 1622.3970,1620.3814, 1618.3657, 1616.3501	1302.3, 743.7, 651.7	Stuart et al., 2004; Meador et al., 2014
Glycerol dialkanol diether	GDD	41	1246.2965, 1244.2808, 1242.2652, 1240.2495, 1238.2339, 1236.2182	669.6	Liu et al., 2012b
Hydroxyl Glycerol dialkyl glycerol tetraether	OH-GDGT (0-5)	43	1318.3176, 1316.3019. 1314.2863, 1312.2706, 1310.2550, 1308.2393	1302.3, 743.7, 651.7	Liu et al., 2012c
Monoglycosidic glycerol dialkyl glycerol tetraether	1G-GDGT-0; 1G-GDGT-5+5’	44	1464.3755, 1462.3598, 1460.3442, 1458.3285 1456.3129, 1454.2972	1302.3, 743.7, 651.7	Stuart et al., 2004
Glycerol dialkyl glycerol tetraether	GDGT-0; GDGT-5+5’	54	1302.3226, 1300.3070, 1298.2914, 1296.2757, 1294.2601, 1292.2444	1302.3, 743.7, 651.7	Hopmans et al., 2000; Schouten et al., 2013; Lengger et al., 2018

Table B1.2: Eukaryotic lipid names and diagnostic mass spectral characteristics used for identification.

Chemical Name	Abbreviation	RT (min)	Molecular Ion $[M^{+}H]^{+}$	Diagnostic Fragment Ion	References
Hydroxychlorophyll a	OH-Chlo	14	909.5502	593.3, 533.5	Chen et al., 2015
Hydroxypheophytin a	OH-Pheo	15	887.5782	591, 609	Milenkovic et al., 2012; Chen et al., 2015
Chlorophyll a	Chl a	17	893.5422	593.3, 533.5	Milenkovic et al., 2012; Chen et al., 2015
Pheophytin a	Pheo a	18	871.5721	591, 609	Chen et al., 2015

Table B1.3: Bacterial and mixed source br-GDGT mass spectral characteristics used for lipid identification.

Chemical Name	Abbreviation	RT (min)	Molecular Ion $[M^{+}H]^{+}$	Diagnostic Fragment Ion	References
Branched glycerol dialkyl glycerol tetraether	Br-GDGT	35	1050.0410, 1048.0253, 1046.0097, 1036.0253, 1034.0097, 1031.9940, 1022.0097, 1019.9921, 1017.9775	525.5, 489.6	Schouten et al, 2000, Hopmans et al., 2004

2. Radiocarbon age data.

Table B2.1: ^{14}C data provided by the André E. Lalonde AMS Laboratory (University of Ottawa).

Sample name	**^{14}C yr BP**	**±**	**$F^{14}C$**	**±**
2A-49, 0-2	3434	15	0.6521	0.0012
2A-49, 10-12	8005	20	0.3691	0.0009
2A-49, 28-32	12957	28	0.1993	0.0007
2A-49, 40-46	13777	31	0.1799	0.0007

3. Lipid Class Concentrations by Core

Table B3.1: Deep Purple (core 1) downcore lipid concentration (μg·g^{-1} sed).

Sample Name	GDGT	OH-GDGT	GDD	OH-GDD	AR	OH-AR	Bpdiol	br-GDGT	1G-GDGT	1G-OH-GDGT	2G-GDGT	2G-OH-GDGT	1G-AR	2G-AR	PA-AR	PA-OH-AR	PG-AR	PS-AR	PG-GDGT	Chlorophyll a	OH-Chlorophyll a	Pheophytin a	OH-Pheophytin a
2A-1,36, 0-2	1.92	0.17	0.09	0.01	0.05	0.00	-	0.21	0.06	0.00	0.01	0.00	0.02	0.01	0.02	0.01	-	0.00	-	0.01	0.00	0.00	0.00
2A-1,36, 2-4	0.54	0.12	0.04	0.01	0.18	0.02	0.00	0.17	0.03	0.00	0.00	0.00	0.02	0.02	0.01	0.01	-	0.00	-	0.01	0.00	0.01	-
2A-1,36, 4-6	2.39	0.27	0.19	0.03	0.31	0.03	-	0.38	0.11	0.01	0.02	0.01	0.02	0.04	0.01	-	-	-	-	0.00	-	-	-
2A-1,36, 6-8	0.09	0.02	0.01	0.00	0.02	0.01	-	0.07	0.01	0.00	0.00	-	0.00	0.00	0.00	-	-	0.00	-	0.00	-	0.00	-
2A-1,36, 8-10	0.07	0.02	0.00	0.00	0.06	0.01	-	0.05	0.01	0.00	0.00	0.00	0.01	0.01	0.01	-	0.00	0.00	-	-	-	-	-
2A-1,36, 10-12	1.92	0.21	0.13	0.02	0.16	0.01	-	0.35	0.09	0.01	0.01	0.00	0.02	0.02	0.01	-	-	0.00	-	0.01	-	-	-
2A-1,36, 12-14	0.54	0.14	0.03	0.01	0.15	0.00	0.00	0.21	0.04	0.00	0.01	0.00	0.01	0.03	0.01	-	-	0.00	-	0.00	0.00	0.00	0.00
2A-1,36, 14-16	0.15	0.02	0.01	0.00	0.06	0.01	0.00	0.05	0.01	0.00	0.00	0.00	0.01	0.00	0.00	-	-	0.00	-	0.00	-	-	-
2A-1,36, 16-18	0.24	0.04	0.02	0.01	0.07	0.00	0.00	0.09	0.01	0.00	0.00	0.00	0.01	0.01	0.01	-	-	0.00	-	0.00	-	-	-
2A-1,36, 18-20	0.88	0.18	0.09	0.02	0.16	0.01	0.00	0.28	0.06	0.01	0.01	0.01	0.01	0.02	0.02	-	-	0.00	-	0.00	-	0.00	-
2A-1,36, 20-24	0.93	0.09	0.08	0.01	0.08	0.00	0.00	0.17	0.04	0.00	0.01	0.00	0.01	0.01	0.00	-	-	0.00	-	0.01	-	-	-
2A-1,36, 24-28	0.07	0.01	0.00	0.00	0.04	0.00	0.00	0.02	0.00	0.00	0.00	0.00	0.01	0.02	0.00	-	-	0.00	-	-	-	-	-

Table B3.2: The Hole (core 2) downcore lipid concentrations (μg·g^{-1} sed).

Sample Name	GDGT	OH-GDGT	GDD	OH-GDD	AR	OH-AR	Bpdiol	br-GDGT	1G-GDGT	1G-OH-GDGT	2G-GDGT	2G-OH-GDGT	1G-AR	2G-AR	PA-AR	PA-OH-AR	PG-AR	PS-AR	PG-GDGT	Chlorophyll a	OH-Chlorophyll a	Pheophytin a	OH-Pheophytin a
2A-1,78,0-2	3.04	0.48	0.14	0.01	0.04	-	-	0.41	0.37	0.02	0.00	0.00	0.07	0.01	-	-	-	-	-	0.00	0.00	-	0.00
2A-1,78,2-4	2.33	0.38	0.12	0.04	0.21	-	0.00	0.35	0.27	0.02	0.12	0.01	0.06	0.03	-	-	-	-	0.02	0.00	-	-	-
2A-1,78,4-6	2.50	0.42	0.10	0.03	0.40	0.01	0.00	0.31	0.17	0.01	0.07	0.01	0.05	0.03	-	-	-	-	0.04	0.00	-	-	-
2A-1,78,6-8	1.93	0.37	0.10	0.04	0.51	0.01	0.00	0.34	0.10	0.01	0.11	0.01	0.05	0.03	-	-	-	-	0.10	0.00	-	-	0.00
2A-1,78,8-10	2.53	0.52	0.17	0.04	0.43	0.01	0.00	0.53	0.10	0.01	0.08	0.01	0.03	0.01	-	-	-	-	0.11	0.00	-	-	-
2A-1,78,10-12	0.43	0.05	0.02	0.01	0.38	0.03	0.00	0.10	0.02	0.00	0.01	0.00	0.07	0.03	-	-	-	-	0.01	-	-	-	-
2A-1,78,12-14	0.82	0.20	0.09	0.02	0.37	0.02	0.00	0.29	0.06	0.01	0.01	0.00	0.05	0.02	-	-	-	-	0.01	-	-	-	-
2A-1,78,14-16	0.90	0.17	0.12	0.02	0.12	0.01	0.01	0.30	0.07	0.00	0.00	0.00	0.02	0.01	-	-	-	-	0.00	-	-	-	-
2A-1,78,16-18	1.29	0.24	0.17	0.03	0.17	0.01	0.01	0.65	0.09	0.01	0.00	0.00	0.04	0.01	-	-	-	-	0.00	0.00	-	-	-
2A-1,78,18-20	1.10	0.19	0.13	0.02	0.07	0.00	0.01	0.32	0.07	0.01	0.00	0.00	0.01	0.00	-	-	-	-	0.00	0.00	-	-	0.00

Table B3.3: Holey Ground (core 3) downcore lipid concentrations (μg·g^{-1} sed).

Sample Name	GDGT	OH-GDGT	GDD	OH-GDD	AR	OH-AR	Bpdiol	br-GDGT	1G-GDGT	1G-OH-GDGT	2G-GDGT	2G-OH-GDGT	1G-AR	2G-AR	PA-AR	PA-OH-AR	PG-AR	PS-AR	PG-GDGT	Chlorophyll a	OH-Chlorophyll A	Pheophytin a	OH-Pheophytin a
2A-1,18, 0-2	0.16	0.03	0.01	0.00	0.01	0.00	0.00	0.04	0.03	0.00	0.00	0.00	0.01	0.01	0.01	-	0.00	0.00	-	0.01	0.01	0.00	0.00
2A-1,18, 2-4	3.54	0.22	0.16	0.02	0.09	0.01	0.00	0.22	0.26	0.01	0.07	0.00	0.05	0.03	0.00	0.01	0.01	0.00	0.10	-	-	-	-
2A-1,18, 4-6	0.71	0.09	0.02	0.01	0.26	0.02	0.00	0.08	0.03	0.00	0.12	0.00	0.05	0.04	0.01	0.01	0.01	-	-	0.00	0.00	-	0.00
2A-1,18, 6-8	0.18	0.02	0.00	0.00	0.11	0.01	0.00	0.03	0.02	0.00	0.03	0.00	0.04	0.04	0.01	-	0.00	0.00	-	0.01	0.00	0.00	0.00
2A-1,18, 8-10	0.25	0.04	0.01	0.00	0.05	0.02	-	0.05	0.02	0.00	0.02	0.00	0.02	0.02	0.00	-	0.00	0.00	-	0.00	0.00	-	0.00
2A-1,18, 10-12	1.07	0.14	0.07	0.02	0.24	0.02	0.00	0.14	0.13	0.00	0.14	0.01	0.06	0.04	0.01	-	0.00	0.00	0.04	0.01	0.00	0.00	0.00
2A-1,18, 12-14	0.40	0.08	0.02	0.01	0.15	0.01	0.00	0.07	0.02	0.00	0.03	0.00	0.04	0.02	0.01	-	0.00	0.00	0.00	0.01	-	0.00	0.00
2A-1,18, 14-16	0.81	0.15	0.05	0.02	0.23	0.02	0.00	0.14	0.05	0.00	0.08	0.00	0.05	0.04	0.01	0.01	0.00	0.00	0.03	0.01	0.00	0.00	0.00
2A-1,18, 16-18	0.22	0.05	0.02	0.00	0.04	0.01	-	0.07	0.01	0.00	0.01	0.00	0.01	0.01	0.01	-	0.00	0.00	-	0.01	0.00	-	0.00
2A-1,18, 18-20	0.13	0.02	0.01	0.00	0.10	0.02	0.00	0.04	0.01	0.00	0.01	0.00	0.03	0.02	0.01	-	0.01	0.00	-	0.00	0.00	0.00	0.00
2A-1,18, 20-24	0.38	0.04	0.02	0.01	0.09	0.01	0.00	0.06	0.02	0.00	0.01	0.00	0.02	0.01	0.01	-	0.00	0.00	-	0.00	0.00	0.00	0.00

Table B3.4: Crusty White Clams (core 4) downcore lipid concentration (μg·g^{-1} sed).

Sample Name	GDGT	OH-GDGT	GDD	OH-GDD	AR	OH-AR	Bpdiol	br-GDGT	1G-GDGT	1G-OH-GDGT	2G-GDGT	2G-OH-GDGT	1G-AR	2G-AR	PA-AR	PA-OH-AR	PG-AR	PS-AR	PG-GDGT	Chlorophyll a	OH-Chlorophyll A	Pheophytin a	OH-Pheophytin a
2A-1,29, 0-2	0.22	0.05	0.01	0.00	0.05	0.01	-	0.06	0.01	0.00	0.00	0.00	0.03	0.03	0.02	0.02	-	0.00	-	0.02	0.00	0.00	0.00
2A-1,29, 2-4	0.70	0.13	0.04	0.00	0.11	0.01	-	0.13	0.07	0.00	0.00	0.00	0.04	0.03	0.02	0.01	-	0.00	-	-	-	-	-
2A-1,29, 4-6	3.16	0.35	0.15	0.01	0.09	0.01	0.00	0.38	0.11	0.00	0.00	0.00	0.04	0.05	0.03	0.02	-	0.01	-	-	-	-	-
2A-1,29, 6-8	2.36	0.30	0.10	0.01	0.16	0.03	-	0.33	0.08	0.00	0.01	0.00	0.07	0.09	0.02	-	-	0.01	-	-	-	-	-
2A-1,29, 8-10	3.12	0.35	0.15	0.01	0.21	0.03	-	0.37	0.13	0.00	0.01	0.00	0.10	0.11	0.02	0.05	-	0.01	-	-	-	-	-
2A-1,29, 10-12	0.23	0.07	0.01	0.00	0.06	0.02	0.00	0.07	0.01	0.00	0.00	0.00	0.02	0.03	0.01	-	-	0.00	-	0.00	-	-	-
2A-1,29, 12-14	0.12	0.04	0.01	0.00	0.05	0.01	0.00	0.04	0.01	0.00	0.00	0.00	0.02	0.03	0.01	-	-	0.00	-	0.00	0.00	-	0.00
2A-1,29, 14-16	0.26	0.07	0.02	0.01	0.03	0.02	-	0.09	0.01	0.00	0.00	0.00	0.03	0.03	0.01	-	-	0.00	-	0.01	-	-	-
2A-1,29, 16-18	2.27	0.39	0.16	0.03	0.19	0.00	0.01	0.11	0.05	0.01	0.04	0.01	0.02	0.03	0.02	0.00	-	0.00	0.01	0.05	0.00	0.00	0.00
2A-1,29, 18-20	0.19	0.04	0.01	0.00	0.03	0.00	0.00	0.05	0.01	0.00	0.00	0.00	0.00	0.01	0.01	-	-	0.00	-	0.00	0.00	-	-
2A-1,29, 20-24	1.17	0.27	0.08	0.02	0.18	0.01	0.00	0.12	0.05	0.01	0.04	0.01	0.02	0.02	0.01	0.00	-	0.00	-	0.02	0.00	0.00	0.00
2A-1,29, 24-28	3.07	0.44	0.24	0.04	0.14	-	0.01	0.18	0.09	0.01	0.07	0.01	0.02	0.02	0.01	-	-	0.00	0.02	0.05	-	-	-
2A-1,29, 28-32	0.32	0.03	0.01	0.00	0.02	0.00	0.00	0.02	0.00	0.00	0.00	0.00	0.00	0.00	0.00	-	-	0.00	-	0.00	0.00	0.00	0.00
2A-1,29, 32-38	1.27	0.20	0.05	0.01	0.10	0.00	0.00	0.10	0.02	0.00	0.04	0.00	0.01	0.00	0.01	-	-	0.00	-	0.01	0.00	-	0.00

Table B3.5: NW 875m Transect (core 5) downcore lipid concentration ($\mu g \cdot g^{-1}$ sed).

Sample Name	GDGT	OH-GDGT	GDD	OH-GDD	AR	OH-AR	Bpdiol	br-GDGT	1G-GDGT	1G-OH-GDGT	2G-GDGT	2G-OH-GDGT	1G-AR	2G-AR	PA-AR	PA-OH-AR	PG-AR	PS-AR	PG-GDGT	Chlorophyll a	OH-Chlorophyll A	Pheophytin a	OH-Pheophytin a
2A,66, 0-2	0.89	0.07	0.06	0.00	0.00	-	0.00	0.05	0.04	0.00	0.00	0.00	0.00	-	0.01	-	-	0.00	-	0.00	0.00	-	-
2A,66, 2-4	0.05	0.01	0.00	0.00	0.00	-	0.00	0.01	0.00	0.00	0.00	0.00	0.00	-	0.00	-	-	0.00	-	0.00	0.00	0.00	0.00
2A,66, 4-6	0.02	0.01	0.00	0.00	0.00	-	0.00	0.01	0.00	0.00	0.00	0.00	0.00	-	0.00	-	-	0.00	-	-	0.00	-	0.00
2A,66, 6-8	0.71	0.06	0.05	0.00	0.01	-	0.00	0.06	0.04	0.00	0.00	0.00	0.00	-	0.00	-	-	0.00	-	0.04	0.00	0.00	0.00
2A,66, 8-10	0.43	0.04	0.02	0.00	0.00	-	0.00	0.04	0.02	0.00	0.00	0.00	0.00	-	0.00	-	-	0.00	-	0.04	0.00	0.00	0.00
2A,66, 10-12	0.84	0.09	0.05	0.01	0.01	-	0.00	0.08	0.07	0.00	0.00	0.00	0.00	0.00	0.01	-	-	0.00	-	0.08	0.00	0.00	0.00
2A,66, 12-14	0.37	0.03	0.01	0.00	0.00	-	0.00	0.03	0.02	0.00	0.00	0.00	0.00	0.00	0.00	-	-	0.00	-	0.02	0.00	0.00	0.00
2A,66, 14-16	2.18	0.23	0.12	0.01	0.01	-	0.00	0.14	0.13	0.01	0.01	0.01	0.00	0.00	0.01	-	-	0.00	-	0.00	0.00	0.00	0.00
2A,66, 16-18	0.36	0.07	0.02	0.01	0.01	-	0.00	0.04	0.02	0.00	0.00	0.00	0.00	0.00	0.01	-	-	0.00	-	0.02	0.00	0.00	0.00
2A,66, 18-20	0.22	0.07	0.01	0.01	0.01	-	0.00	0.03	0.01	0.00	0.00	0.00	0.00	0.00	0.01	-	-	0.00	-	0.01	0.00	0.00	0.00
2A,66, 20-24	0.73	0.19	0.06	0.02	0.02	-	0.00	0.09	0.04	0.00	0.00	0.01	0.00	0.01	0.02	-	-	0.00	-	0.01	0.01	0.00	0.01
2A,66, 24-28	2.40	0.38	0.12	0.02	0.01	-	0.01	0.14	0.13	0.01	0.01	0.01	0.00	0.00	0.02	-	-	0.00	-	0.01	0.00	0.00	0.00
2A,66, 28-32	0.38	0.07	0.02	0.00	0.01	-	0.00	0.04	0.01	0.00	0.00	0.00	0.00	-	0.01	-	-	0.00	-	0.02	0.00	0.00	0.00
2A,66, 32-36	4.07	0.67	0.34	0.06	0.02	-	0.01	0.25	0.18	0.02	0.02	0.03	0.00	0.00	0.03	-	-	0.00	-	0.11	0.01	0.00	0.02
2A,66, 36-40	0.52	0.09	0.02	0.00	0.01	-	0.00	0.05	0.01	0.00	0.00	0.00	0.00	-	0.01	-	-	0.00	-	0.01	0.00	0.00	0.00

Table B3.6: Midpoint Transect (core 6) downcore lipid concentrations (μg·g^{-1} sed).

Sample Name	GDGT	OH-GDGT	GDD	OH-GDD	AR	OH-AR	Bpdiol	br-GDGT	1G-GDGT	1G-OH-GDGT	2G-GDGT	2G-OH-GDGT	1G-AR	2G-AR	PA-AR	PA-OH-AR	PG-AR	PS-AR	PG-GDGT	Chlorophyll a	OH-Chlorophyll A	Pheophytin a	OH-Pheophytin a
2A,41, 0-2	0.55	0.05	0.04	0.00	0.00	-	0.01	0.03	0.03	0.00	0.00	0.00	0.00	-	0.01	-	-	0.00	-	0.03	0.00	0.00	0.00
2A,41, 2-4	0.46	0.03	0.04	0.00	0.00	-	0.00	0.04	0.03	0.00	0.00	0.00	0.00	-	0.00	-	-	0.00	-	0.01	0.00	0.00	0.00
2A,41, 4-6	0.59	0.05	0.03	0.00	0.00	-	0.00	0.04	0.04	0.00	0.00	0.00	0.00	-	0.00	-	-	0.00	-	0.01	0.00	0.00	0.00
2A,41, 6-8	0.52	0.04	0.04	0.00	0.00	-	0.00	0.04	0.03	0.00	0.00	0.00	0.00	-	0.00	-	-	0.00	-	0.00	0.00	0.00	0.00
2A,41, 8-10	0.04	0.01	0.00	0.00	0.00	-	0.00	0.00	0.00	0.00	-	0.00	0.00	-	0.00	-	-	0.00	-	-	0.00	-	0.00
2A,41, 10-12	0.40	0.04	0.03	0.00	0.00	-	0.00	0.04	0.03	0.00	0.00	0.00	0.00	-	0.00	-	-	0.00	-	-	0.00	-	0.00
2A,41, 12-14	1.00	0.08	0.06	0.01	0.00	-	0.00	0.07	0.07	0.00	0.00	0.00	0.00	-	0.00	-	-	0.00	-	0.03	0.00	0.00	0.00
2A,41, 14-16	1.00	0.09	0.06	0.01	0.01	-	0.01	0.08	0.09	0.00	0.00	0.00	0.00	-	0.00	-	-	0.00	-	-	0.00	-	0.00
2A,41, 16-18	1.15	0.10	0.11	0.01	0.01	-	0.00	0.12	0.06	0.00	0.00	0.00	0.00	-	0.01	-	-	0.00	-	0.04	0.00	0.00	0.00
2A,41, 18-20	0.64	0.05	0.03	0.00	0.00	-	0.00	0.04	0.02	0.00	0.00	0.00	0.00	-	0.00	-	-	0.00	-	-	0.00	-	0.00
2A,41, 20-24	0.47	0.07	0.02	0.01	0.00	-	0.00	0.05	0.03	0.00	0.00	0.00	0.00	-	0.01	-	-	0.00	-	-	0.00	-	0.00
2A,41, 24-28	2.04	0.27	0.13	0.02	0.01	-	0.00	0.16	0.10	0.01	0.01	0.01	0.00	-	0.00	-	-	0.00	-	0.00	0.01	-	0.01
2A,41, 28-32	0.15	0.04	0.01	0.00	0.00	-	-	0.03	0.01	0.00	0.00	0.00	0.00	-	0.00	-	-	0.00	-	0.01	0.00	0.00	0.00
2A,41, 32-36	2.83	0.46	0.23	0.04	0.01	-	0.00	0.22	0.13	0.01	0.01	0.01	0.00	-	0.01	-	-	0.00	-	0.05	0.01	0.00	0.00

Table B3.7: Average Simpson's Diversity Index for IPL and CL community in each core.

	IPL				**CL**			
Site	**D**	**1-D**	**Max**	**Min**	**D**	**1-D**	**Max**	**Min**
Deep Purple	0.25	0.75	0.83	0.66	0.38	0.62	0.75	0.37
The Hole	0.37	0.63	0.79	0.35	0.40	0.60	0.71	0.43
Holey Ground	0.23	0.77	0.82	0.71	0.41	0.59	0.72	0.30
Crusty White Clams	0.24	0.76	0.83	0.68	0.47	0.53	0.72	0.36
NW 875m Transect	0.41	0.59	0.74	0.40	0.57	0.44	0.64	0.32
Midpoint	0.50	0.50	0.74	0.35	0.62	0.38	0.56	0.28

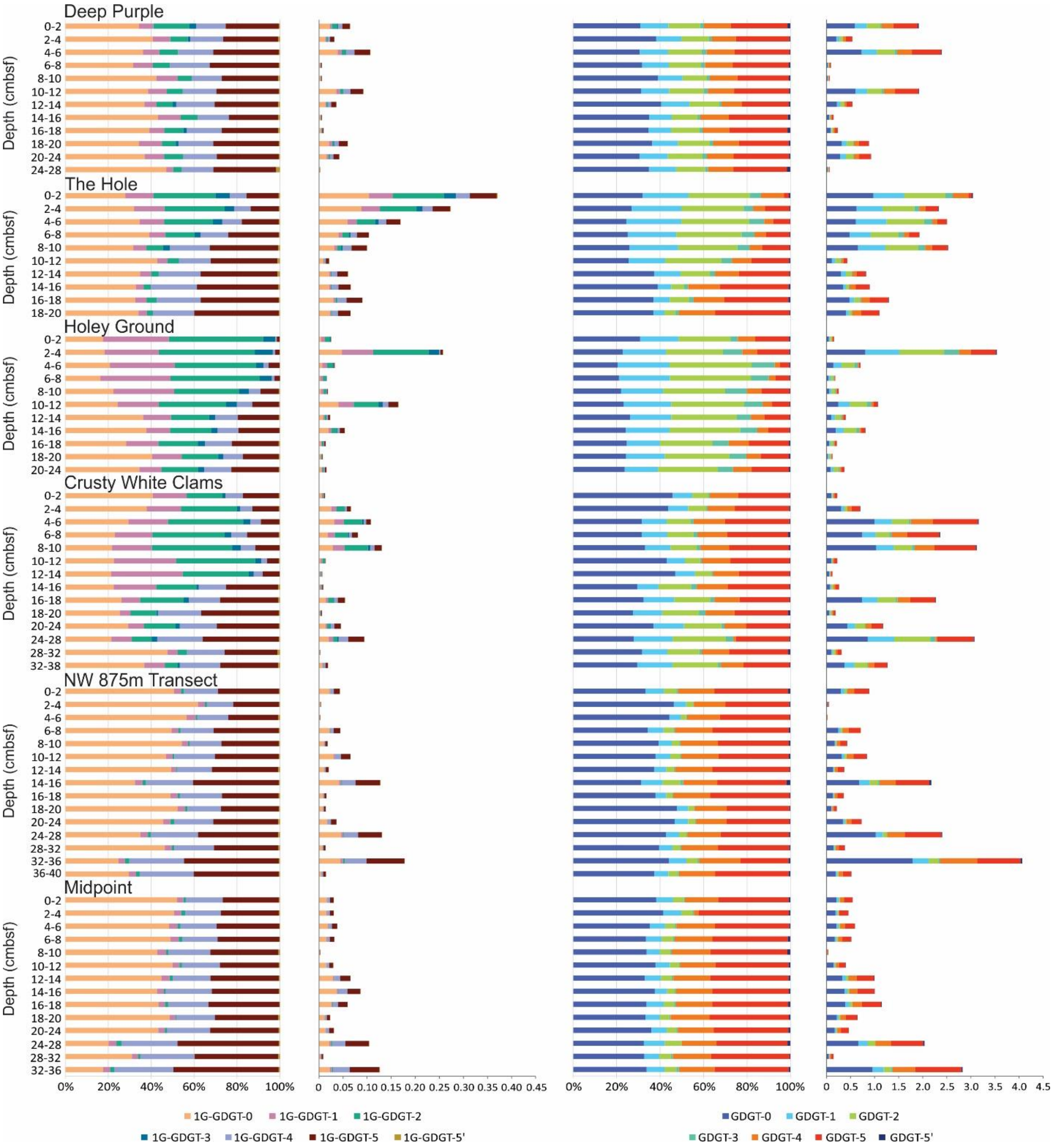

Figure B3.1: 1G-GDGT and GDGT relative abundance and concentrations across site 2A-1 transect.

4. The Redshaw Ratio

Table B4.1: Average abundance of crenarchaeaol in each core along the Site 2A-1 transect. The Redshaw ratio can be used to estimate the relative abundance of crenarchaeol at any depth at site 2A-1.

Site	1G-GDGT(5)	GDGT(5)	GDD(5)
Deep Purple	5.02	84.63	10.34
The Hole	10.63	74.54	14.84
Holey Ground	5.78	81.81	12.41
Crusty White Clams	2.50	88.62	8.87
NW 875m Transect	4.74	87.68	7.58
Midpoint Transect	4.93	88.14	6.93
Average	5.60	84.24	10.16
STDV	2.46	4.94	2.76

5. Principal Component Analysis

A scree plot of the eigenvectors was created using the “factoextra” package in Rstudio. The first four components are responsible for close to 75% of the variance.

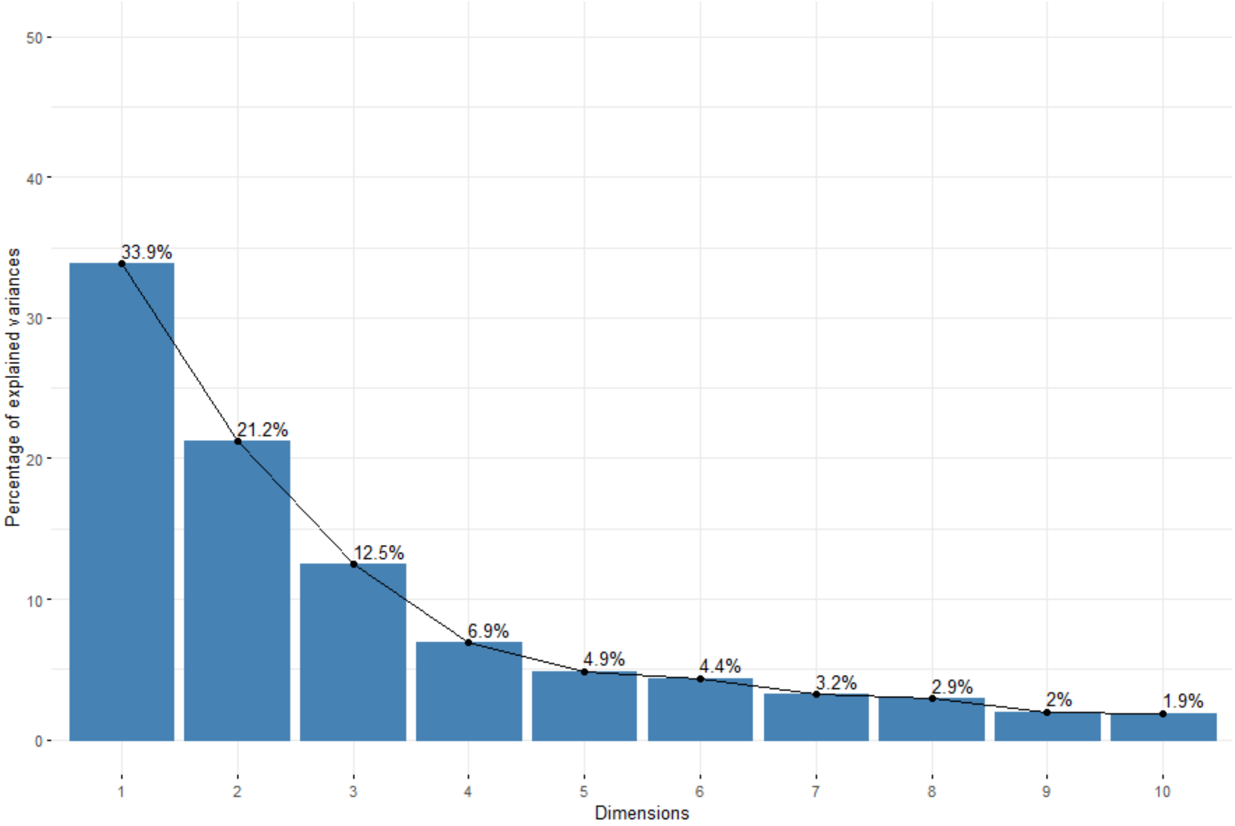

Figure B5.1: Scree plot of lipidomic PCA eigenvalues.

The third and forth principal components accounted for less than 20% of the data variance (Fig. 2C) but were included in the analysis as the first two components could only explain <55% of the variance. No interpretation of the data distribution along PC 3 and PC 4 has been attempted at this time.

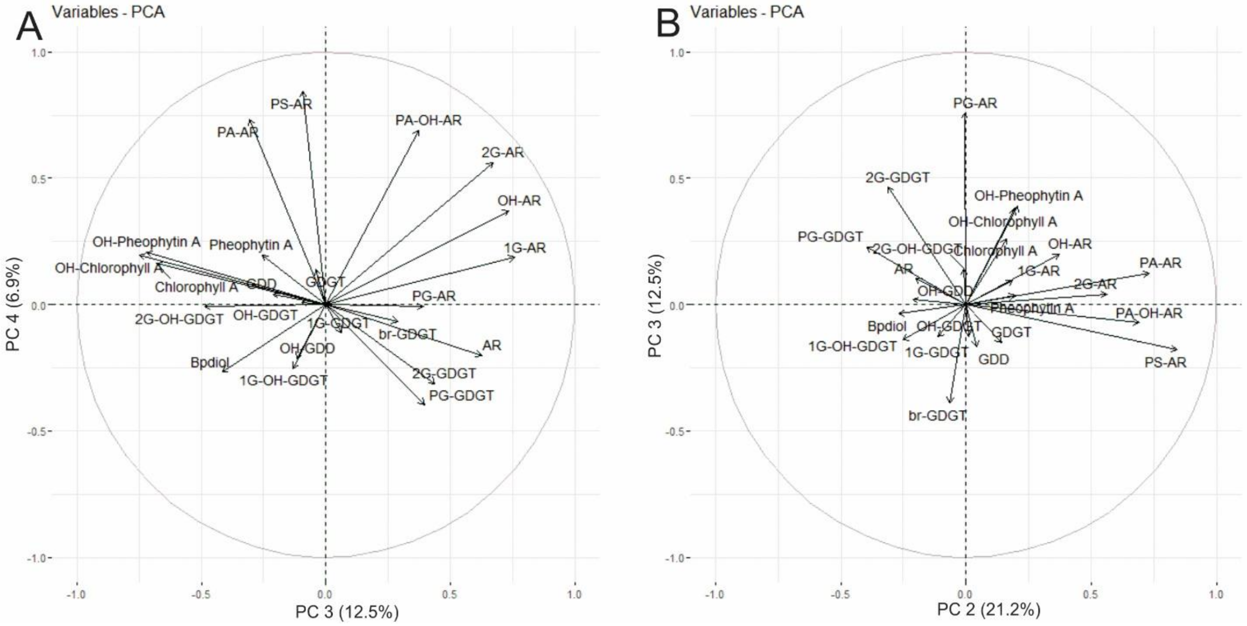

Figure B5.2: PCA imbedded factor loadings and scores plots for A) PC 2 and PC 3 and B) PC 3 and PC 4.

Where ring structure is influenced by temperature (Schouten et al., 2002), a PCA of the site 2A-1 lipidome, separated into individual classes was completed to create separation in the ubiquitous GDGT classes (Figure C3). This created separation along PC 2 specifically with 1, 2, and 3-ringed structures exhibiting positive loadings into what has been described into the seepage related zone. Crenarchaeol dropped to a negative loading, into the more oxic zone with the water column sourced pigments. GDGT-0 continued to experience no strong loadings, a further sign of the lipid's ubiquitous nature.

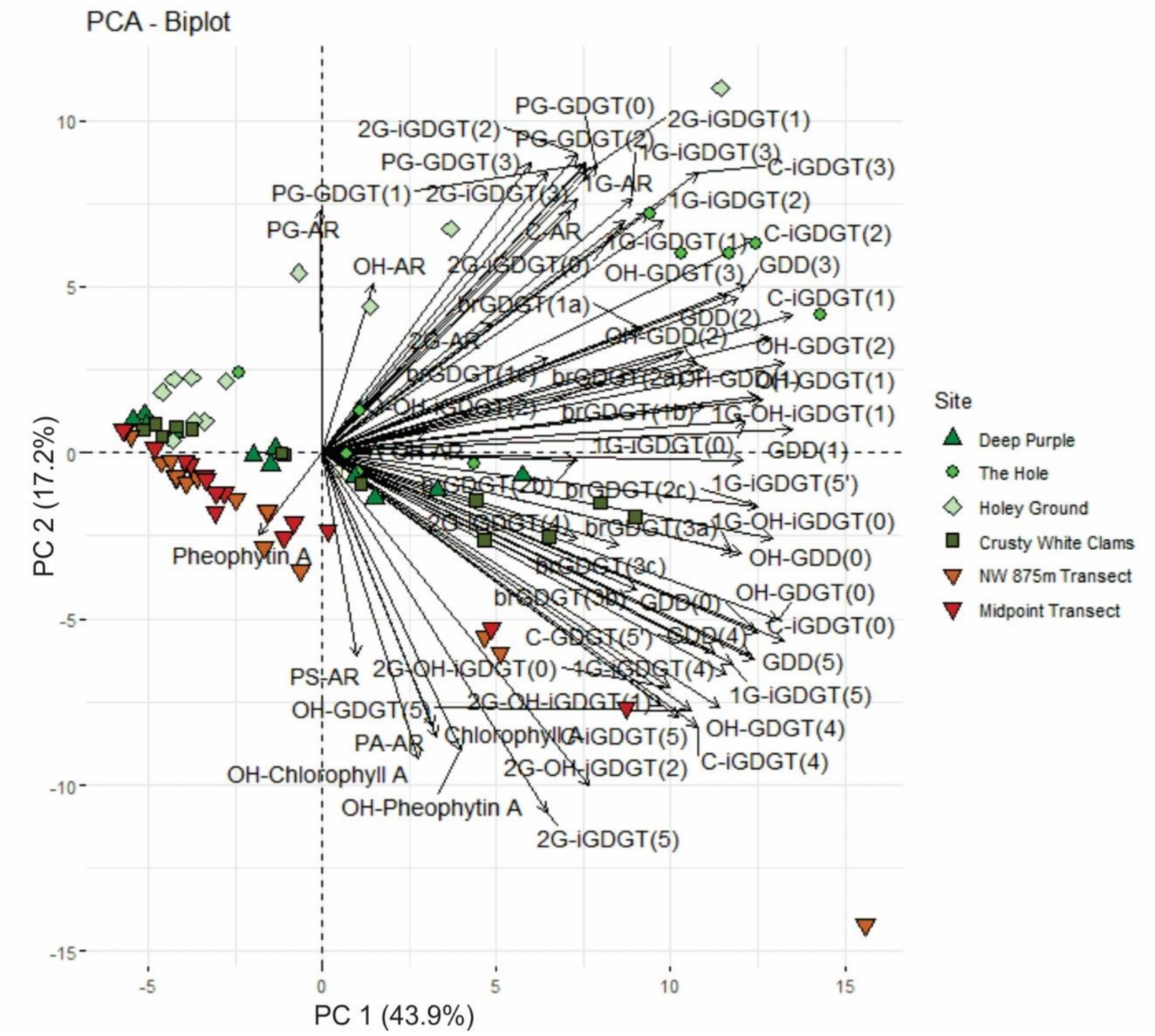

Figure B5.3: PCA biplot of lipid classes separated by ring structure.

6. Lipidomic Environmental Proxies

Table B5.1: Summary of lipid proxies calculated at Site 2A-1. Data is organized downcore by location across the transect.

Sample Name	MI$_{\text{CL}}$	MI$_{\text{IPL}}$	*br*SRI	AR:OH-AR
2A-1,36, 0-2	0.52	0.51	0.72	0.03
2A-1,36, 2-4	0.50	0.40	0.72	0.09
2A-1,36, 4-6	0.54	0.34	0.73	0.09
2A-1,36, 6-8	0.52	0.34	0.73	0.54
2A-1,36, 8-10	0.49	0.38	0.69	0.14
2A-1,36, 10-12	0.54	0.35	0.71	0.04
2A-1,36, 12-14	0.55	0.33	0.73	0.03
2A-1,36, 14-16	0.45	0.44	0.72	0.12
2A-1,36, 16-18	0.47	0.39	0.76	0.07
2A-1,36, 18-20	0.54	0.37	0.74	0.03
2A-1,36, 20-24	0.54	0.38	0.74	0.02
2A-1,36, 24-28	0.51	0.19	0.64	0.08
2A-1,78,0-2	0.95	0.76	0.54	0.00
2A-1,78,2-4	0.83	0.77	0.71	0.00
2A-1,78,4-6	0.89	0.68	0.72	0.01
2A-1,78,6-8	0.84	0.50	0.78	0.03
2A-1,78,8-10	0.81	0.34	0.76	0.01
2A-1,78,10-12	0.73	0.24	0.77	0.07
2A-1,78,12-14	0.54	0.19	0.77	0.05
2A-1,78,14-16	0.30	0.15	0.76	0.06
2A-1,78,16-18	0.38	0.21	0.83	0.06
2A-1,78,18-20	0.25	0.14	0.69	0.04
2A-1,18, 0-2	0.74	0.98	0.61	0.16
2A-1,18, 2-4	0.78	0.97	0.63	0.13
2A-1,18, 4-6	0.94	0.93	0.64	0.09
2A-1,18, 6-8	0.91	0.97	0.64	0.10
2A-1,18, 8-10	0.81	0.87	0.60	0.39
2A-1,18, 10-12	0.88	0.81	0.69	0.07
2A-1,18, 12-14	0.82	0.63	0.60	0.09
2A-1,18, 14-16	0.85	0.63	0.70	0.07
2A-1,18, 16-18	0.71	0.62	0.64	0.19
2A-1,18, 18-20	0.80	0.66	0.72	0.19
2A-1,18, 20-24	0.74	0.57	0.72	0.17
2A-1,29, 0-2	0.42	0.66	0.56	0.22
2A-1,29, 2-4	0.42	0.77	0.57	0.12
2A-1,29, 4-6	0.44	0.86	0.53	0.14
2A-1,29, 6-8	0.47	0.78	0.57	0.18
2A-1,29, 8-10	0.47	0.84	0.43	0.15
2A-1,29, 10-12	0.37	0.92	0.59	0.28

2A-1,29, 12-14	0.42	0.89	0.57	0.16
2A-1,29, 14-16	0.49	0.61	0.55	0.47
2A-1,29, 16-18	0.58	0.53	0.54	0.03
2A-1,29, 18-20	0.56	0.33	0.60	0.16
2A-1,29, 20-24	0.61	0.45	0.66	0.03
2A-1,29, 24-28	0.65	0.37	0.59	0.00
2A-1,29, 28-32	0.49	0.26	0.65	0.14
2A-1,29, 32-38	0.64	0.37	0.65	0.01
2A,66, 0-2	0.30	0.14	0.46	0.00
2A,66, 2-4	0.24	0.16	0.48	0.00
2A,66, 4-6	0.20	0.17	0.50	0.00
2A,66, 6-8	0.26	0.12	0.50	0.00
2A,66, 8-10	0.23	0.12	0.45	0.00
2A,66, 10-12	0.26	0.11	0.47	0.00
2A,66, 12-14	0.21	0.08	0.45	0.00
2A,66, 14-16	0.36	0.11	0.51	0.00
2A,66, 16-18	0.18	0.14	0.59	0.00
2A,66, 18-20	0.22	0.15	0.55	0.00
2A,66, 20-24	0.25	0.14	0.55	0.00
2A,66, 24-28	0.23	0.11	0.57	0.00
2A,66, 28-32	0.23	0.13	0.54	0.00
2A,66, 32-36	0.38	0.10	0.56	0.00
2A,66, 36-40	0.25	0.11	0.56	0.00
2A,41, 0-2	0.29	0.13	0.45	0.00
2A,41, 2-4	0.25	0.16	0.46	0.00
2A,41, 4-6	0.26	0.15	0.47	0.00
2A,41, 6-8	0.27	0.16	0.45	0.00
2A,41, 8-10	0.24	0.13	0.42	0.00
2A,41, 10-12	0.25	0.14	0.44	0.00
2A,41, 12-14	0.26	0.14	0.47	0.00
2A,41, 14-16	0.21	0.11	0.43	0.00
2A,41, 16-18	0.27	0.12	0.41	0.00
2A,41, 18-20	0.24	0.09	0.39	0.00
2A,41, 20-24	0.25	0.11	0.52	0.00
2A,41, 24-28	0.34	0.11	0.53	0.00
2A,41, 28-32	0.26	0.09	0.52	0.00
2A,41, 32-36	0.30	0.09	0.50	0.00